Institute of Modern Physics

Chinese Academy of Sciences

Initial Investigations of (np)–Scattering with a Polarized Deuterium Target at ANKE–COSY

Ph.D. Thesis of

Boxing Gou

Supervisors from China   Prof. Z. Li (IMP)

       Prof. T. Wang (LZU)

Supervisors from Germany   Prof. H. Ströher (FZJ)

       Dr. A. Kacharava (FZJ)

至小无内，谓之小一。

<div align="right">—惠施</div>

一尺之棰，日取其半，万世不竭。

<div align="right">—公孙龙</div>

<div align="right">《庄子·天下篇》</div>

Declaration of Authorship

I, Boxing GOU, declare that this thesis titled, 'Initial Investigations of (n-p)–Scattering with a Polarized Deuterium Target at ANKE-COSY' and the work presented in it are my own. I confirm that:

- This work was done wholly or mainly while in candidature for a research degree.

- Where any part of this thesis has previously been submitted for a degree or any other qualification at this University or any other institution, this has been clearly stated.

- Where I have consulted the published work of others, this is always clearly attributed.

- Where I have quoted from the work of others, the source is always given. With the exception of such quotations, this thesis is entirely my own work.

- I have acknowledged all main sources of help.

- Where the thesis is based on work done by myself jointly with others, I have made clear exactly what was done by others and what I have contributed myself.

Signed:
_____

Date:
_____

Abstract

The understanding of the forces among nucleons is fundamental to the whole of nuclear and hadronic physics. The nucleon-nucleon (NN) scattering is the ideal probe to study the nuclear forces. The scattering amplitudes for the complete description of the NN interactions can be reconstructed from phase-shift analyses (PSA), which requires measurements with polarized experiments. The existing data allow to extract unambiguous proton-proton (pp) amplitudes below 2 GeV. However, there is very little known about the neutron-proton (np) system above 800 MeV nucleon energy. THE ANKE-COSY collaboration has embarked on a systematic program which aims to extract the np scattering amplitudes through the deuteron-proton charge-exchange process $dp \rightarrow \{pp\}_s n$. First part of the program via polarized deuteron beam and hydrogen target allowed successful measurement of np amplitudes up to 1.135 GeV nucleon energy, which is the maximum nucleon energy that can be accessed with deuteron beam at COSY. Via inverse kinematics, i.e. using a proton beam incident on a polarized deuterium target will allow to enhance the np study up to 2.8 GeV, the highest energy available at COSY. The method of inverse kinematics has to be validated prior to the production experiment. As the proof-of-principle (POP) experiment, the initial research has been conducted at proton energy $T_p = 600$ MeV using a polarized deuterium target. The projectiles were measured by two silicon tracking telescopes (STT) placed closed to the target and by the ANKE sub-detection systems. Four polarization modes of the deuterium target were employed. In order to increase the effective target thickness, polarized deuterium atoms produced by the atomic beam source (ABS) was filled into a storage cell, where the circulating COSY beam collides with the target. The target polarizations were measured using the proton-deuteron elastic reaction. The vector and tensor analyzing powers A_y and A_{yy} of $p\vec{d} \rightarrow n\{pp\}_s$ were measured for momentum transfers $q \geqslant 160$ MeV/c. These data connect smoothly with the previous measurements at $q \leqslant 140$ MeV/c performed using a polarized deuteron beam. The data presented in present thesis are well reproduced by the impulse approximation using the SAID np amplitudes. The results therefore proves that it is possible to continue the np programme at higher energies at ANKE.

Contents

To my parents

Chapter 1

Introduction

1.1 Physics Motivation

Human's inherent curiosity is the driving force which pushes physics developing forward. What on earth is the world we live in? How does it operate? What is it made of? What holds it together? Every human being asks these questions in the childhood. For thousands of years, people tried to find the answers to those questions by investigating different aspects of the world, and several branches of physics haven been developed. On this exciting journey, many physicists devoted enormous wisdom and efforts, which have crystallized into the precious knowledge. By studying the motions of the planets, the classical mechanics was established, it describes how an object moves, provided that this object is neither too small nor too fast. The classical mechanics is the foundation upon which the other branches of the physics were built. Thermodynamics deals with the phenomena such as heat, temperature, energy and work, its applications directly resulted the first industrial revolution. Another branch of physics, the electrodynamics, generalizes the laws of the electric and magnetic phenomena by the brief and nice Maxwell equations, which is usually regarded as the most beautiful theory in physics.

The above branches all belong to the classical physics, they were so successful that physicists once thought the whole physics had been established perfectly. In the late nineteenth century, two untackled problems, i.e. the black-body radiation problem and the surprising result of the Michelson-Morley experiment [1], triggered the discovery of the modern physics: the quantum physics and the relativity theory, which have developed rapidly in both depth and width in the twentieth century. As results, many new subjects were established. Among these new subjects, the subatomic physics has always been at the frontier of modern physics, it

studies the elementary building blocks of the world and the interactions between them. In 1897, via studying the cathode rays J. J. Thomson discovered the electron [2], which is the first subatomic particle ever been found. J. J. Thomson measured the velocity and the specific charge of electron using (crossed) electric and magnetic fields. The experiment results showed that the specific charge of electron is nearly two thousands larger than that of hydrogen ion, which was regarded as the lightest particle before 1897. Moreover, J. J. Thomson found this new particle could be produced from various materials, thus he postulated that electron was a common constituent of all atoms, spreading uniformly in a homogeneous bulk of positively charged material, like the plums in a pudding. Starting from 1909, Ernest Rutherford, together with his assistants Geiger and Marsden, began to perform an experiment to test Thomson's plum pudding model. They fired α particles at a thin gold foil, and observed the deflection of the outgoing α particles. According to the plum pudding model the α particles should go straight through the gold foil, at most be deflected just a little bit. Astonishingly, they found although most of the α particles passed through the gold foil almost undisturbed, a little fraction of them (about one in ten thousand) were deflected at very large angles. In 1911 Ernest Rutherford published the results and proposed his new model of the atom [3]. According to Rutherford's model, the positive charge and the most mass of atom are concentrated in the center, occupying only a tiny fraction of the space, while the electrons are spread around. In this famous experiment Rutherford and his cooperators discovered the nucleus, which started the era of nuclear physics. Based on Rutherford's model, Niels Bohr proposed the Bohr model for atoms and the primitive quantum theory in 1913 [4], which successfully explained the spectrum of the hydrogen atom. Rutherford named the core of the hydrogen atom as proton. At first physicists naturally thought that the heavier nuclei should be composed of more protons bound together, hence the atomic mass was supposed to be proportional to the atomic number. However, experiments showed that the atomic masses of the heavier atoms are evidently larger than expected. in 192, in order to account for this fact, Rutherford postulated that, besides the protons there ought to be neutral and massive particles inside the atomic nucleus yet to be discovered. In 1930 James Chadwick, Rutherford's student, discovered a nuetral and radioactive stream when he bombed Beryllium target with an α beam. Unlike gamma rays, this stream didn't induce the photo-electric effect. In 1932 Chadwick declared that the neutral stream was the particle which Rutherford had postulated, i.e. the neutron [5, 6]. Not only did Chadwick

discover the neutron, but also he determined the mass of neutron by applying momentum conservation technique to the following reaction.

$$\begin{array}{c}^4_2\alpha\end{array} + \begin{array}{c}^9_4Be\end{array} \rightarrow \begin{array}{c}^{12}_6C\end{array} + \begin{array}{c}^1_0n\end{array}$$
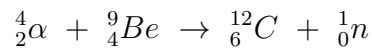
Remarkably, the neutron mass was measured to be almost the same as the proton mass. It seems that Chadwick's discovery completed the scenario of the nucleus, however, since there only positive and neutral constituents, the nucleus could not exist due to the repulsive electric force. Eugene Wigner asserted there must be an attractive force which hold the nucleus together. This attractive force is the nuclear strong force. In view of that proton and neutron have almost identical masses, Heisenberg came up with the concept of isospin soon after the discovery of the neutron, he proposed to regard the proton and neutron as two states of a single particle, i.e. the nucleon. According to Heisenberg's hypothesis, the strong force, unlike the electromagnetic force, is irrelevant to the electric charge. Furthermore, the nuclear strong force must act over a very short range, otherwise it would manifest itself earlier. These distinct features suggested that the nuclear strong interaction was completely different from the other interactions which physicists were familiar with, indeed its properties were barely unknown at that time. Since then, many physicists have pursued to uncover the nature of the nuclear force.

The first scientist who attempted to theoretically describe the nuclear strong interaction was Hideki Yukawa, he assumed in 1935 that there ought to be some particle mediating the nuclear force [7], just like the photon mediates the electromagnetic interaction. Given the short range of the nuclear strong force, Yukawa postulated that the mediator must be quit heavy, his calculation indicated that the mass of the mediator should be about one sixth of the proton mass. Since its mass is between those of electron and proton, this mediator was named as meson. Later in 1947, π meson was discovered in the cosmic rays, which coincided with Yukawa's particle. Yukawa was awarded the Nobel prize for physics in 1949 "for his prediction of the existence of mesons on the basis of theoretical work on nuclear force". However, Yukawa's one-pion theory of the nuclear force itself is not successful. Heavier force carriers were required to account for the nuclear force at shorter distances. Moreover, the dynamical behaviors of pion itself was not taken into account in Yukawa's theory. Later, more theories and modes for the nuclear interaction appeared. Some physicists introduced the multi-pion exchange model, where several pions can be treated as a single boson thanks to the strong correlation between them. With the discoveries of heavier mesons, heavy-meson

exchange theories were also developed. Except for the meson exchange theories, other theoretical attempts such as phenomenological potentials and quark models based on QCD theory were also proposed. Unfortunately, none of the present theories can satisfactorily explain all the experiments, and there are usually too many free parameters in those theories and models.

Through above discussion one can see that the nature of the nuclear strong interaction is so complicated that it is not possible to deduce it only from several experiments, as is possible in the cases of gravitational law and electromagnetic law. A lot of measurements are needed to acquire information on the nuclear strong interaction. Besides the bound systems of nucleons such as deuteron, the nucleon-nucleon (NN) scattering is the best probe to study the nuclear force. To perform the comparison between experiment and theory, it is convenient to define some quantities which can not only be derived directly from the theories but also summarize the experiment results. In fact the scattering amplitudes are very suitable to be such quantities, they could be deduced using the phase-shift analysis (PSA) from the experimental observables such as cross section, analyzing powers and spin correlation coefficients etc. Reversely, the experimental observables can be calculated from the amplitudes by the impulse approximations. On the other hand, the scattering amplitudes can be calculated from theory.

In the the following a short review of the NN scattering experiments in the intermediate and high energies is given in section 1.2. Since the polarized experiments involve many spin observables, it is necessary to introduce these quantities. In section 1.3 the complete description of reactions with spin is discussed in detail, through which the polarized observables are introduced.

1.2 Overview of the NN Scattering Investigation

The nucleon-nucleon (NN) system is an object with spin degree of freedom, therefore a thorough NN investigation is not possible without the polarized experiments. In the following, a brief introduction to the types and basic principles of the polarized beams and polarized targets which are most often utilized in the NN investigations is given first, then the measurements of the NN scattering at intermediate and high energies are summarized.

Polarized Beams

Generally speaking, the polarized beams can be classified into two categories according to their production approaches. The first type of the polarized beams are realized by collecting the products of certain nuclear reactions, whose final particles are usually polarized due to their spin-dependent dynamics. On the other hand, the second approach is based on the properties of spin itself, in this approach the particles are first polarized in the ion sources by the static magnetic fields and the radio-frequency electromagnetic fields, and then accelerated to the required energies by accelerators. In the early investigations in 1950s and 1960s the polarized beams were largely prepared through the nuclear reactions, where the unpolarized targets were bombarded by the unpolarized beams, the products were usually polarized thanks to the spin-dependence of the nuclear reactions. If a secondary beam of certain final particle was produced with small energy spread, low emittance and high polarization, it can be used as polarized beam to perform polarized measurements by bombarding other targets. These experiments are often referred as double-scattering experiment as they involve two scatterings. It is obvious that in the double-scattering experiments it is hard to adjust the energy , and the qualities[1] of the secondary beams are not good. Later, with the advance of the polarized ion sources [8] and the development of the polarized-beam acceleration, most laboratories started to perform experiments with the polarized beams provided directly by the accelerators. For instance, the IUCF at Indiana University, the TRIUMF at Canada's national laboratory for particle and nuclear physics, the LAMPF at the Los Alamos Laboratory, the SATURNE at the Saclay research center, the COSY at the Jülich research center, the RHIC at the Brookhaven laboratory etc., have hosted many polarized experiments. Since neutron can not be accelerated, the method of nuclear reaction is used for producing the polarized neutron beams. Unlike the double-scattering experiment mentioned previously, polarized proton/deuteron beams are impinged on certain targets, and the polarization are transferred form the primary beams to the secondary neutron beams by the deuteron breakup or by the collisions between the free proton and the bounded neutron. In such processes the energy of the neutron beam can be controlled. The SATURNE II–IKAR collaboration first obtained the free neutron beam with polarization of 0.59 ± 0.02 via the dueteron breakup on the Be target [10, 11]. Later the SATURNE II–NN collaboration also did experiments with polarized neutron beam. TRIUMF laboratory produced the polarized neutron beams through the

---

[1]i.e. the beam intensity and the phase space density.

reaction between the polarized proton and unpolarized deutron target [13]. At Los Alamos laboratory, targets of D, Be, as well as ^6Li and ^7Li were employed to collide with the polarized proton for the polarized neutron beam production [14–16]. PSI obtained the polarized neutron beams via the proton-carbon scattering [17].

Polarized Targets

According to the production principle, the polarized targets used for the NN scattering investigations can be classified into two types, i.e. the polarized solid target [18] and the polarized gas target [19].

In the production of the polarized solid targets, the first step is to polarized the unpaired electrons in some specific sold material. The unpaired electrons have spin magnetic moments of $\vec{\mu}_e = g_e \frac{\mu_B}{\hbar} \vec{S}^2$, when subjected to external magnetic field $\vec{B}$ and temperature T the distribution of the unpaired electrons in equilibrium obey the Boltzmann statistics

$$n_{\uparrow\downarrow} = n_0 \cdot e^{\frac{\vec{\mu}_e \cdot \vec{B}}{kT}} = n_0 \cdot e^{\frac{\mp \mu_B B}{kT}}, \tag{1.1}$$

where $n_\uparrow$ and $n_\downarrow$ denote the number of the unpaired electrons with spin parallel and antiparallel to the external magnetic field $\vec{B}$, and $n_0 = \frac{n_\uparrow + n_\downarrow}{2}$ stands for the half of the unpaired electrons. It can be derived from Eq. 1.1 that the spin polarization of the unpaired electron is

$$P_e = \frac{n_\uparrow - n_\downarrow}{n_\uparrow + n_\downarrow} = \frac{e^{-\frac{\mu_B B}{kT}} - e^{\frac{\mu_B B}{kT}}}{e^{-\frac{\mu_B B}{kT}} + e^{\frac{\mu_B B}{kT}}} = \tanh\left(-\frac{\mu_B B}{kT}\right). \tag{1.2}$$

Assuming that $B = 2.5\,T$ and $T = 1\,K$, using the constants $\mu_B = 5.8 \times 10^{-15} eV/T$ and $k = 8.6 \times 10^{-5} eV/K$ one can get the electron polarization $P_e = -0.93$. It shows the polarization of the unpaired electrons in the solid material are very high under the circumstance of low temperature and high magnetic field. Customarily the mechanism for producing polarization descried above is called Brute-force polarization. On the contrast, due to the extremely small proton magneton ($\frac{\mu_p}{\mu_B} = 1.52 \times 10^{-3}$), the proton spin polarization are smaller than that of the unpaired electrons by 3 orders of magnitude for the same magnetic field and temperature. It is therefore obvious that the Brute-force polarization mechanism can not be used for polarizing the spin of proton or deuteron. To obtain the nuclear polarization

---

$^2 g_e \approx -2$ and $\mu_B = \frac{e\hbar}{2m_e}$ are the electron spin g factor and the Bohr magneton respectively.

one has to utilize the so called Dynamic Nuclear Polarization (DNP) [20] to transfer the polarization from electron to proton (or deuteron).
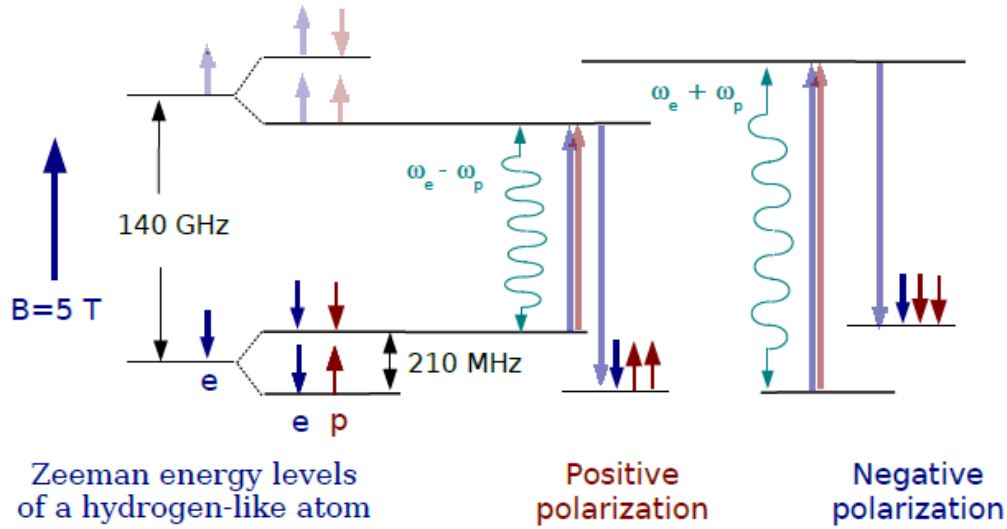
Figure 1.1: Principle of the dynamic nuclear polarization (DNP).

Fig. 1.1 illustrates the basic principle of the nuclear dynamic polarization. In a solid target, the unpaired electrons and the protons in the lattice form hydrogen-like systems, which split into four Zeemman states in a external magnetic field $\vec{B}$. If $B = 5\ T$, the split caused by the interaction between the external field and the electron is 140 GHz, and the split caused by the interaction between the electron and the proton is 210 MHz, corresponding to the Larmor precession frequencies of electron (ω_e) and proton (ω_p) respectively. As shown by the plot, the electron spin is polarized due to the Brute-force mechanism, i.e. more hydrogen-like systems populate in the states $|\downarrow\downarrow\rangle$ and $|\downarrow\uparrow\rangle$ than in the states $|\uparrow\downarrow\rangle$ and $|\uparrow\uparrow\rangle$. If a radio-frequency magnetic field B_{rf} with frequency $\omega_e - \omega_p$ is applied transversely with respect to the static magnetic field $\vec{B}$, the hydrogen-like systems at the state $|\downarrow\downarrow\rangle$ will absorb energy and transit to the state $|\uparrow\uparrow\rangle$. Then the electron spin flips and the hydrogen-like system transit to the low-energy state $|\downarrow\uparrow\rangle$. In this manner most of the proton spins will align parallel to the external magnetic field $\vec{B}$, thus positively polarized protons are prepared. Similarly, negative proton spin polarization will be achieved when a rf magnetic field with frequency $\omega_e + \omega_p$ is applied. Note the influence of the dipole coupling between the electron spins on the energy levels has to be taken into account when the concentration of the unpaired electron is high [18]. Actually, there should be enough unpaired electrons in the solid target in order to have high polarizing efficiency. Chemical doping and radioactive irradiation are used for producing unpaired electrons [18]. For

instance at Saclay and Gatchina, polarized targets were made of chemically doped butanol ($C4H9OH$) and propanediol ($C3H8O2$) [21], while ammonia targets such as NH_3 and ND_3 were irradiated with electron beams. After the polarizing process is completed, the target will be transferred to the target zone where a medium magnetic holding field (0.3-0.4 T) and extremely low temperature (50 mK) present for experiment. Such operation manner is customarily referred as frozen spin mode. In principle polarization in any direction can be realized by setting the direction of the holding field. Therefore, various observables can be accessed with solid polarized target in frozen spin mode.

Different from the polarized solid target, the polarized gas target [19] first makes use of inhomogeneous magnetic field at room temperature to polarize the electrons and then get the nuclear polarization by inducing certain Zeeman transitions using rf electromagnetic fields. The principle and the components of the polarized gas target are discussed in detail in section 3.3 of present thesis. Nucleon-nucleon scatting researches with polarized gas target mainly include the EDDA experiment [22] and ANKE experiment [23].

Summary of the NN Scattering Measurements at Intermediate and High Energies

With the advances of polarized beam and polarized target, many research institutions studied the nucleon-nucleon systems extensively. In what follows we shall briefly summarize the pp and np experimental investigations at intermediate and high energies respectively.

In order to completely describe the NN system of isospin $I = 1$ around 1 GeV, Saclay and Gatchina performed series of polarized pp experiments in the 80's of last century. In 1985, the NN collaboration at Saclay measured a set of analyzing powers and spin correlation coefficients of pp scattering in the angular region of $45° < \theta_{cm} < 90°$ at 834，874，934，995 and 11095 MeV [24] using the polarized proton beam provided by SATURNE II and the polarized solid target [21], which was supplemented by Gatchina's measurements of the same observables between 35° and 95° at 690，850，890 and 950 MeV [25]. In addition, Gatchina also measured several spin transfer coefficients at 800，850，900，970 MeV using both vertically and horizontally polarized beams in conjunction with the polarized solid target [26, 27]. In late 1980's, SATURNE II –NN collaboration carried out systematic measurements of 15 spin observables of pp scattering at 11 energies

between 0.84 and 2.7 GeV, collected more than 3000 data [28]. In order to search for dibrayon, KEK and SATURNE II studied the distribution of the analyzing power of pp scattering with respect to the center-of-mass energy at 1-3 GeV and 0.655-1.017 GeV respectively. KEK found two distinct resonant structures at the invariant mass of proton pair $M_{pp} = 2.16$, 1.129 GeV [29], while the SATURNE data showed that the analyzing power distributed smoothly below 1 GeV [30]. The internal target detector EDDA built in the middle of 1990s at COSY was a dedicated spectrometer for pp study. From 1997 to 2005 the EDDA collaboration published series of pp data of $30° < \theta_{cm} < 90°$ at 500-2500 MeV, which include the unpolarized differential cross section [31], the analyzing powers [32] and the spin correlation coefficients [33–35]. Those high-precision data had imposed great impact on the pp database. At high-energy regions, CERN and BNL measured the dependences of the analyzing power and the spin correlation coefficient on the transverse momentum at 18-28 GeV/c, which manifested strong resonance at large transverse momenta [36, 37]. This phenomenon indicates that the spin dependence of the nuclear force decreases at large transverse momenta, which has not been satisfactorily interpreted yet.

The investigations on np scattering are much scarcer in comparison with the pp case. Using free neutron beams produced by (un)polarized deuteron breakup on Be target, the SATURNE II–IKAR collaboration measured the unpolarized differential cross section [11] as well as the neutron analyzing power [10, 11] of np scattering between 378 and 1135 MeV. SATURNE II–NN collaboration measured 11 spin observables of the np scattering between 312 and 1100 MeV, as results large amount of data were accumulated [38, 39]. Most of the data in their research were measured with free polarized neutron beam while some data were also collected with the quasi free neutron inside deuteron. Remarkably, the free neutron data and the quasi-free neutron data were in consistent with each other, which meant dueteron could be used as neutron source. In order to check isospin invariance of nuclear force Indinan university and TRIUMF measured both analyzing powers and spin correlation coefficients of np scattering at 181 MeV and 477 MeV respectively [40, 41], both of their results indicated that the nuclear force were not completely charge independent. Los Alamos also performed measurements of np spin correlation coefficients [42, 43].

The above summary shows that great efforts have been put on the nucleon–nucleon scattering research, yielding lots of valuable data. Many databases and programme, such as SAID [44], NN-online [45], Saclay-Geneva PSA [46] and

Bonn-Gatchina PWA [47] etc., have been developed to analysis and interpreter these experimental data. Thanks to the wealth of experimental data and theoretical analyses, the scattering amplitudes of pp scattering below 2 GeV are known with little ambiguity. On the contrast, due to lack of experimental data the phase-shift analyses can be performed only upto 1.3 GeV with large uncertainties above 800 MeV. Therefore, better understanding of the nuclear force demands further investigations at specific energies and in specific kinematical regions where measurements can impact the PSA significantly.

1.3 Complete Description of a Nuclear Reaction

One of the important features of the nuclear force is that it is spin dependent, which has been realized long before. In principle one can not acquire sufficient information on the spin dependence through unpolarized experiments since the spin effects are averaged out. Therefore the polarized experiments have to be performed in order to investigate the spin dependence of nuclear force. A general description of a nuclear reaction[3] is given from the point view of experiment. First the density matrix and its expansions, as well as the polarizations which characterize the polarized ensembles are discussed in section 1.3.1. In the following section, the M matrix which represents the dynamical process is discussed, and the corresponding cross section are also derived, all the experimental observables are contained in the cross section. Finally the necessary measurements are briefly discussed. Note even though the subscription given in this section is particularly for the polarized experiments, it also applies to the unpolarized cases, as the unpolarized case itself is actually a special polarized cases.

1.3.1 Polarized Ensemble: Density Operator and Polarizations

For an ensemble of identical particles with spin $\vec{S}$, imagine there are n different quantum states which are represented respectively by their spin wave functions ψ_i (where $i = 0, ..., n$), each with probability f_i of being occupied. If one performs a number of measurements of an observable $\hat{A}$ on this ensemble, the result[4] then is the weighted average of the expectation values of all the occupied states, which

---

[3]In this thesis, the phrase "reaction"also means "scattering ".

[4]For convenience, hereafter we express the measurement result of an observable on an ensemble as **ensemble expectation.**

reads

$$\langle A \rangle = \sum_{i=1}^{n} f_i \langle \psi_i | \hat{A} | \psi_i \rangle. \tag{1.3}$$

Insert the unit operator $\hat{I} = \sum_{k}^{2S+1} |k\rangle \langle k|$ into Eq. 1.3, $\langle A \rangle$ can be rewritten as

$$
\begin{aligned}
\langle A \rangle &= \sum_{i=1}^{n} f_i \sum_{m=1}^{2S+1} \sum_{k=1}^{2S+1} \langle \psi_i | m \rangle \langle m | \hat{A} | k \rangle \langle k | \psi_i \rangle \\
&= \sum_{i=1}^{n} f_i \sum_{m=1}^{2S+1} \sum_{k=1}^{2S+1} \langle k | \psi_i \rangle \langle \psi_i | m \rangle \langle m | \hat{A} | k \rangle \\
&= \sum_{m=1}^{2S+1} \sum_{k=1}^{2S+1} \langle k | \sum_{i=1}^{n} f_i | \psi_i \rangle \langle \psi_i | m \rangle \langle m | \hat{A} | k \rangle \\
&= \sum_{k=1}^{2S+1} \langle k = 1 | \sum_{i}^{n} f_i | \psi_i \rangle \langle \psi_i | \hat{A} | k \rangle \\
&= Tr \Big(\sum_{i=1}^{n} f_i | \psi_i \rangle \langle \psi_i | \hat{A} \Big).
\end{aligned} \tag{1.4}
$$

Based on above derivation one can conclude that the ensemble expectation of an observable $\hat{A}$ on a ensemble can be calculated as the trace of its product with the operator $\sum_{i}^{n} f_i | \psi_i \rangle \langle \psi_i |$. Since the physical state of a quantum system is completely[5] determined by the expectations of a complete set of Hermitian operators, an ensemble is described as completely as possible by its density operator

$$\hat{\rho} =: \sum_{i=1}^{n} f_i | \psi_i \rangle \langle \psi_i |. \tag{1.5}$$

With this definition, the ensemble expectation of an observable $\hat{A}$ can be calculated as

$$\langle A \rangle = Tr(\hat{\rho}\hat{A}) \tag{1.6}$$

However, since the wave functions $|\psi_i\rangle$ are usually unknown for an ensemble, the density operator is not suitable for the experiments. It is convenient to expand it into some measurable quantities. It is obvious that the density is Hermitian, i.e. $\rho = \rho^{\dagger}$.

In the spin space, the density operator is represented by a $(2S+1) \times (2S+1)$ matrix, which is named as density matrix and denoted by ρ. The density matrix can be expanded into any complete set of base matrices, $(2S+1)^2$ base matrices

---

[5]Actually the phase can not be determined by the expectation, however we still use the phrase "completely" because the phase doesn't play a role in the measurement.

$\mathscr{P}_j$ are needed since there $(2S + 1)^2$ matrix elements for ρ. These base matrices are required to be Hermitian ($\mathscr{P}_j = \mathscr{P}_j^\dagger$) so that they represent experimental observables. For simplicity, the base matrices are required to be orthogonal to each other, i.e.

$$Tr\left(\mathscr{P}_j \mathscr{P}_k^\dagger\right) = Tr\left(\mathscr{P}_j \mathscr{P}_k\right) = (2S + 1)\delta_{jk} \tag{1.7}$$

where $2S+1$ is the conventional normalization coefficient. Generally the expansion of a density matrix ρ is expressed as

$$\rho = \frac{1}{2S + 1} \sum_{j=1}^{(2S+1)^2} P_j \mathscr{P}_j. \tag{1.8}$$

The one-to-one correspondence relation between operator and matrix suggests there is an operator $\hat{\mathscr{P}}_j$ for every bases matrix $\mathscr{P}_j$, whose expectation is calculated as

$$Tr\left(\hat{\rho}\hat{\mathscr{P}}_j\right) = Tr\left(\frac{1}{2S + 1} \sum_{k=1}^{(2S+1)^2} P_k \mathscr{P}_k \mathscr{P}_j\right) = \frac{1}{2S + 1} \sum_{k=1}^{(2S+1)^2} P_k Tr\left(\mathscr{P}_k \mathscr{P}_j\right) = P_j. \tag{1.9}$$

It can be seen from above derivation that the expansion coefficients P_j in Eq. 1.8 are the ensemble expectations of the base matrices $\mathscr{P}_j$. These coefficients are able to describe an spin ensemble in the form of measurable observables, they are defined as the polarizations of the spin ensemble (beam or target). The most conventional expansions are the Cartesian and spherical expansions. The spherical expansion are more suitable in the cases of high spins. In the following subsections the Cartesian expansions for the particles of $spin = \frac{1}{2}$ and $spin = 1$ are given.

1.3.1.1 Cartesian Expansion of Density Operator for $S = \frac{1}{2}$

For the particles of $spin = \frac{1}{2}$ four orthogonal matrices are needed to expand the density matrix. The the unit matrix together with the Pauli spin matrices are used as the bases, which read

$$\mathscr{P}_1 = I = \begin{pmatrix} 1 & 0 \\ 0 & 1 \end{pmatrix} \tag{1.10a}$$

$$\mathscr{P}_2 = \sigma_x = \begin{pmatrix} 0 & 1 \\ 1 & 0 \end{pmatrix} \quad \mathscr{P}_3 = \sigma_y = \begin{pmatrix} 0 & -i \\ i & 0 \end{pmatrix} \quad \mathscr{P}_4 = \sigma_z = \begin{pmatrix} 1 & 0 \\ 0 & -1 \end{pmatrix} \quad (1.10b)$$

Insert above bases into the general formula Eq. 1.8, the density matrix of $spin - \frac{1}{2}$ is written as

$$\rho = \frac{1}{2}(1 + P_x \sigma_x + P_y \sigma_y + P_z \sigma_z) \quad (1.11)$$

where p_x, p_y and p_z are the familiar vector polarizations which are commonly used. For example if the quantization axis is taken along the z axis of a Cartesian coordinate, then the polarization P_z is related to experiment by

$$P_z = \frac{N^\uparrow - N^\downarrow}{N^\uparrow + N^\downarrow} \quad (1.12)$$

where $N^\uparrow$ and $N^\downarrow$ stand for the number of particles with spin projected along and opposite the z axis respectively. The same is true for P_x and P_y.

1.3.1.2 Cartesian Expansion of Density Operator for $S = 1$

In principle nine base matrices are needed for the expansion of the density matrix of $spin - 1$ ensembles. Unlike the case of $spin - \frac{1}{2}$, five more matrices have to be constructed except for the unit and angular momentum matrices

$$I = \begin{pmatrix} 1 & 0 & 0 \\ 0 & 1 & 0 \\ 0 & 0 & 1 \end{pmatrix} \quad (1.13a)$$

and

$$\mathscr{P}_x = S_x = \frac{1}{\sqrt{2}} \begin{pmatrix} 0 & 1 & 0 \\ 1 & 0 & 1 \\ 0 & 1 & 0 \end{pmatrix} \quad \mathscr{P}_y = S_y = \frac{1}{\sqrt{2}} \begin{pmatrix} 0 & -i & 0 \\ i & 0 & -i \\ 0 & i & 0 \end{pmatrix} \quad \mathscr{P}_z = S_z = \begin{pmatrix} 1 & 0 & 0 \\ 0 & 0 & 0 \\ 0 & 0 & -1 \end{pmatrix}$$
$$(1.13b)$$

which are tensor of $rank - 0$ (scalar) and tensors of $rank - 1$ (vector) respectively. Looking from the perspective of mathematics, the number of complete orthogonal bases of a tensor of $rank - k$ is $2k + 1$. Given there are 1 scalar (Eq. 1.13a) and 3 vector[6] (Eq. 1.13b) bases already, the remaining bases of the density must be tensors of $rank - 2$. Mathematically，a tensor of $rank - 2$ could be constructed

---

[6]Note the three matrices in Eq. 1.13b is normal to each other

as the out product of two vectors. In what follows, we shall discuss the procedure of seeking the bases, and finally give the prescription. As the first step the out product of two matrices of angular momentum from Eq. 1.13b, e.g. S_i and S_j are expressed as one symmetric term and asymmetric term:

$$S_i S_j = \frac{1}{2}(S_i S_j + S_j S_i) + \frac{1}{2}(S_i S_j - S_j S_i). \tag{1.14}$$

In view of the commutation between the angular momenta S_i and S_j:

$$S_i S_j - S_j S_i = i\varepsilon_{ijk}S_k \tag{1.15}$$

one finds out the asymmetric term does not provide a second order tensor but a vector S_k (multiplied by a constant) which is a known base matrix. Therefore we discard the asymmetric term and keep the symmetric one. As result, the new tensor is formed:

$$S_{ij} = \frac{1}{2}(S_i S_j + S_j S_i) \tag{1.16}$$

From the discussion in last subsection we know that the ensemble expectation of a base matrix is the polarization that corresponds to the base matrix, thus it is natural to expect the ensemble expectation be 0 for an unpolarized ensemble. So an base matrix ought to be traceless. The tenors defined in Eq. 1.16 don't meet this requirement. By transforming S_{ij} further, the traceless tensors are obtained:

$$\mathscr{P}_{ij} = 3S_{ij} - 2\delta_{ij}I \tag{1.17}$$

where I is the 3×3 unit matrix. Beside the above requirement, the normalization condition 1.7, i.e. $Tr(\mathscr{P}_j\mathscr{P}_k) = 3\delta_{jk}$ should also be satisfied, so the normalization factors $\sqrt{\frac{3}{Tr(\mathscr{P}_{ij}\mathscr{P}_{ij})}}$ are multiplied to $\mathscr{P}_{ij}$ and $\sqrt{\frac{3}{Tr(S_iS_i)}}$ are multiplied to the matrices in Eq. 1.13b. Finally we get totally ten matrices including the unit matrix, which are given below.

$$\mathscr{P}_1 = I = \begin{pmatrix} 1 & 0 & 0 \\ 0 & 1 & 0 \\ 0 & 0 & 1 \end{pmatrix} \tag{1.18a}$$

$$\mathscr{P}_2 = \sqrt{\frac{3}{2}}\,\mathscr{P}_x = \frac{\sqrt{3}}{2}\begin{pmatrix} 0 & 1 & 0 \\ 1 & 0 & 1 \\ 0 & 1 & 0 \end{pmatrix} \tag{1.18b}$$

$$\mathscr{P}_3 = \sqrt{\frac{3}{2}}\,\mathscr{P}_y = \frac{\sqrt{3}}{2}\begin{pmatrix} 0 & -i & 0 \\ i & 0 & -i \\ 0 & i & 0 \end{pmatrix} \tag{1.18c}$$

$$\mathscr{P}_4 = \sqrt{\frac{3}{2}}\,\mathscr{P}_z = \sqrt{\frac{3}{2}}\begin{pmatrix} 1 & 0 & 0 \\ 0 & 0 & 0 \\ 0 & 0 & -1 \end{pmatrix} \tag{1.18d}$$

$$\mathscr{P}_5 = \sqrt{\frac{2}{3}}\,\mathscr{P}_{xy} = \sqrt{\frac{3}{2}}\begin{pmatrix} 0 & 0 & -i \\ 0 & 0 & 0 \\ i & 0 & 0 \end{pmatrix} \tag{1.18e}$$

$$\mathscr{P}_6 = \sqrt{\frac{2}{3}}\,\mathscr{P}_{yz} = \frac{1}{2\sqrt{3}}\begin{pmatrix} 0 & 1 & 0 \\ 1 & 0 & -1 \\ 0 & -1 & 0 \end{pmatrix} \tag{1.18f}$$

$$\mathscr{P}_7 = \sqrt{\frac{2}{3}}\,\mathscr{P}_{zx} = \frac{\sqrt{3}}{2}\begin{pmatrix} 0 & -i & 0 \\ i & 0 & i \\ 0 & -i & 0 \end{pmatrix} \tag{1.18g}$$

$$\mathscr{P}_8 = \sqrt{\frac{1}{2}}\,\mathscr{P}_{xx} = \sqrt{\frac{1}{8}}\begin{pmatrix} -1 & 0 & 3 \\ 0 & 2 & 0 \\ 3 & 0 & -1 \end{pmatrix} \tag{1.18h}$$

$$\mathscr{P}_9 = \sqrt{\frac{1}{2}}\mathscr{P}_{yy} = \sqrt{\frac{1}{8}}\begin{pmatrix} -1 & 0 & -3 \\ 0 & 2 & 0 \\ -3 & 0 & -1 \end{pmatrix} \tag{1.18i}$$

$$\mathscr{P}_{10} = \sqrt{\frac{1}{2}}\mathscr{P}_{zz} = \sqrt{\frac{1}{2}}\begin{pmatrix} 1 & 0 & 0 \\ 0 & -2 & 0 \\ 0 & 0 & 1 \end{pmatrix} \tag{1.18j}$$

With the prescription give above the density of ensembles composed of spin-1 particles is expanded as

$$\begin{aligned}
\rho = \frac{1}{3}\{ &I + \frac{3}{2}(P_x\mathscr{P}_x + P_y\mathscr{P}_y + P_z\mathscr{P}_z) \\
&+ \frac{2}{3}(P_{xy}\mathscr{P}_{xy} + P_{yz}\mathscr{P}_{yz} + P_{zx}\mathscr{P}_{zx}) + \frac{1}{3}(P_{xx}\mathscr{P}_{xx} + P_{yy}\mathscr{P}_{yy} + P_{zz}\mathscr{P}_{zz})\}
\end{aligned} \tag{1.19}$$

where P_i in the first row are the vector polarizations while P_{ij} in the second row are the tensor polarizations. They are named vector and tensor polarizations because their corresponding base matrices $\mathscr{P}_i$ and $\mathscr{P}_{ij}$ rotate in the spin space as vector and tensor respectively. Again the polarizations defined here are identical to the commonly used definition. For example if the quantization axis is taken along the z axis of a Cartesian coordinate, then the vector polarization is

$$P_z = \frac{N^\uparrow - N^\downarrow}{N^\uparrow + N^\downarrow} \tag{1.20}$$

and the tensor polarizarion is

$$P_{zz} = \frac{N^\uparrow + N^\downarrow - 2N^0}{N^\uparrow + N^0 + N^\downarrow} \tag{1.21}$$

where $N^\uparrow$, $N^\downarrow$ and N_0 denote the number of particles with spin up, down and sideways respectively.

As mentioned before, nine orthogonal matrices are sufficient to expand the density matrix of a spin-1 ensemble. Instead, there are ten base matrices constructed from above procedure, so the bases matrices listed above are not completely independent. In fact the independent bases are P_{xx}, P_{yy} and P_{zz}, the relation

among them is

$$\mathscr{P}_{xx} + \mathscr{P}_{yy} + \mathscr{P}_{zz} = \begin{pmatrix} 0 & 0 & 0 \\ 0 & 0 & 0 \\ 0 & 0 & 0 \end{pmatrix} \tag{1.22}$$

It is evident that with this relation, the last three base matrices in 1.18 can be substituted by any of the following combinations,

$$(\mathscr{P}_{xx} - \mathscr{P}_{yy}, \quad \mathscr{P}_{zz}), \quad (\mathscr{P}_{yy} - \mathscr{P}_{zz}, \quad \mathscr{P}_{xx}), \quad (\mathscr{P}_{zz} - \mathscr{P}_{xx}, \quad \mathscr{P}_{yy}). \tag{1.23}$$

The density matrix can be rewritten by using for instance the first combination $(\mathscr{P}_{xx} - \mathscr{P}_{yy}, \quad \mathscr{P}_{zz})$ as

$$\begin{aligned} \rho = \frac{1}{3}\{I + &\frac{3}{2}(P_x\mathscr{P}_x + P_y\mathscr{P}_y + P_z\mathscr{P}_z) \\ &+ \frac{2}{3}(P_{xy}\mathscr{P}_{xy} + P_{yz}\mathscr{P}_{yz} + P_{zx}\mathscr{P}_{zx}) + \frac{1}{6}(P_{xx} - P_{yy})(\mathscr{P}_{xx} - \mathscr{P}_{yy}) + \frac{1}{2}P_{zz}\mathscr{P}_{zz}\} \end{aligned} \tag{1.24}$$

1.3.2 Dynamics: M Matrix and Cross Section

Having given the prescription of describing a spin ensemble in last subsection, it is ripe now to deal with the nuclear reactions involving particles with spin. Consider a process with two particles in both the entrance and exit states

$$a + b \rightarrow c + d \tag{1.25}$$

whose wave functions of the initial and and final states are $\psi_i = \psi_a \otimes \psi_b$ and $\psi_f = \psi_c \otimes \psi_d$ respectively. Provided the dynamical process which transforms the initial system into the final system is described by the operator S, i.e. $\psi_f = S\psi_i$, the density matrix of the final system ρ_F is derived from the initial density matrix ρ_i as

$$\rho_F = S\rho_i S^\dagger \tag{1.26}$$

as the density matrices are tensors in the spin space. Considering the particles which didn't participate the interaction, the operator S should be substituted with $R = S - 1$. Therefore, instead of ρ_F, the density matrix which directly relevant to the experimental observables is

$$\rho_f = R\rho_i R^\dagger. \tag{1.27}$$

So far the discussion is only confined in the spin space. The momentum degree of freedom has also to be taken into account to completely describe an experiment. Suppose the initial and final relative momenta[7] are $\vec{k}_i$ and $\vec{k}_f$, and the corresponding wave functions in the momentum space are denoted by $\left|\vec{k}_i\right\rangle$ and $\left|\vec{k}_f\right\rangle$. The initial density matrix in the case of a specific momentum state $\left|\vec{k}_i\right\rangle$ is

$$\rho_i(\vec{k}_i) = \left\langle \vec{k}_i \right| \rho_i \left| \vec{k}_i \right\rangle, \tag{1.28}$$

it is essentially a diagonal element of the general density matrix ρ_i in the momentum space. On the dynamical side, the operator R which characterizes the dynamical process is also represented by a matrix in the momentum space. Likewise, the matrix element of this matrix, for instance $\left\langle \vec{k}_f \right| R \left| \vec{k}_i \right\rangle$, is also a matrix in the spin space, whose elements, if multiplied by the normalization factor, are in turn the amplitudes for individual initial and final spin states. Conventionally, the spin matrix $\left\langle \vec{k}_f \right| R \left| \vec{k}_i \right\rangle$ multiplied the normalized factor is denoted as $M(\vec{k}_f, \vec{k}_i)$. Finally the density matrix for the final momentum state $\vec{k}_f$ becomes

$$\rho_f(\vec{k}_f) = M(\vec{k}_f, \vec{k}_i)\rho_i(\vec{k}_i)M^\dagger(\vec{k}_f, \vec{k}_i) \tag{1.29}$$

With above notations the differential cross section, which is defined as the intensity of the outgoing particles normalized by the incident intensity[8], is expressed as

$$\frac{d\sigma}{d\Omega}(\theta, \phi) = \frac{Tr\rho_f(\vec{k}_f)}{Tr\rho_i(\vec{k}_i)} = \frac{TrM(\vec{k}_f, \vec{k}_i)\rho_i(\vec{k}_i)M^\dagger(\vec{k}_f, \vec{k}_i)}{Tr\rho_i(\vec{k}_i)} \tag{1.30}$$

The purpose of investigating a reaction is to uncover the law behind the dynamical process, the only way is to compare our understanding and hypothesis about the law, which are generalized as theory, with the fact, namely the experiment. In Eq. 1.30 the experimental observable is the cross section $\frac{d\sigma}{d\Omega}$, it is expressed in the form of the M matrix, which can be derived from the theory, in this sense the comparison between experiment and theory could in principle be performed. However the relation between cross section and M matrix expressed by Eq. 1.30 is too abstract, it would be convenient if this relation can be more factorized. The expansion of M matrix for NN scattering in terms of several scalar amplitudes

---

[7]For simplicity, "relative momentum"is referred as "momentum"in the following.

[8]The intensity of an ensemble described by the density matrix ρ is calculated as the expectation value of the unity matrix I, i.e. $Tr\rho I = Tr\rho$.

is given in section 1.3.2.1. The polarized differential cross section in the form of variant spin observables are discussed in section 1.3.2.2.

1.3.2.1 Expansion of M Matrix for NN Interaction

As a tensor in the spin space, the M matrix can be expanded in the base matrices, just as the expansion of density matrix. Since the object of this thesis is studying the nucleon-nucleon system, the expansion is only given for NN scattering. In the center-of-mass system, the M matrix $M(\vec{k}_f, \vec{k}_i)$ only depends the initial and final momenta, for simplicity, the M matrix and the expansion are expressed as functions of the momentum transfer $\vec{q}$. For a system composed of two identical spin-$\frac{1}{2}$ particles the M matrix is expanded as

$$
\begin{aligned}
M(\vec{q}) =& \alpha(\vec{q}) + i\gamma(\vec{q})(\vec{\sigma}_1 + \vec{\sigma}_2)\cdot\hat{n} + \beta(\vec{q})(\vec{\sigma}_1\cdot\hat{n})(\vec{\sigma}_2\cdot\hat{n}) \\
& + \delta(\vec{q})(\vec{\sigma}_1\cdot\hat{m})(\vec{\sigma}_2\cdot\hat{m}) + \varepsilon(\vec{q})(\vec{\sigma}_1\cdot\hat{l})(\vec{\sigma}_2\cdot\hat{l})
\end{aligned}
\tag{1.31}
$$

if the the system is invariant under rotation, spatial reflection and time reversal [48]. In the above expansion $\vec{\sigma}_1$ and $\vec{\sigma}_1$ are the Pauli matrices acting on the wave functions of the two nucleons respectively. The unit vectors in Eq. 1.31 is defined in terms of the initial and final momenta $\vec{k}_i$ and $\vec{k}_f$:

$$
\hat{l} = \frac{\vec{k}_i + \vec{k}_f}{|\vec{k}_i + \vec{k}_f|}, \quad \hat{m} = \frac{\vec{k}_f - \vec{k}_i}{|\vec{k}_f - \vec{k}_i|}, \quad \hat{n} = \frac{\vec{k}_i \times \vec{k}_f}{|\vec{k}_i \times \vec{k}_f|}.
\tag{1.32}
$$

Evidently, these unit vectors are orthogonal among each other. This expansion is applicable for both proton-proton (pp) and neutron-proton (np) systems, provided the isospin invariance is maintained strictly.

1.3.2.2 Cross Section in Form of Spin Observables

In this subsection we shall introduce the spin observables by decomposing the differential cross section (defined in Eq. 1.30). Note the initial density matrix of the reaction $a + b \to c + d$ is the direct product of the density matrices of particle a and b, i.e. $\rho_i(\vec{k}_i) = \rho_a(\vec{k}_i) \otimes \rho_b(\vec{k}_i)$, it can be expanded according to Eq. 1.8 as[9]

$$
\rho_i = \frac{1}{(2S_a + 1)(2S_b + 1)} \sum_{j_a=1}^{(2S_a+1)^2} \sum_{j_b=1}^{(2S_b+1)^2} P_{j_a}^a P_{j_b}^b \mathscr{P}_{j_a}^a \mathscr{P}_{j_b}^b.
\tag{1.33}
$$

---

[9]To shorten the formulae, the dependences on momentum is not written out explicitly sometimes.

Substitute the density matrix $\rho_i(\vec{k}_i)$ in Eq. 1.30 with above expression, one obtains

$$
\begin{aligned}
\frac{d\sigma}{d\Omega} &= \frac{TrM\rho_i M^\dagger}{Tr\rho_i} \\
&= \frac{1}{(2S_a+1)(2S_b+1)} \frac{1}{Tr\rho_i} Tr \sum_{j_a=1} \sum_{j_b=1} P^a_{j_a} P^b_{j_b} M \mathscr{P}^a_{j_a} \mathscr{P}^b_{j_b} M^\dagger \\
&= \frac{1}{(2S_a+1)(2S_b+1)} \frac{1}{Tr\rho_i} \left[TrMM^\dagger \right. \\
&\qquad + \sum_{j_a=1} P^a_{j_a} TrM \mathscr{P}^a_{j_a} M^\dagger + \sum_{j_a=1} P^b_{j_b} TrM \mathscr{P}^b_{j_b} M^\dagger \\
&\qquad \left. + \sum_{j_a=1} \sum_{j_b=1} P^a_{j_a} P^b_{j_b} TrM \mathscr{P}^a_{j_a} \mathscr{P}^b_{j_b} M^\dagger \right].
\end{aligned}
$$
$$(1.34)$$

It has already been demonstrated by Eq. 1.9 that $P^a_{j_a}$ and $P^b_{j_b}$ are polarizations of ensembles a and b respectively, thus for an unpolarized experiment above formula reduces to

$$
\frac{d\sigma}{d\Omega}^0 = \frac{TrMM^\dagger}{(2S_a+1)(2S_b+1)Tr\rho_i} \tag{1.35}
$$

which is the usual unpolarized cross section. Utilizing the expression of unpolarized cross section Eq. 1.35, Eq. 1.34 can be rewritten as

$$
\frac{d\sigma}{d\Omega} = \frac{d\sigma}{d\Omega}^0 \left[1 + \sum_{j_a=1} P^a_{j_a} \frac{TrM \mathscr{P}^a_{j_a} M^\dagger}{TrMM^\dagger} + \sum_{j_b=1} P^b_{j_b} \frac{TrM \mathscr{P}^b_{j_b} M^\dagger}{TrMM^\dagger} \right.
$$
$$
\left. + \sum_{j_a=1} \sum_{j_b=1} P^a_{j_a} P^b_{j_b} \frac{TrM \mathscr{P}^a_{j_a} \mathscr{P}^b_{j_b} M^\dagger}{TrMM^\dagger} \right]. \tag{1.36}
$$

Compared with the unpolarized cross section Eq. 1.35, the polarized cross section contains some extra terms, each of these terms is a product of certain polarization(s) and a quantity composed of the dynamical M matrix and the base matrix(s) corresponding to the polarization(s). Take the term $P^a_{j_a} \frac{TrM \mathscr{P}^a_{j_a} M^\dagger}{TrMM^\dagger}$ as example, $P^a_{j_a}$ is a polarization component characterizing ensemble a and $\frac{TrM \mathscr{P}^a_{j_a} M^\dagger}{TrMM^\dagger}$ contains the dynamical information, which measures how the reaction $a + b \to c + d$ is influenced by this polarization component. Conventionally $\frac{TrM \mathscr{P}^a_{j_a} M^\dagger}{TrMM^\dagger}$ and $\frac{TrM \mathscr{P}^b_{j_b} M^\dagger}{TrMM^\dagger}$ are defined as analyzing powers, while $\frac{TrM \mathscr{P}^a_{j_a} \mathscr{P}^b_{j_b} M^\dagger}{TrMM^\dagger}$ is called spin correlation coefficient.

Since the nuclear force is spin dependent, the particles from the exit channel

(c and d in our case) are usually polarized, even in an unpolarized experiment. Therefore the spin dependence of the nuclear force can be also investigated via measuring the polarization(s) of the outgoing particle(s). By definition the polarization component corresponding to a density matrix base $\mathscr{P}^c_{j_c}$ is[10]

$$P^c_{j_c} = \frac{Tr\rho_f \mathscr{P}^c_{j_c}}{Tr\rho_f}.$$ (1.37)

Together with the definition of differential cross section (Eq. 1.30) it can be derived that

$$P^c_{j_c}\frac{d\sigma}{d\Omega}(\theta,\phi) = \frac{Tr\rho_f(\vec{k}_f)\mathscr{P}^c_{j_c}}{Tr\rho_i(\vec{k}_i)} = \frac{TrM(\vec{k}_f,\vec{k}_i)\rho_i(\vec{k}_i)M^\dagger(\vec{k}_f,\vec{k}_i)\mathscr{P}^c_{j_c}}{Tr\rho_i(\vec{k}_i)},$$ (1.38)

this expression can be expanded as

$$\begin{aligned}
P^c_{j_c}\frac{d\sigma}{d\Omega} = \frac{d\sigma}{d\Omega}^0 \Bigg[& \frac{TrMM^\dagger\mathscr{P}^c_{j_c}}{TrMM^\dagger} \\
& + \sum_{j_a=1} P^c_{j_c}P^a_{j_a}\frac{TrM\mathscr{P}^a_{j_a}M^\dagger\mathscr{P}^c_{j_c}}{TrMM^\dagger} + \sum_{j_b=1} P^c_{j_c}P^b_{j_b}\frac{TrM\mathscr{P}^b_{j_b}M^\dagger\mathscr{P}^c_{j_c}}{TrMM^\dagger} \\
& + \sum_{j_a=1}\sum_{j_b=1} P^c_{j_c}P^a_{j_a}P^b_{j_b}\frac{TrM\mathscr{P}^a_{j_a}\mathscr{P}^b_{j_b}M^\dagger\mathscr{P}^c_{j_c}}{TrMM^\dagger} \Bigg]
\end{aligned}$$

(1.39)

where the quantities containing the M matrix are spin observables. For example, $\frac{TrMM^\dagger\mathscr{P}^c_{j_c}}{TrMM^\dagger}$ is the polarization component of base $\mathscr{P}^c_{j_c}$ produced in a unpolarized experiment, thus is called polarizing power. $\frac{TrM\mathscr{P}^a_{j_a}M^\dagger\mathscr{P}^c_{j_c}}{TrMM^\dagger}$ is the polarization transfer coefficient which measures the influence of the polarization component $P^a_{j_a}$ of the initial particles a to the polarization component $P^c_{j_c}$ of the final particle c. It is possible to measure the spin correlation coefficient of the final particles when the polarizations of both the particles in the exit channel are measured in coincidence.

From above discussion we see some observables such like analyzing power and final polarization contain only one polarization, while some ones contain more. According to the number of polarization components involved, the observables can be classified as one-spin observables, two-spin observables, and so on. Usually more polarizations one observable contains, more difficult the measurement is. As

---

[10]Here the polarization of particle c is given as an example.

a summary, observables involving up to two spin components are listed below for reaction of type $a + b \rightarrow c + d$.

- Zero-spin observable.

  Unpolarized differential cross section:

  $$\frac{d\sigma}{d\Omega}^{0} = \frac{TrMM^{\dagger}}{(2S_a + 1)(2S_b + 1)Tr\rho_i}. \tag{1.40}$$

- One-spin observables.

  Analyzing powers:

  $$A^a_{j_a} = \frac{TrM\mathscr{P}^a_{j_a}M^{\dagger}}{TrMM^{\dagger}}, \tag{1.41a}$$

  $$A^b_{j_b} = \frac{TrM\mathscr{P}^b_{j_b}M^{\dagger}}{TrMM^{\dagger}}. \tag{1.41b}$$

  Polarizing powers:

  $$P^c_{j_c} = \frac{TrMM^{\dagger}\mathscr{P}^c_{j_c}}{TrMM^{\dagger}}, \tag{1.42a}$$

  $$P^d_{j_d} = \frac{TrMM^{\dagger}\mathscr{P}^d_{j_d}}{TrMM^{\dagger}}. \tag{1.42b}$$

- Two-spin observables:

  Spin correlation coefficients of entrance channel:

  $$C_{j_a,j_b} = \frac{TrM\mathscr{P}^a_{j_a}\mathscr{P}^b_{j_b}M^{\dagger}}{TrMM^{\dagger}}. \tag{1.43}$$

  Spin correlation coefficients of exit channel:

  $$C_{j_c,j_d} = \frac{TrMM^{\dagger}\mathscr{P}^c_{j_c}\mathscr{P}^d_{j_d}}{TrMM^{\dagger}}. \tag{1.44}$$

  Spin transfer coefficients:

  $$T^{j_c}_{j_a} = \frac{TrM\mathscr{P}^a_{j_a}M^{\dagger}\mathscr{P}^c_{j_c}}{TrMM^{\dagger}}, \tag{1.45a}$$

$$T_{j_a}^{j_d} = \frac{TrM\mathscr{P}_{j_a}^a M^\dagger \mathscr{P}_{j_d}^d}{TrMM^\dagger}, \tag{1.45b}$$

$$T_{j_b}^{j_c} = \frac{TrM\mathscr{P}_{j_b}^b M^\dagger \mathscr{P}_{j_c}^c}{TrMM^\dagger}, \tag{1.45c}$$

$$T_{j_b}^{j_d} = \frac{TrM\mathscr{P}_{j_b}^b M^\dagger \mathscr{P}_{j_d}^d}{TrMM^\dagger}. \tag{1.45d}$$

So far the polarized cross section as well as the spin observables for a two body reaction have been introduced. However, the cross section defined in Eq. 1.34 can not be directly compared with the experimental distributions. The reason is explained below. Note the formula for the differential cross section given by Eq. 1.34 is defined in the projectile helicity reference coordinate which is determined by the initial momentum $\vec{k}_i$ and the final momentum $\vec{k}_f$, while on the other hand, the (beam or/and target) polarizations are conveniently described in the laboratory reference coordinate, which is usually defined by the detectors. The polarizations in the laboratory coordinate are consistent for any given polarized ensembles, but on the contrary, in the helicity coordinate the polarizations are variant since $\vec{k}_f$ is different for each specific process. Fig. 1.2 depicts the relation between the laboratory frame XYZ and the projectile helicity frame $x'y'z'$. Both Z and z' are set along the incident momentum $\vec{k}_i$; y' is defined by the vector $\vec{k}_i \times \vec{k}_f$; the x' is
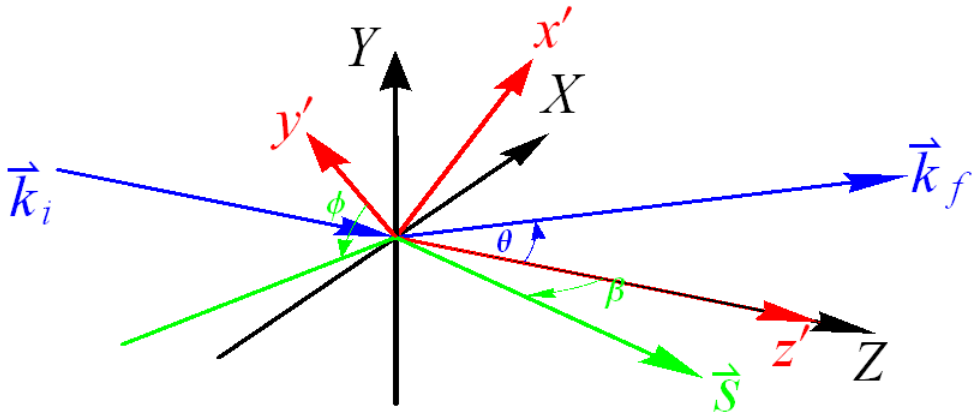
Figure 1.2: Relation between the laboratory coordinate system XYZ (drawn in black) and the projectile helicity coordinate system $x'y'z'$ (drawn in red). $\vec{k}_i$ and $\vec{k}_f$ represent the initial and final momenta respectively. Both Z and z' are parallel to $\vec{k}_i$; y' is defined by $\vec{k}_i \times \vec{k}_f$; $x'y'z'$ forms a right-hand coordinate system. The polarization quantization axis $\vec{S}$ is indicated (in green) as well, its spherical coordinate in the projectile helicity coordinate system is $(1, \beta, \phi)$.

chosen in such a manner that x', y' and z' forms a right-handed coordinate. The spin quantization axis of the polarized ensemble is parallel to an unit vector $\vec{S}$, which is described by the spherical coordinate $(1, \beta, \phi)$ in the projectile helicity coordinate system. The polarization is most conveniently described in a coordinate system xyz[11] where z axes is chosen to be parallel to the quantization axis $\vec{S}$, and x and y axes are taken arbitrarily in the plane which is perpendicular to $\vec{S}$ because of symmetry. For instance, in the case where the polarized ensemble is produced by a polarized atomic beam source (ABS)(refer Sec. 3.3.1) the z axis is parallel to the atomic beam direction. In the polarization system, the vector polarization only have z component. In view of the cylindrical symmetry and the anticommutativity between the angular momentum operators, it can be seen from Eq. 1.17 that there are only three nonvanishing tensor polarizations p_{zz}, p_{xx} and p_{yy}. Because $p_{xx} = p_{yy}$ and $p_{xx} + p_{yy} + p_{zz} = 0$[12], the relation

$$p_{xx} = p_{yy} = -\frac{1}{2}p_{zz} \tag{1.46}$$

holds. The transformation from the polarization system xyz to the projectile helicity system $x'y'z'$ is given by

$$\vec{p'} = T\vec{p} \tag{1.47}$$

for a polarization of the first-rank tensor (vector polarization) $\vec{p}$, and by

$$\overset{\leftrightarrow}{p'} = T\overset{\leftrightarrow}{p}\widetilde{T} \tag{1.48}$$

for a polarization of the second-rank tensor (tensor polarization) $\overset{\leftrightarrow}{p}$, with

$$T = \begin{pmatrix} T_{xx} & T_{xy} & -\sin\beta\cos\phi \\ T_{yx} & T_{yy} & \sin\beta\cos\phi \\ T_{xz} & T_{zy} & \cos\phi \end{pmatrix} \tag{1.49}$$

and $\widetilde{T}$ being the transposed matrix of T [49]. Note the matrix elements in the first and second columns of T are irrelevant to the transformation. The polarized differential cross section in the polarization frame is obtained by substituting the polarizations in Eq. 1.34 by the values calculated from Eq. 1.47 and 1.48. As

---

[11]In the present thesis this frame is referred as polarization (coordinate) system.
[12]which can be derived from the relation 1.22

examples, the cross sections in the polarization system of the single-polarized reactions of the types $\frac{\vec{1}}{2} + b \to c + d$ and $\vec{1} + b \to c + d$ are derived below.

The differential cross section of the reaction $\frac{\vec{1}}{2} + b \to c + d$ in the helicity coordinate is

$$\frac{d\sigma}{d\Omega} = \frac{d\sigma}{d\Omega}^0 \left[1 + p_{y'} A_y(\theta) \right]. \tag{1.50}$$

Note the analyzing powers A_x and A_y must vanish to preserve the parity conservation [48]. The vector polarizations in the helicity frame is deduced from Eq.1.47 as

$$p_{x'} = -p_z \sin\beta \sin\phi, \tag{1.51a}$$

$$p_{y'} = p_z \sin\beta \cos\phi, \tag{1.51b}$$

$$p_{z'} = p_z \cos\beta. \tag{1.51c}$$

Combining formulae 1.50 and 1.51b, one obtains the differential cross section of the reaction $\frac{\vec{1}}{2} + b \to c + d$ in the polarization system:

$$\frac{d\sigma}{d\Omega} = \frac{d\sigma}{d\Omega}^0 \left[1 + p_z \sin\beta \cos\phi A_y(\theta) \right]. \tag{1.52}$$

The differential cross section of the reactions induced by polarized spin-1 particle $\vec{1} + b \to c + d$ is

$$\frac{d\sigma}{d\Omega} = \frac{d\sigma}{d\Omega}^0 \left[1 + \frac{3}{2} p_{y'} A_y(\theta) + \frac{2}{3} p_{x'z'} A_{xz}(\theta) \right.$$
$$\left. + \frac{1}{3} p_{x'x'} A_{xx}(\theta) + \frac{1}{3} p_{y'y'} A_{yy}(\theta) + \frac{1}{3} p_{z'z'} A_{zz}(\theta) \right], \tag{1.53a}$$

or equivalently

$$\frac{d\sigma}{d\Omega} = \frac{d\sigma}{d\Omega}^0 \left[1 + \frac{3}{2} p_{y'} A_y(\theta) + \frac{2}{3} p_{x'z'} A_{xz}(\theta) \right.$$
$$\left. + \frac{1}{6} (p_{x'x'} - p_{y'y'})\{A_{xx}(\theta) - A_{yy}(\theta)\} + \frac{1}{2} p_{z'z'} A_{zz}(\theta) \right]. \tag{1.53b}$$

providing the parity conversation is maintained [48]. Similarly, by substituting the polarizations in Eq. 1.53 with

$$p_{x'y'} = -\frac{3}{2}\sin^2\beta\sin\phi\cos\phi p_{zz} \tag{1.54a}$$

$$p_{x'z'} = -\frac{3}{2}\sin\beta\cos\beta\sin\phi p_{zz} \tag{1.54b}$$

$$p_{y'z'} = \frac{3}{2}\sin\beta\cos\beta\cos\phi p_{zz} \tag{1.54c}$$

$$p_{x'x'} = \frac{1}{2}(3\sin^2\beta\sin^2\phi - 1)p_{zz} \tag{1.54d}$$

$$p_{y'y'} = \frac{1}{2}(3\sin^2\beta\cos^2\phi - 1)p_{zz} \tag{1.54e}$$

$$p_{z'z'} = \frac{1}{2}(3\cos^2\beta - 1)p_{zz} \tag{1.54f}$$

which are deduced from Eq. 1.48 and 1.46 , the differential cross section of single-polarized reactions $\vec{1} + b \rightarrow c + d$ in the polarization system is derived as

$$
\begin{aligned}
\frac{d\sigma}{d\Omega} = \frac{d\sigma}{d\Omega}^0 \Big[& 1 + \frac{3}{2}p_z\sin\beta\cos\phi A_y(\theta) - \sin\beta\cos\beta\sin\phi p_{zz}A_{xz}(\theta) \\
& + \frac{1}{6}(3\sin^2\beta\sin^2\phi - 1)p_{zz}A_{xx}(\theta) \\
& + \frac{1}{6}(3\sin^2\beta\cos^2\phi - 1)p_{zz}A_{yy}(\theta) \\
& + \frac{1}{6}(3\cos^2\beta - 1)p_{zz}A_{zz}(\theta) \Big]
\end{aligned}
\tag{1.55a}
$$

or

$$
\begin{aligned}
\frac{d\sigma}{d\Omega} = \frac{d\sigma}{d\Omega}^0 \Big\{ & 1 + \frac{3}{2}p_z\sin\beta\cos\phi A_y(\theta) - \frac{1}{2}\sin 2\beta\sin\phi p_{zz}A_{xz}(\theta) \\
& + \frac{1}{4}\sin^2\beta\cos 2\phi p_{zz}[A_{yy}(\theta) - A_{xx}(\theta)] + \frac{1}{4}(3\cos^2\beta - 1)p_{zz}A_{zz}(\theta) \Big\}.
\end{aligned}
\tag{1.55b}
$$

Chapter 2

Neutron-Proton Scattering Investigation at ANKE

In the first chapter we have stressed the physics motivation of the investigations of the nucleon-nucleon (NN) interaction, and also discussed the description of the nucleon-nucleon (NN) scattering at length, where our knowledge about the NN scattering is expressed as various observables and amplitudes. Many databases, such like SAID and NN-OnLine, were set up with the purpose of collecting and analyzing the data (of the observables and amplitudes) that have been accumulated over decades around the world. Besides their intrinsic importance for the understanding of the nuclear forces, these valuable data are also imperative elements in the study of the nuclear many-body system as well as the meson production. As mentioned in the previous chapter, theoretical models can be directly expressed in the term of amplitudes, and on the other hand, experimental observables are summarized as amplitudes through the phase-shift analysis (PSA). Fitting all the available NN scattering observables, the amplitudes up to a certain orbital angular momentum can be obtained by the phase-shift analysis (PSA), with the increase of the experimental observables, the amplitudes of higher orbital angular momenta will be obtained. Conversely, observables can be calculated from amplitudes using the impulse approximation. It is possible to deduce the amplitudes at the energies where no experiment has been conducted via extrapolation or utilizing the dispersion relation, thus predictions can be made for the unknown observables. It goes without saying that the more the experimental observables are exploited in the phase-shift analysis, the more precisely the amplitudes are extracted, the reverse is also true.

There exist large amount of data of observables of the proton-proton (p-p) scattering. As examples, the abundance plot of the unpolarized differential cross section and the analyzing power of the pp elastic scattering are presented in Fig. 2.1. Thanks to these valuable data, the phase-shift analyses of isospin $I = 1$ have yielded reliable amplitudes up to about 2 GeV.

(a) Unpolarized differential cross section $\frac{d\sigma}{d\Omega}$. (b) Analyzing power A_y.
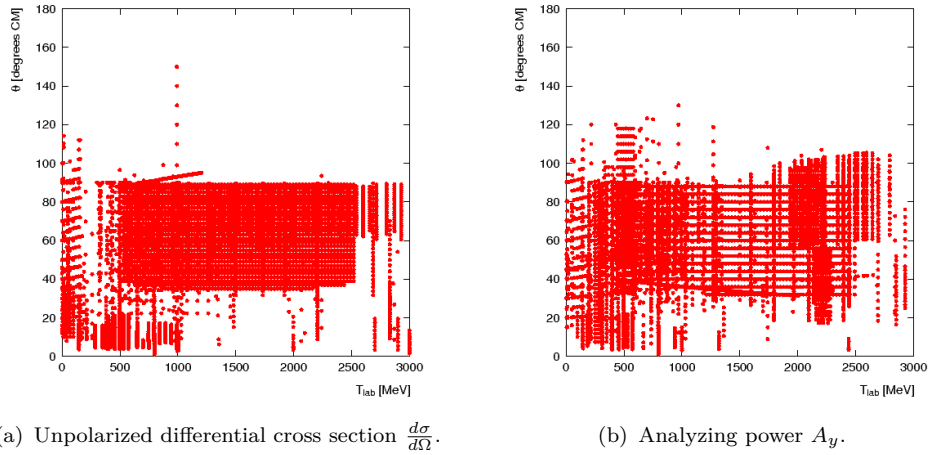
Figure 2.1: Abundance plots of the unpolarized differential cross section $\frac{d\sigma}{d\Omega}$ (left) and the analyzing power A_y (right) of the proton-proton elastic scattering in the kinetimatic regin of the scattering angle θ and the nucleon energy T_{lab} in the laboratory reference fram. Note the data located in the domain of $500 < T_{Lab} < 2500$ and $30° < \theta < 90°$ are contributed by EDDA at COSY.

Due to the difficulties with producing the neutron beams or targets of high quality and the neutron detection, the data of the neutron-proton (np) scattering are much less. For comparison, the abundance plots of the differential cross section and the analyzing powers are showed for the np scattering as well (Fig. 2.2). As can be seen, the data of np scattering are far more spare above 800 MeV. Base on these data, the phase-shift analyses of $I = 0$ can only be applied to 1.3 GeV，with large ambiguities above 800 MeV. It was proposed by Wilkin and Bugg that the information on the spin dependence of the neutron-proton elastic scattering at large angle can be learned by studying the deuteron charge-exchange on hydrogen. Using this method, the ANKE-Collaboration has been embarked on a comprehensive np scattering program for years.

We shall introduce the prescription of investigating the neutron-proton charge-exchange amplitudes from $dp \rightarrow \{pp\}n$ reaction in section 2.1. The results obtained in the first phase of the ANKE np program are summarized in section 2.2.

(a) Unpolarized differential cross section $\frac{d\sigma}{d\Omega}$.

(b) Analyzing power A_y.
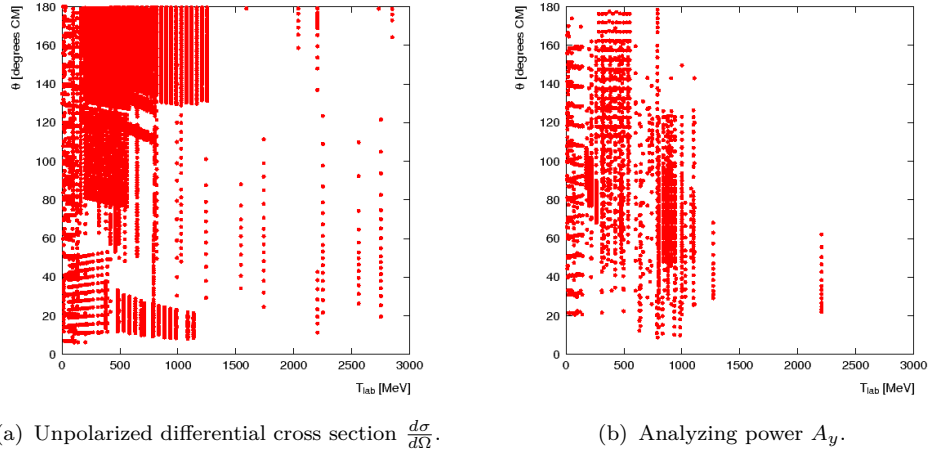
Figure 2.2: Abundance plots of the unpolarized differential cross section $\frac{d\sigma}{d\Omega}$ (left) and the analyzing power A_y (right) of the proton-proton elastic scattering in the kinetimatic regin of the scattering angle θ and the nucleon energy T_{lab} in the laboratory reference fram.

## 2.1 Impulse Approximation for Deuteron Charge Exchange on Proton

From the discussion in section 1.3.2 we know the neutron-proton scattering process can be described completely by a M matrix. Since the matrix elements of the M matrix are essentially the amplitudes corresponding to individual initial and final spin states, the M matrix is also called scattering amplitude. Here we designate it as $M_{np\to pn}$. In order to make the present discussion self-contained, we repeat the expansion of the np amplitude here:

$$M_{np\to pn} = \alpha(\vec{q}) + i\gamma(\vec{q})(\vec{\sigma}_1 + \vec{\sigma}_2)\cdot\hat{n} + \beta(\vec{q})(\vec{\sigma}_1\cdot\hat{n})(\vec{\sigma}_2\cdot\hat{n})$$
$$+ \delta(\vec{q})(\vec{\sigma}_1\cdot\hat{m})(\vec{\sigma}_2\cdot\hat{m}) + \varepsilon(\vec{q})(\vec{\sigma}_1\cdot\hat{l})(\vec{\sigma}_2\cdot\hat{l}), \tag{2.1}$$

where the three orthogonal unit vectors are defined by the initial $(\vec{k}_i)$ and final $(\vec{k}_f)$ momenta as

$$\hat{l} = \frac{\vec{k}_i + \vec{k}_f}{|\vec{k}_i + \vec{k}_f|}, \quad \hat{m} = \frac{\vec{k}_f - \vec{k}_i}{|\vec{k}_f - \vec{k}_i|}, \quad \hat{n} = \frac{\vec{k}_i \times \vec{k}_f}{|\vec{k}_i \times \vec{k}_f|}, \tag{2.2}$$

and $\vec{\sigma}_1$ and $\vec{\sigma}_2$ are the Pauli matrices between the neutron and proton spinors. It is seen form Eq. 2.1 that the np amplitude $M_{np\to pn}$ consists of five scalar amplitudes, which are the functions of the three-momentum transfer $\vec{q}$. α is the spin-independent amplitude, γ is the spin-orbit amplitude, and β, δ, and ε are the
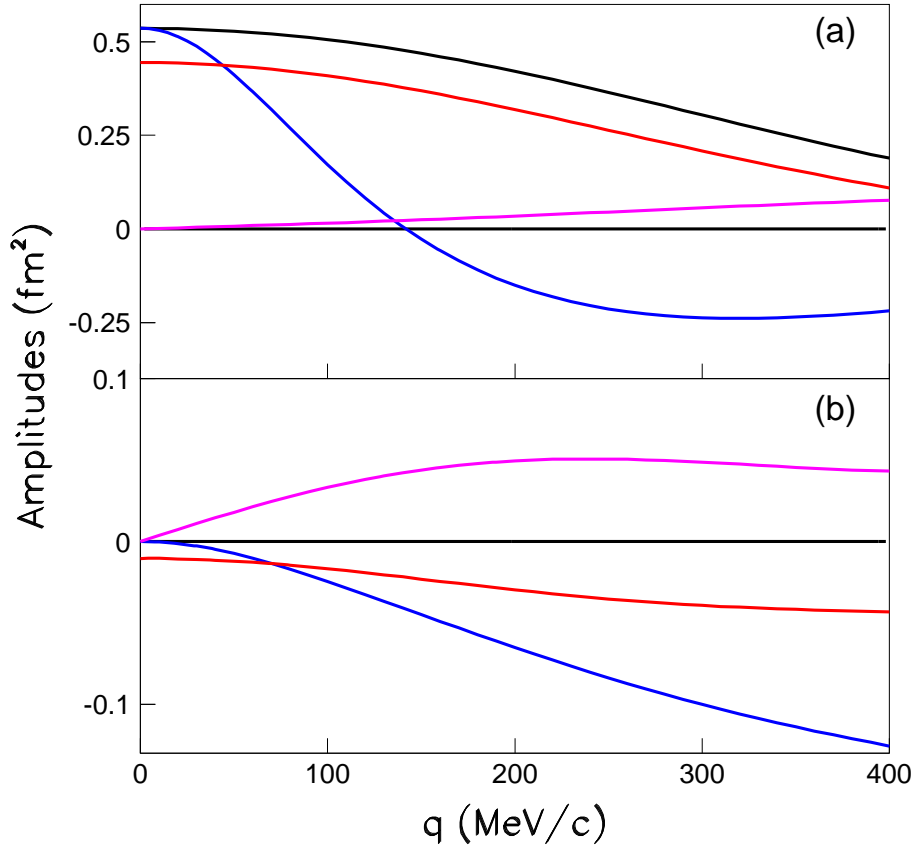
Figure 2.3: The amplitudes of the np scattering at 363 MeV. The real values are plotted in panel (a) and the imaginary ones are in panel (b). β, δ, ε and γ are indicated by black, blue, red and magenta colors respectively.

spin-spin amplitudes. As example, Fig. 2.3. shows both the real and imaginary parts of each amplitude at 363 MeV, predicted by the SAID[44] PSA solution. The general structure of the amplitudes is fairly similar at different energies. The amplitudes are normalized such that the unpolarized differential cross section of the elementary np scattering is

$$\frac{d\sigma}{dt} = |\alpha(\vec{q})|^2 + |\beta(\vec{q})|^2 + 2|\gamma(\vec{q})|^2 + |\delta(\vec{q})|^2 + |\varepsilon(\vec{q})|^2. \tag{2.3}$$

The deuteron charge-exchange reaction on proton $dp \to \{pp\}n$ can be described in terms of the elementary np amplitudes, it is therefore exploited as an effective tool to study the np scattering. Detailed theoretical studies of the deuteron charge exchange on proton in impulse approximation can be found in Ref. [52, 53]. Here we just give the essential content which are necessary for the understanding of the

approach for the np study at ANKE.

The deuteron charge exchange on proton is depicted in terms of a impulse approximation diagram in Fig. 2.4, which can be viewed as an neutron-proton elastic scattering followed by the final state interaction (FSI) between the outgoing protons. This process is most conveniently calculated in the center-of-mass reference frame of the np scattering, the so-called Breit frame is such a frame. Provided the momentum transfer is $\vec{q}$, the initial deuteron and the final proton pair have three-momentum $-\frac{1}{2}\vec{q}$ and $\frac{1}{2}\vec{q}$ respectively in the Breit frame. The momentum of the spectator proton is assumed to be zero. According to the impulse approximation, the amplitude of the deuteron charge exchange is defined by the np charge-exchange $M_{np\to pn}$ together with the initial and final wave functions, which is written as

$$M_{dp\to\{pp\}n}(\vec{k}_i, \vec{q}, \vec{k}, S, m_S, m_n, \lambda, m_p) = \left\langle \Psi_{\{pp\}}^{\vec{k},S,m_S}, \Psi_n^{m_n} \middle| M_{np\to pn}(\vec{q}) e^{i\vec{q}\cdot\vec{r}/2} \middle| \Psi_d^{\lambda}, \Psi_p^{m_p}, \vec{k}_i \right\rangle. \tag{2.4}$$

The initial state is defined by the wave functions of the deuteron (Ψ_d^{λ}) and the proton ($\Psi_p^{m_p}$), together with the initial momentum. Similarly the final state is described by the wave functions of the diproton $\{pp\}$ ($\Psi_{\{pp\}}^{\vec{k},S,m_S}$) and neutron ($\Psi_n^{m_n}$). In the $^1S_0$ limit the final state interaction (FSI) is taken into account through the diproton wave function $\Psi_{\{pp\}}^{\vec{k},S,m_S}$ which is obtained by solving the Schrödinger equation where both the strong and Coulomb potentials are included. Non-relativistic
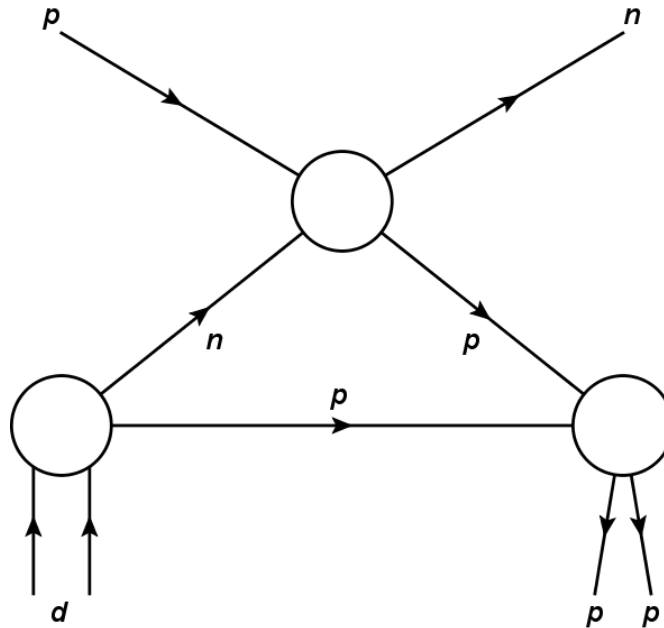
Figure 2.4: Impulse approximation diagram for the deuteron charge exchange on proton.

wave functions are adequate at low momentum transfer $\vec{q}$, whereas corrections have to be applied at higher $\vec{q}$. Here $\vec{r}$ is the relative coordinate between the neutron and proton in the deuteron, and $\vec{k}$ is the momentum of the final protons in their own center-of-mass frame, S and m_S are the total spin of the diproton $\{pp\}$ and its projection, λ is the spin projection of the deuteron, m_p and m_p are the magnetic quantum numbers of the initial proton and the final neutron. The integration of the np amplitude over the Fermi momentum can be simplified as the $M_{np \to pn}$ at certain energy, multiplied by a form factor which represents the overlap between the wave functions of the initial deuteron and the final diproton, provided that $M_{np \to pn}$ varies slowly with energy on the Fermi momentum scale.

If the final diproton emerges in the $^1S_0$ state, designated as $\{pp\}_s$, its excitation energy $E_{pp} = k^2/m_p$ is very small. In this case, the process $dp \to \{pp\}_s n$ must involves a spin flip from the deuteron state $^3S_1$ or $^3D_1$ to the state $^1S_0$ of $\{pp\}_s$ because of the Pauli blocking, therefore only the spin-dependent amplitudes contribute the cross section. The impulse approximation gives the solution for the differential cross section and the spin Cartesian observables involving the initial spins in the terms of the spin-dependent amplitudes below:

$$
\begin{aligned}
\frac{d^4\sigma}{dt\,d^3k} &= \frac{1}{3}I\{S^-(k, \frac{1}{2q})\}^2, \\
IA_y^d &= 0, \\
IA_y^p &= -2Im(\beta^\star \gamma), \\
IA_{xx} &= |\beta|^2 + |\gamma|^2 + |\varepsilon|^2 - 2|\delta|^2 R^2(k, \frac{1}{2}q), \\
IA_{yy} &= |\delta|^2 R^2(k, \frac{1}{2}q) + |\varepsilon|^2 - 2|\beta|^2 - 2|\gamma|^2, \\
IC_{y,y} &= -2Re(\varepsilon^\star \delta)R(k, \frac{1}{2}q), \\
IC_{x,x} &= -2Re(\varepsilon^\star \beta), \\
C_{yy,y} &= -2A_y^p
\end{aligned}
\tag{2.5}
$$

where

$$
R(k, \frac{1}{2}q) = S^+(k, \frac{1}{2}q)/S^-(k, \frac{1}{2}q)
\tag{2.6}
$$

is the ratio of the longitudinal form factor

$$
S^+(k, \frac{1}{2}q) = F_S(k, \frac{1}{2}q) + \sqrt{2}F_D(k, \frac{1}{2}q)
\tag{2.7}
$$

to the transverse form factor

$$S^+(k, \frac{1}{2}q) = F_S(k, \frac{1}{2}q) - 2F_D(k, \frac{1}{2}q)/\sqrt{2} \tag{2.8}$$

where

$$F_S(k, \frac{1}{2}q) = \left\langle \Psi^{\vec{k},0,0}_{\{pp\}} \middle| j_0(\frac{1}{2}qr) \middle| \Psi^S_d \right\rangle \tag{2.9}$$

and

$$F_D(k, \frac{1}{2}q) = \left\langle \Psi^{\vec{k},0,0}_{\{pp\}} \middle| j_2(\frac{1}{2}qr) \middle| \Psi^D_d \right\rangle \tag{2.10}$$

are matrix elements which are defined in terms of the deuteron wave functions $\left| \Psi^S_d \right\rangle$ and $\left| \Psi^D_d \right\rangle$ and $\{pp\}_s$ wave function $\left| \Psi^{\vec{k},0,0}_{\{pp\}} \right\rangle$. In the forward direction $R = 1$.

$$I = |\beta|^2 + |\gamma|^2 + |\varepsilon|^2 + |\delta|^2 R^2(k, \frac{1}{2}q). \tag{2.11}$$

is the spin-flip intensity. Note the formulae in Eq. 2.5 are given in the Breit frame, one should apply a Winger rotation before the comparison with the experimental results.

By scrutinizing the relationships between the np amplitudes and the observables of the deuteron charge-exchange reaction on hydrogen, one would find that the terms $|\delta|^2$, $|\varepsilon|^2$ and $|\gamma|^2 + |\beta|^2$ can be extract from the unpolarized differential cross section $\frac{d^4\sigma}{dt d^3 k}$ and the two deuteron tensor analyzing powers (A_{xx} and A_{yy}), provided that the momentum transfer $\vec{q}$ is small and the diproton emerged in the $^1S_0$ state. If not all the diprotons are in the $^1S_0$ state, contamination from the higher waves will show up. For example the signals of the observables in Eq. 2.5 will be reduced by the P-wave components, because these observables are of opposite sings for the spin-singlet and spin-triplet pp states. It is reasonable to expect that a tight cut on the excitation energy of the diproton may block the higher-wave components since the E_{pp} is small for the $^1S_0$ state. However, the pilot research at ANKE suggested that[54] components of higher waves (mainly the P wave) still remains even E_{pp} is lower than 1 MeV. Another way of minimizing the dilution from the P wave is to place a cut on the angle θ_{qk} between the momentum transfer $\vec{q}$ and the momentum $\vec{k}$ of the final protons in the center-of-mass reference frame of the diproton, since the odd partial waves can not be excited if are orthogonal to each other. In order to have sufficient statistics, data from the whole range of θ_{qk} are used and a cut of $E_{pp} < 3$ MeV is used in the subsequent measurements at ANKE. The price to be paid is that the effects of the higher waves have to be carefully taken into account in the impulse approximation.

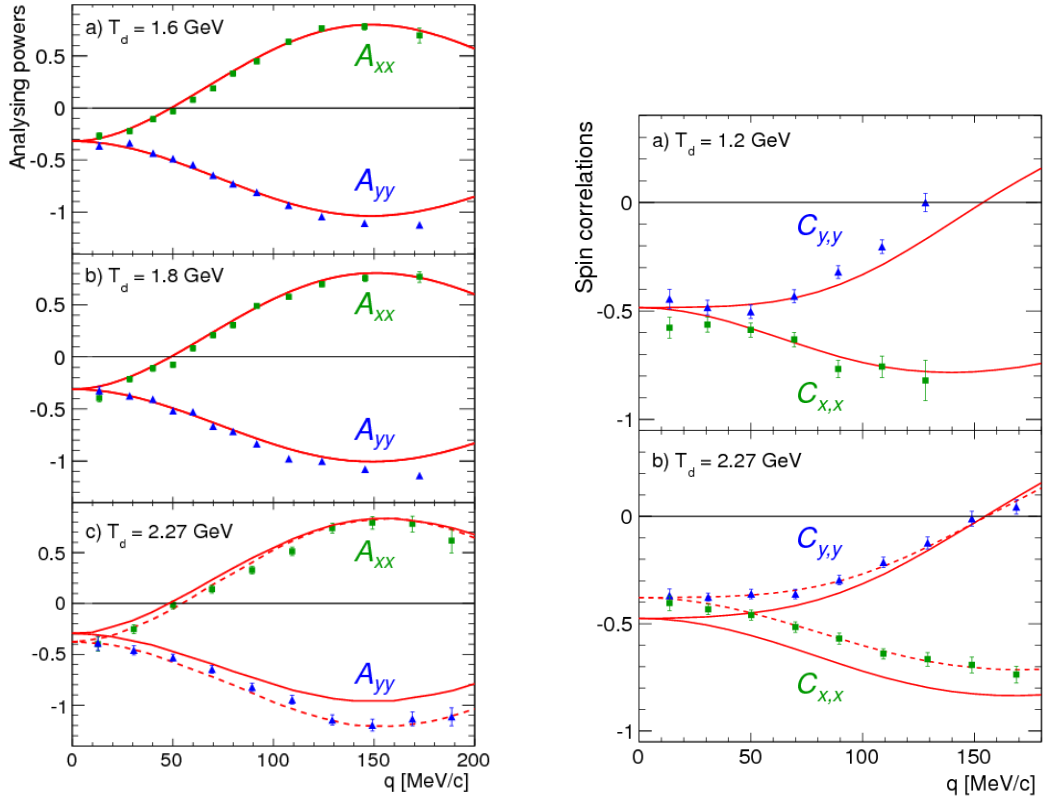## 2.2 Neutron-Proton Invetigation at ANKE in the First Phase
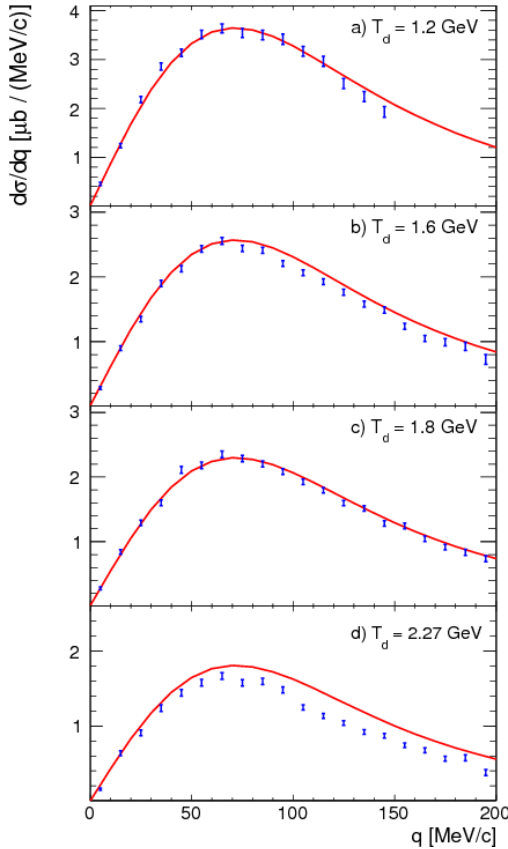
Figure 2.5: Unpolarized differential cross section of the deuteron charge-exchange reaction $d+p \rightarrow \{pp\}_s+n$ at $T_d = 1.2, 1.6, 1.8$ and 2.27 GeV with $E_{pp} < 3$ MeV. The red curves represent the impulse approximation calculations [52] using the SAID solution for the np amplitudes [44].

A systematic investigation program of the neutron-proton scattering was planed as an important topic of the spin physics at COSY many years ago[23]. Since then, great efforts have been devoted to make this research a success. Using a polarized deuteron beam of the kinetic energy $T_d = 1170$ MeV and an unpolarized hydrogen cluster target[55], an initial experiment was conducted as the proof-of-principle (POP) research. Through this research reliable polarimetry for the polarized deuteron beam was established at 1170 MeV, and the measured spin observables were well reprodeced by the impulse approximation using the well-known np amplitudes, which expressly validated the principle of the investigation. The POP experiment is described in Ref. [54, 56, 57]. Starting from 2005, production experiments were performed at 1.2, 1.6, 1.8, and 2.27 GeV, where the unpolarized differential cross section $\frac{d\sigma}{dq}$ and the one-spin observables A_{xx}, A_{yy}, A_y^p were measured. After the implementation of a polarized hydrogen target at ANKE, double polarized experiment were carried at 1.2 and 2.27 GeV in 2009, and the spin correlation coefficients $C_{x,x}$ and $C_{y,y}$ were obtained. In all these measurements[58], the energy 1.2 GeV was used mainly for the purpose of polarimetry. All the results mentioned above are presented together with the corresponding impulse approximation calculations in the following plots (refer Fig. 2.5, 2.6(a), 2.6(b) and 2.7).

From these plots, one can see that, except several values of A_{yy} and $C_{y,y}$

Figure 2.6: The tensor analyzing powers A_{xx} and A_{yy} (left) and the spin-correlation coefficients $C_{x,x}$ and $C_{y,y}$ (right) of the deuteron charge-exchange reaction $\vec{d} + \vec{p} \rightarrow \{pp\}_s + n$ at $T_d = 1.6$, 1.8 and 2.27 GeV with $E_{pp} < 3$ MeV. The red curves represent the impulse approximation calculations [52] using the SAID solution [44] for the np amplitudes. The dashed curves at 2.27 GeV corresponds an uniform reduction of the longitudinal spin-spin amplitude $\varepsilon(q)$ by about 25%.

at high momentum transfer q, the measured results coincide with the impulse approximation calculations (indicated by red lines) based on the np amplitudes taken from the SAID database well at the three lower energies $T_d = 1.2$, 1.6 and 1.8 GeV, whereas the discrepancies at the highest energy 2.27 GeV is obvious. This is not surprising, because the np amplitudes from the SAID database have far more ambiguities at energies higher than about 1 GeV. However, by reducing the longitudinal spin-spin amplitude $\varepsilon(q)$ uniformly by about 25%, the agreement between the impulse approximations and the measurements becomes fairly satisfactory, which suggests the amplitude $\varepsilon(q)$ is overestimated in the SAID database at energies higher than 1 GeV.

The investigation in the first phase of the neutron-proton scattering program at ANKE implies that the measurements of the deuteron charge exchange on proton at high energies will impact the np database significantly. However, $T_N =$
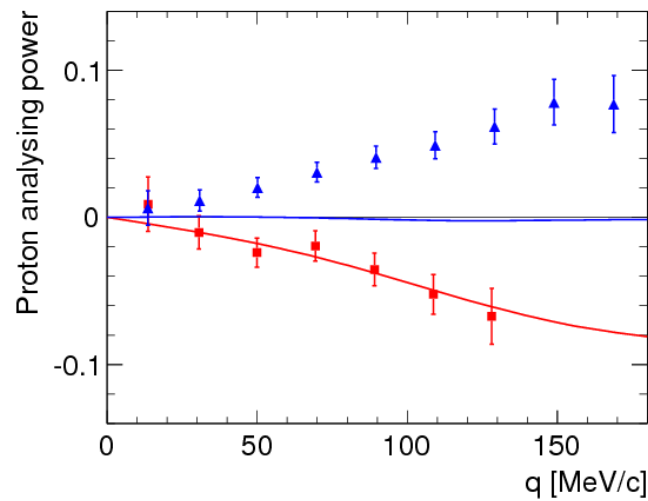
Figure 2.7: Proton analyzing power A_y^p of the deuteron charge-exchange reaction $d + \vec{p} \rightarrow \{pp\}_s + n$ at $T_d = 1.2$ and 2.27 GeV with $E_{pp} < 3$ MeV. The red curves represent the impulse approximation calculations [52] using the SAID solutio [44]n for the np amplitudes.

1.135 GeV[1] is the maximum nucleon energy accessible with the deuteron beam at COSY, to continue the investigations to the highest nucleon energy available at COSY ($T_N = 2.8$ GeV), the reverse kinematics should be adopted, where polarized deuterium targets have to be employed in conjunction with the proton beams provide by COSY.

---

[1]which corresponds to the highest deuteron energy available at COSY $T_d = 2.27$ GeV.

Chapter 3

Experimental Equipment

The experiment was performed at the ANKE magnetic spectrometer, which is located at one of the internal target stations of COSY. In this chapter, the experimental instruments that were exploited during the experiments are described.

3.1   Accelerator: COSY

The COSY (**CO**oler **SY**nchrotron) accelerator facility [59], depicted in Fig. 3.1, was designed for medium energy physics, it can deliver unpolarized as well as polarized beams of either proton or deuteron, with momenta between 0.295 GeV/c to 3.65 Gev/c. The complex mainly consists of two unpolarized ion sources and one polarized ion source [60, 61], an injector cyclotron (JULIC), an 100-meter long injection beam line, a racetrack-shaped cooler synchrotron of 184 meters in circumference, and three extraction beam lines to three external target stations.

All the three ion sources are able to produce both H^- and D^- beams. The beam from ion source is first pre-accelerated to 295 MeV/c in the isochronous cyclotron (JULIC), and then guided by the magnets along the injection line toward the carbon stripping foil, which is placed behind a dipole magnet in the extraction arc of the storage ring. By penetrating the stripping target, the negatively charged ions lose their electrons outside of the nuclei, hence resulting a proton or deuteron beam circulating in the synchrotron. Under the effects of quadruple magnetic field, the beam does betatron oscillations both vertically and horizontally while it is circulating in the storage ring thanks to the bending force of the dipole magnets, which are located in the arc sections. The radio frequency (rf) cavity is mainly used for the purpose of beam acceleration or deceleration, its radio frequencies are adjusted according to the beam revolution frequencies such that the beam gets
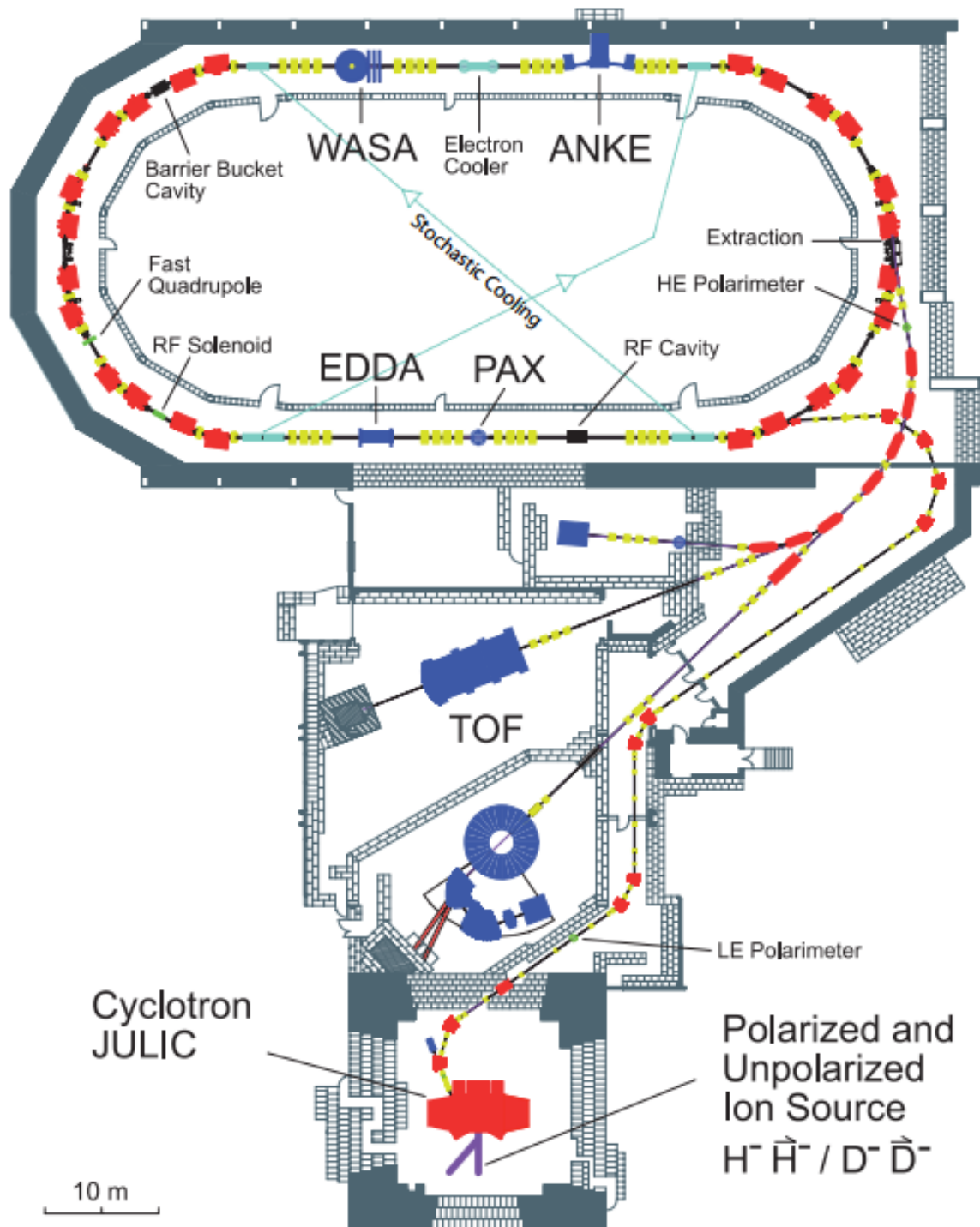
Figure 3.1: The floorplan of the COSY complex. Stripping injection is adapted at COSY in order to overcome the limitation on the beam intensity in the storage ring imposed by Liouville's theorem [60], therefore all the ion sources produce negatively charged particles(H^- or D^-). Fore internal target experiments are install at the ring. ANKE and WASA are general purpose spectrometers for hadronic and nuclear physics; PAX is dedicated instrument for polarized antiproton beam study; EDDA is currently operated as a beam polarimeter, used in the precursor investigations for the measurements of the electric dipole moment (EDM) of charged particles [63]. Among the three external target instruments, TOF is used for hadronic physics and the other two are employed in the development of the two future detectors at FAIR: PANDA and CBM.

accelerated or decelerated when it passes through the rf cavity, it is also used to reduce (or increase) beam's longitudinal phase space. In order to improve the beam quality, i.e. to compress the beam phase space, COSY has equipped and operated with an 100-keV electron cooler and a stochastic cooler [64–67] for many years. The 100-keV electron cooler is applied only at low energies, mainly at the injection energy, either to prepare low-emittance beams for the acceleration and extraction afterwards or to accumulate the intensity of the polarized beams by a cooling-stacking [67] process. The stochastic cooling, which covers the higher momentum range, is used to compensate the mean energy loss and emittance growth due to the interaction between circulating beam and target during the internal-target experiments. However the stochastic cooling will not be sufficient to counteract the even stronger heating forces that present in the experiments which require higher luminosity ($> 10^{32}$ $cm^{-2}s^{-1}$)(e.g. the WASA experiment [68] utilizing a pallet target.). The study of beam dynamics showed that electron cooling up to the maximum momentum of COSY is the only technically feasible solution. For this purpose a 2-MeV electron cooler [69] has been developed in Novosibirsk and installed at COSY in 2013. Furthermore, the 2-MeV electron cooler is intended to do some preparatory investigations for the high energy cooler of the HESR at FAIR [70, 71].

3.2 ANKE Spectrometer

ANKE (**A**pparatus for Studies of **N**ucleon and **K**aon **E**jectiles) [72] is a magnetic spectrometer located at one of the internal target stations of COSY, designed for the investigations of hadron medium physics. As shown by the top view of ANKE in Fig. 3.2, the whole detector comprises of three dipole magnets, namely D1, D2 and D3, and four sub-detection systems, whose magnetic and geometric settings can be optimized so that particles in the kinematic regions of interest can be detected, these detectors are the forward detector (Fd), the positive side detector (Pd), the negative side detector (Nd) and the silicon tracking telescope (STT). The idea of the three-dipole-magnet design is following: the COSY beam is deflected off its original straight path by an angle α by D1 magnet into the target chamber, where it collides with the target. The ejectiles from the the collisions in the forward directions are bent by the analyzing magnet D2 and registered in the detection systems Fd, Pd or Nd. The particles emitted at large scattering angles are detected by the silicon tracking telescope (STT) placed closely to the target.

The beam particles which have not interacted with the target particles are bent to the direction of the inner ring by an angle of -2α, and subsequently deflected back to the nominal orbit by D3, which bends the beam by an angle of α.
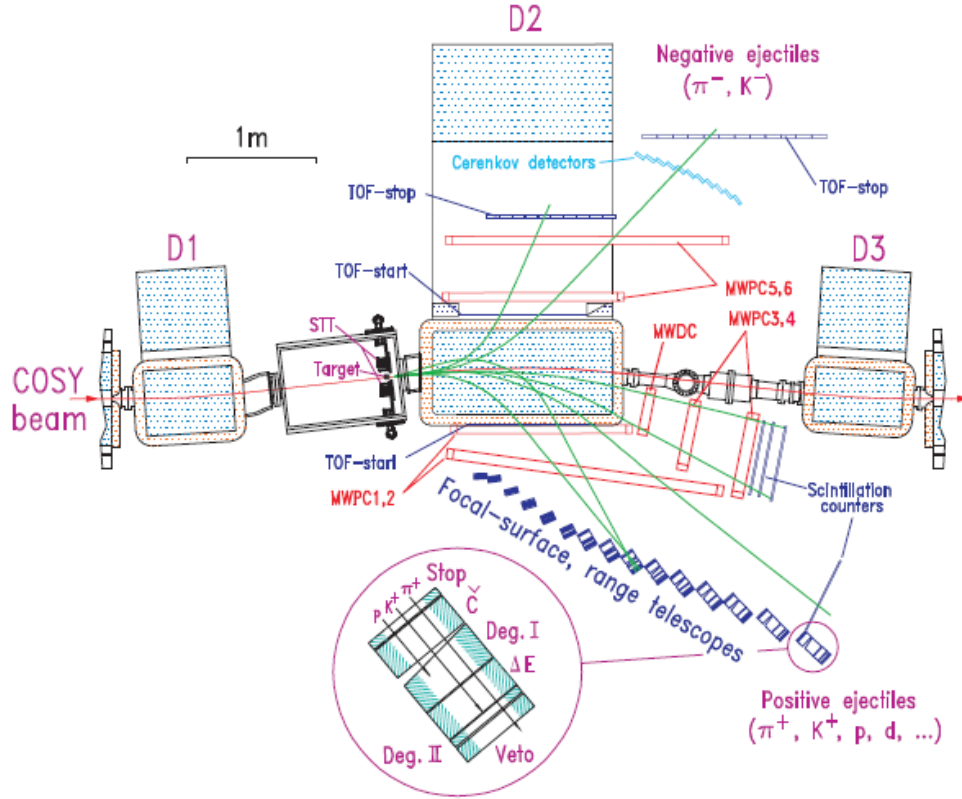
Figure 3.2: Schematic diagram of the ANKE magnetic spectrometer.

The deflection angle of the D2 magnet 2α is defined by the beam momentum and the D2 field strength, which is in turn selected for specific experiment such that the desired kinematic regions of the interested processes can be covered by the sub-detection systems. To be specific, the D2 deflection angle is calculated as

$$2\alpha = B_{D2}l_{eff}/B_\rho, \tag{3.1}$$

where B_{D2} is the field strength at the center of D2, l_{eff} is the effective field length along the COSY beam in D2, and B_ρ is the magnetic rigidity of the COSY beam. In order that different deflection angles can be realized geometrically, the spectrometer magnet D2 is installed on a pair of rail tracks, which allows D2 to move horizontally perpendicular to the COSY beam line with certain freedom. Restricted by the range within which D2 can move, α can vary from 5.5° to 10.1°. To be able to move together with the D2 magnet, the beam pipe and target chamber are connected to the D2 vacuum chamber by flexible bellows.

A vacuum chamber is installed between the gap of the D2 magnet, with three exit windows on its left, right and front sides, which allow the scattered particles to enter the sub-detection systems Nd, Pd, and Fd respectively. In order to reduce the the Coulomb scattering of the ejectile particles in the material of the exit windows, which may worsen the momentum reconstruction, the windows are made of Aluminum foils with a thickness of 0.5 mm. A ultra-vacuum target chamber is installed in front of the D2 chamber, it was designed in such a manner that different internal target can be installed for specific experiment conveniently. Up to now, a solid strip targets [72], an unpolarized cluster gas target [74–76] and a polarized internal gas target [77, 78] have been exploited in different experiments at ANKE. In Table 3.1, the features the targets mentioned above are presented.

Table 3.1: Targets available at ANKE.

Targets	Material(s)	Size	Thickness
Solid strip target	C, Cu, Ag, Au	wedge shape，length=40 mm, width=2 mm at base	$40 \ \mu g/cm^2 - 1.5 \ mg/cm^2$
Cluster-jet target	p, d	diameter 8.5 mm	$10^{14} - 10^{15} \ cm^{-2}$
Polarized cell target	$\vec{p}, \vec{d}$	transverse dimension $15 \times 20 \ mm^2$	$10^{13} \ cm^{-2}$

The sub-detection systems forward detector(Fd), positive side detector(Pd) and silicon tracking telescopes (STTs), which were employed in this experiment, are described in details in sections 3.2.1, 3.2.2 and 3.2.3.

3.2.1 Forward detector

The forward detector, placed between the dipole magnets D2 and D3, is designed to detect the high-momentum, positively charged particles produced at small scattering angles. Its major components include three multi-wire proportional chambers (MWPC) used for track reconstruction [79], a two-planed forward scintillator hodoscope (FSH) and a Cherenkov detector array [80]. Since the gap between D2 and D3 is only 1.6 meters wide, the distances between the neighboring MWPCs are subsequently very short. Given this circumstance, the spatial resolution of these MWPCs has to be sufficiently good so that precise track reconstruction could be achieved. Each MWPC is consist of two modules, used for the measurement of X and Y coordinates of the hits respectively. We shall call them X(Y) module here for brevity. The X(Y) module comprising of a wire plane with wires arranged in the direction of (Y)X axis at distances of 1 mm, and a strip plane which is inclined by $-(+)180°$ with respect to the wires.
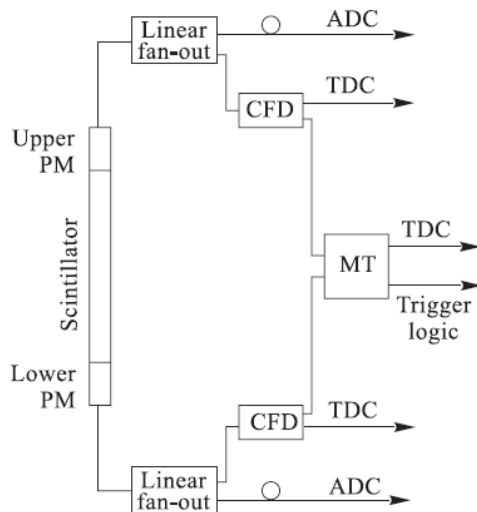
The forward scintillation hodoscope (FSH) behind the multi-wire proportional chambers (MWPC) is mainly used to record the time and energy signals for particle
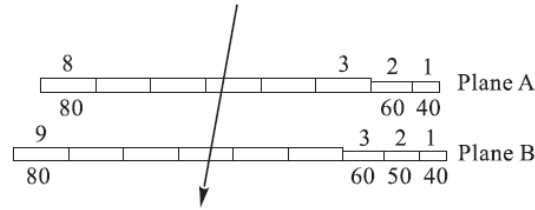
Figure 3.3: Top view of the Fd counters

identification and track reconstruction. As depicted in its top view in Fig. 3.3, it comprises of two planes with 8 and 9 vertically arranged plastic scintillation counters of length of 360 mm, respectively. In each plane, the six counters which are far from the beam pipe have a cross section of 80×20 mm^2, whereas the others have a thickness of 15 mm and their widths decrease (see Fig. 3.3). For the purpose of the time calibration between different counters (refer 4.2.2.1), the plane A is half-width shifted towards the beam pipe with respect to plane B. All the counter are read out at both ends via lucite light guides and photo multipliers. Fig. 3.4 illustrates the frond end electronics of each counter. Signal from each photo multiplier is converted into one analog signal (ADC) and two logical signals (TDC) by the linear fan-out and the constant fraction discriminator (CFD)[1]. The upper and lower TDCs are exploited to obtain the hit position as well as to form the mean time and the trigger. The ADC signals, on the other hand, are mainly used to extract the particle energy deposit.

Figure 3.4: Front end electronics.
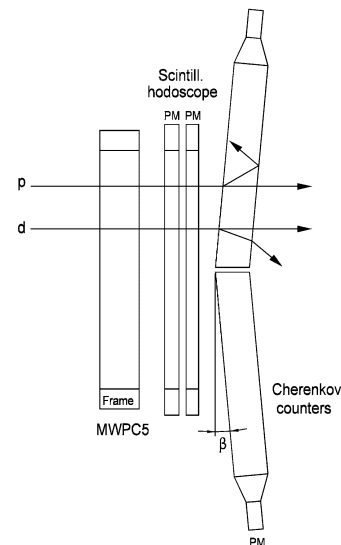
Figure 3.5: Cherenkov counter.

---

[1]The CFD is used for eliminating the time walk caused by the difference between the signal amplitudes.

The 16 Cherenkov counters behind the forward scintillator telescope (FSH) are used to discriminate fast particles with the same momentum, taking advantage of the fact that the emission angle of the Cherenkov light is dependent on the velocity of the incident particles [81]. As illustrated in Fig. 3.5, via inclining the Cherenkov detectors by an appropriate angle β, the light originated from the slower particle, say deuteron, will have a small opening angle thus is absorbed due to refraction and long light path; on the other hand, the light from the faster particle, say proton, will have a large enough opening angle which allows it propagate to the photomultipliers and produce a signal. From the above discussion, we see that the inclining angle β is a critical parameter, one needs to optimize it according to specific requirements of the experiments so that the best particle discrimination can be achieved.

Besides the three MWPCs and the FSH described in the preceding paragraphs, there is a set of detectors (Side Wall) comprising of two vertically placed planes of 5 and 6 scintillators with dimensions of $height \times width \times thickness = 1000 \times 100 \times 10 \ mm^3$ respectively, and an array of Cherenkov counters. The side wall, unlike the FSH which is implemented in the common frame with the MWPCs, is independent on the other detectors, is independent of the other detectors. Thus it can be placed either at the lower-momentum end of FSH to increase the acceptance, or behind the FSH as a veto detector.

3.2.2 Positive side detector

The positive side detection system is used to register the positively-charged particles ejected in the forward directions with lower momenta. It is implemented on the right-hand side of the D2 magnet. The main components of this detector include the particle tracking system comprising of two multi-wire proportional chambers (MWPCs), and the system for particle identification, which consists of 23 TOF-start counters mounted close to the right exit window of the D2 vacuum chamber and 15 segmented range telescopes placed in the focal plane of D2.

The MWPC installed next to the start counters has a sensitive area of $350 \times 1300 \ mm^2$, while that of the other MWPC is $600 \times 1960 \ mm^2$, both adapted to the geometrical acceptance which they are supposed to cover. Each MWPC has three layers of tangsten wires at a distance of 2.54 mm with different orientations (vertical, $+30°$, $-30°$). The diameter of the wire is 20 μm and 25 μm for the smaller and the larger MWPC respectively. Mylar foils with a thickness of 20 μm, coated with C or Al arer served as the cathodes. The distance between the anode

wire and the cathode plane is 5 mm. During the experiments, these MWPCs are operated with mixture of 70% of Argon and 30% of CO_2.

The particle identification is based of time of flight (TOF), energy loss (ΔE) and information from the range telescope. The time of flight is measured between the TOF-start counters and the TOF-stop counters. In order to have long time of flight, the start counters are installed extremely close to the D2 exit window, actually the frame of the start counters is fixed on D2 magnet. On one hand the thinner a scintillator is, the less photons it produced when charged particles passing through it; but on the other hand the multiple scattering in the scintillator worsens the track reconstruction, therefore the thickness of the scintillator counters in the TOF-start plane is the result of a compromise between the requirements of sufficient light output and small angular spread. As a result of the preceding consideration, counter 1 and 2 at the low momentum end have a thickness of 0.5 mm, while it is 1.0 mm for counters 3 to 5, and 2.0 mm for the rest. The width and the height for all the scintillators in the start plane are the same (50 mm and 270 mm respectively, slightly larger than the dimension of D2 exit window).

The range telescopes are designed for particle identification, especially used to discriminate the K^+ mesons from massive background of protons and pions [82]. One of the range telescopes is depicted in the exaggerated way in Fig. 3.2. A range telescope is composed of a TOF-stop counter, a Cherenkov scintillator, two degraders , a ΔE detector and a veto detector. The principle of the particle identification with the telescope is illustrated in Fig. 3.2: the kaons are stopped either in the ΔE detector or in the second degrader, whereas the proton lose their kinetic energy before passing through the first degrader, and the pions can penetrate the second degrader thus be detected by the veto detector. Of course the decay products such as pions and muons could also produce signals in the veto detector, but these particles can be distinguished from the primary pions utilizing the characteristic decay time (12 ns). In additional, the Cherenkov scintillators installed in the telescopes placed on the high-momentum side can register the photons caused by the fast pions. The reason that the first degrader is wedge-shaped leis in the fact that particles fall into one telescope have a certain of momentum spread. This momentum spread for the experiment with point-like target is about 10%, which is acceptable, whereas in experiment with a long target the momentum spread is so large that the method for PID described above is no longer valid. Therefore only the stop counter are used for this experiment.

3.2.3 Silicon Tracking Telescopes

In the second phase of the ANKE np investigation [23], where the polarized deuteron target is used to provide the quasi-free neutron, one needs to detect the slow spectator protons which are emitted isotropically around the target. Besides the use of a long storage-cell target (refer sec. 3.3.2) makes the vertex measurement necessary. Therefore a detection system which can identify and track the low-energy particles at large angles are indispensable. The silicon tracking telescope (STT) [73] was developed for this purpose. As shown in Fig. 3.6, one STT is consist of three double-sided microstructed silicon strip detectors and the auxiliary components such as the read-out electronics and the cooling system. The combination of the three silicon strip detectors forms a telescope system, which permits both particle identification (PID) and tracking (refer sec. 4.2.1.1). The PID is based on the $\Delta E/E$ method, this means (the four-momentum of) a particle can be measured by STT only if this particle penetrates the most inner layer and is stopped by STT. Therefore the energy range covered by a STT is determined by the thickness of the inner layer and the total thickness. Thus one STT with the thinnest possible inner layer and the thickest possible outer layer is desired.
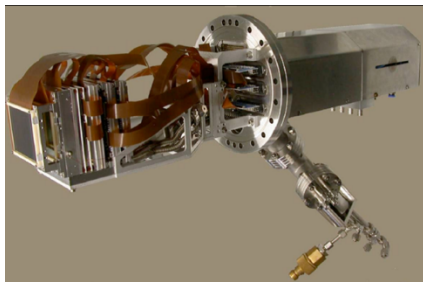
Figure 3.6: Silicon tracking telescope.
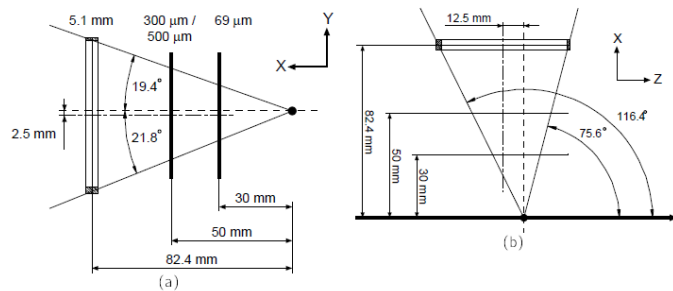
Figure 3.7: Top and side views of STT.

Based on above consideration, together with other constrains such as the space limits set by the target chamber and the available technology for making the silicon detectors, the STT has been designed with the configuration indicated in Fig. 3.7. To have a large geometrical acceptance, a short distance between telescope and target is desired, the telescopes are installed close to the target with a distance of only 27.970 mm, corresponding to an azimuthal angle coverage of $\pm20°$ or so. The modularity of the STT enables one to cover the interested angle ranges for specific experiment by optimizing the position of the telescope along the beam direction. In addition, a configuration of 4 STTs with 2 STTs placed

on each side of the target permits to have a large acceptance. The effective pitch width of the inner and middle silicon detectors is about 400 μm while it is about 600 μm for the detector outside. Accordingly the angular resolution of the track is $1° - 6°$ (FWHM), depending on particle type, energy loss and the track inclination. Such angular resolution permits a vertex reconstruction with a resolution of about 1 mm. Defined by the thickness of the detectors depicted in Fig. 3.7, the energy ranges of 2.5-32 MeV for proton and 4-43 MeV for deuteron are achieved with a resolution of 150-250 MeV. The STT is able to recognize a particle passage within 100 ns, which can be used to trigger the read out. This self-triggering feature makes it possible to configure high-level triggers in combination with the other ANKE triggers.

3.3 Polarized Internal Target

The polarized internal target [83, 84] is one of the targets adopted at the ANKE spectrometer, which allows to conduct not only single polarized experiments but also double polarized experiments at ANKE in conjunction with COSY beam. This installation is able to provide both polarized hydrogen target and polarized deuterium target, each with different polarization modes. Fig. 3.8 is a photo of the ANKE polarized internal target, as illustrated on this photo, the main components of the polarized internal target include an atomic beam source(ABS) [85], a storage cell [86] and a lamb-shift polarimetry [87, 88]. The atomic beam source provide jet of atoms of hydrogen or deuterium with nuclear spin polarization. However the areal density of ABS jet is generally too small to meet any practical needs, in order to overcome this problem a device named "storage cell" has been developed and used widely in the spin physics community since long time ago. Inside the ANKE target chamber a storage cell is installed in order to increase the target thickness when the polarized internal target is adapted for research. The Lamb-shift polarimetry, shown in the bottom of Fig. 3.8 can measure the polarization of ABS jet very fast (within several seconds) with a precision of 1%, it is used to adjust the configuration of the atomic beam source at the beginning of experiments. Section 3.3.1 is devoted to general working principle and major functional parts of the atomic beam source. Different aspects of of the storage cell is discussed in section 3.3.2. Finally the lamb-shift polarimetry is described in section 3.3.3.
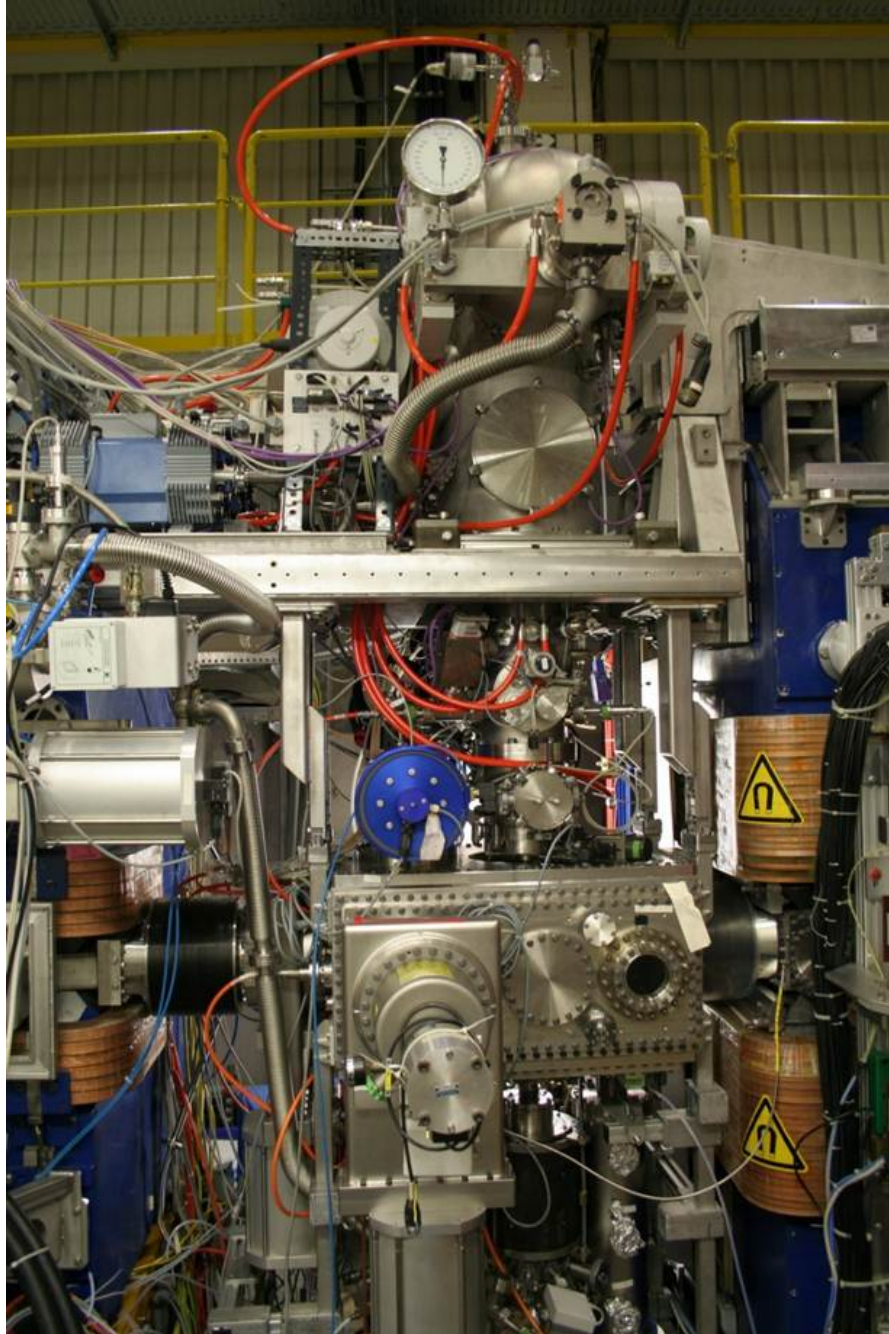
Figure 3.8: The Polarized internal target at ANE.

3.3.1 Atomic Beam Source

It is necessary to understand how physically the ABS produces nuclear-polarized beams out of the unpolarized ensembles before one goes into the technical details, therefore the basic physics behind the principle of ABS is discussed first in Section 3.3.1.1. However, only knowing the basic principle is not enough if one wishes to realize or use this sophisticated instrument, so a detailed description of the main functional components is provided in the following section.

3.3.1.1 Working principle of ABS

The Stern-Gerlach experiment [89], which lead to the discovery of spin, showed for the first time that a beam of atoms could be spatially separated in an inhomogeneous magnetic field. This experiment is showed in Fig. 3.9, in the inhomogeneous magnetic field $\vec{B}(z)$, the potential energy of the Ag atom with magnetic moment $\vec{\mu}$ is $U = \vec{B}(z) \cdot \vec{\mu}$, which is not uniform, thus the magnetic field exerts a force on the atom: $F = -\nabla U = -\nabla(\vec{B}(z) \cdot \vec{\mu}) = -\frac{\partial B}{\partial Z} g_s \mu_B S_z$. In this manner, the Ag atoms with their electron spins oriented upwards ($S_z = \frac{1}{2}\hbar$) and downwards ($S_z = -\frac{1}{2}\hbar$) are separated while they are passing through the magnetic field, as a result both the separated beams are polarized with respect the electron spin.
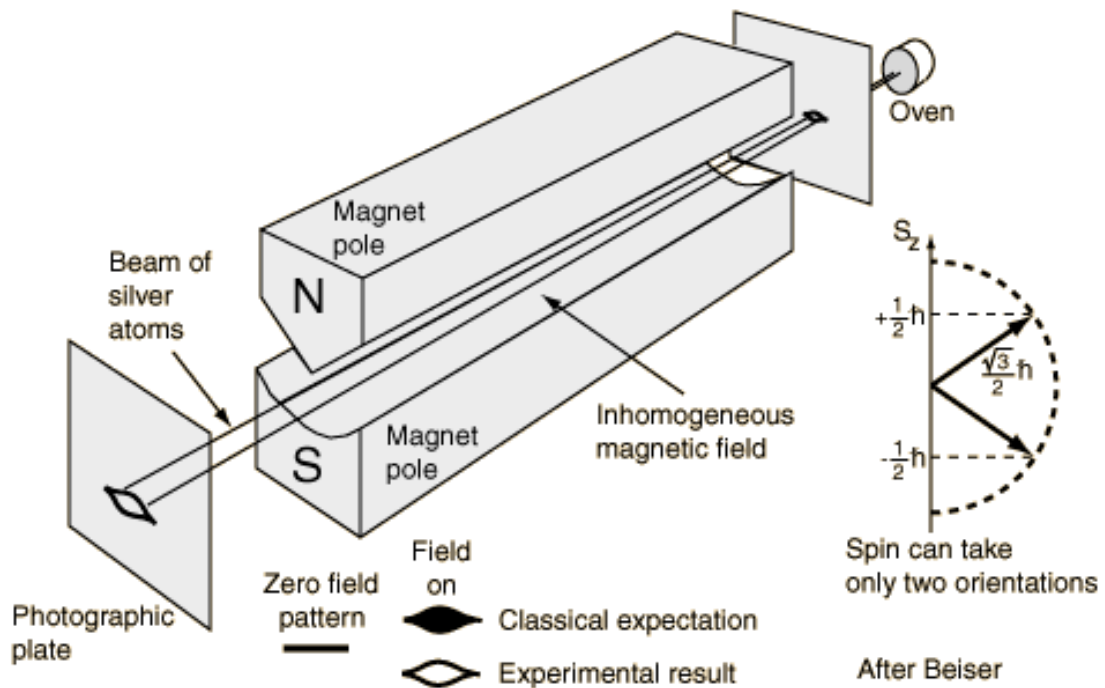
Figure 3.9: Stern-Gerlach principle

The general idea of the polarized atomic beam source (ABS) is basically from the Stern-Gerlach experiment. Note that the beam profile of the separated beams in the Stern-Gerlach experiment is not cylindrically symmetric, which is essential for better beam qualities (such as beam intensity and polarization etc), thus the dipole field is substituted with a cylindrically symmetric multiple filed (either sextuple or quadruple) in ABS. One should also note that the beam from the spin separator (i.e. the inhomogeneous magnetic field) is only electronicly polarized, due to the smallness of the proton/deuteron magnetic moment associated with the nuclear spin, it is practically impossible to polarize the nuclear spin according

to the energy difference between their spin sub-states in the magnetic field, as in the Stern-Gerlach experiment. An additional device, i.e. the fast adiabatic passage [94] is employed as a spin flipper to manipulate the nuclear spin, making use of the fact that the nuclear spin is associated with the electron spin.

The object we deal with is hydrogen/deuterium atoms in the magnetic field, where the nuclear spin and the electron spin interact with each other and the Zeeman effect [91] plays an important role as well. As the atoms are separated according to the energy of the sub-states with different spin configurations, it is necessary and sufficient to study the relation between their spin states and energy eigne states. The atoms in the atomic beam source are mostly in their ground states, where the angular momentum of the valence electron is $\vec{J} = \vec{S}$. Henceforward we denote the nuclear spin by $\vec{I}$ and $\vec{F} = \vec{S} + \vec{I}$ as its sum with the electron angular momentum $\vec{S}$, and the letters with subscript m represent the projections along the magnetic field B of the corresponding vectors. The Hamiltonian operator relevant to the energy differences reads

$$\hat{H} = -\gamma_e \hat{S}_m B - \gamma_n \hat{I}_m B + a_{hfi}(\hat{\vec{S}} \cdot \hat{\vec{I}}) \tag{3.2}$$

where the first and second terms describe the interaction between the spins and the external magnetic field $\vec{B}$ while the third term describes the hyperfine interaction between the electron spin and the nuclear spin. Here $\gamma_e = -g_e \mu_B/\hbar = -g_e \frac{e}{2m_e}$ and $\gamma_n = g_n \mu_N/\hbar = g_n \frac{e}{2m_p}$ are the gyromagnetic ratios of electron and nucleus respectively, and a_{hfi} is the hyperfine constant.

Now we shall digress a bit to discuss the hyperfine coupling in the absence of external field first , because as it will be seen soon that it is convenient to use the hyperfine split as the basic unit in the discussion of the hyperfine interaction in the magnetic field. Without external field the Hamiltonian operator defined in Eq. 3.2 reduces to $\hat{H}_{hfi} = a_{hfi}(\hat{\vec{S}} \cdot \hat{\vec{I}})$, it is straightforward that the solution of its Hamiltonian equation $\hat{H}_{hfi} |F\rangle = E_F |F\rangle$, i.e. the hyperfine interaction energy is $E_F = a_{hfi}(\hat{\vec{S}} \cdot \hat{\vec{I}})$. Using the relation $\vec{I} \cdot \vec{S} = \frac{1}{2}[F(F+1) - I(I+1) - S(S+1)]$, it can be calculated that

$$E_F = \frac{a\hbar^2}{2}[F(F+1) - I(I+1) - \frac{3}{4}] \tag{3.3}$$

and the hyperfine split is

$$\Delta E = E_{F=I+\frac{1}{2}} - E_{F=I-\frac{1}{2}} = a\hbar^2(I + \frac{1}{2}) \tag{3.4}$$

Another frequently used unit is the magnetic field which corresponds the hyperfine split: $B_{crit} = \Delta E/(g_e - g_n)\hbar$, with this unit any magnetic field B can be expressed as a dimensionless quantity $x = B/B_{crit}$.

Let us come back to study the atoms in external magnetic field. Because our purpose is to study the behaviour and properties of variant spin sub-states in the magnetic field, it is nature to study it in the representative space of the spin: $|S, m_S\rangle \otimes |I, m_I\rangle \equiv |m_S, m_I\rangle$, where $|S, m_S\rangle$ is the eigenvector of S^2 and S_z and $|I, m_I\rangle$ is the eigenvector of I^2 and I_z. Further simplification $|m_S, m_I\rangle \equiv |m_S, m_F - m_S\rangle$ can be made taking the angular moment conservation $m_F = m_S + m_I$ into account. In the Hilbert space spanned by the base vectors $|\uparrow\rangle = \left|\frac{1}{2}, m_F - \frac{1}{2}\right\rangle$ and $|\downarrow\rangle = \left|-\frac{1}{2}, m_F + \frac{1}{2}\right\rangle$, the Hamiltonian $\hat{H}$ defined in Eq. 3.2 is expressed as

$$\hat{H} = \begin{pmatrix} H_{\uparrow\uparrow} & H_{\uparrow\downarrow} \\ H_{\downarrow\uparrow} & H_{\downarrow\downarrow} \end{pmatrix} \tag{3.5}$$

Rewriting the inner product in the third term of Eq. 3.2 in the form of the ladder operators $\hat{S}_\pm = \hat{S}_x \pm \hat{S}_y$ and $\hat{I}_\pm = \hat{I}_x \pm \hat{I}_y$ as

$$\hat{\vec{S}} \cdot \hat{\vec{I}} = \hat{S}_z \hat{I}_z + \frac{1}{2}(\hat{S}_+ \hat{I}_- + \hat{S}_- \hat{I}_+) \tag{3.6}$$

The properties of the ladder operators, the orthogonality of the the base vector and the angular momentum conservation $\Delta_{m_S} + \Delta_{m_I} = 0$ lead to the following relations:

$$\left\langle m'_S, m'_I \left| \hat{S}_+ \hat{I}_- \right| m_S, m_I \right\rangle$$
$$= \sqrt{(S + m_s + 1)(S - m_S)(I - m_I + 1)(I + m_I)}\delta_{m'_S - (m_s+1)}\delta_{m'_I - (m_I-1)}\delta_{\Delta_{m_S} + \Delta_{m_I}} \tag{3.7a}$$

and

$$\left\langle m'_S, m'_I \left| \hat{S}_- \hat{I}_+ \right| m_S, m_I \right\rangle$$
$$= \sqrt{(S - m_s + 1)(S + m_S)(I + m_I + 1)(I - m_I)}\delta_{m'_S - (m_S-1)}\delta_{m'_I - (m_I+1)}\delta_{\Delta_{m_S} + \Delta_{m_I}} \tag{3.7b}$$

Utilizing the relations above the matrix elements in Eq. 3.5 are computed as following:

$$H_{\uparrow\uparrow} = \left\langle \frac{1}{2}, m_F - \frac{1}{2} \left| \hat{H} \right| \frac{1}{2}, m_F - \frac{1}{2} \right\rangle$$
$$= -B\hbar[\frac{1}{2}\gamma_e + \gamma_n(m_F - \frac{1}{2})] + \frac{1}{2}(m_F - \frac{1}{2})a\hbar^2 \tag{3.8a}$$

$$H_{\downarrow\downarrow} = \left\langle -\frac{1}{2}, m_F + \frac{1}{2} \left| \hat{H} \right| -\frac{1}{2}, m_F + \frac{1}{2} \right\rangle$$
$$= -B\hbar[-\frac{1}{2}\gamma_e + \gamma_n(m_F + \frac{1}{2})] - \frac{1}{2}(m_F + \frac{1}{2})a\hbar^2 \tag{3.8b}$$

$$H_{\uparrow\downarrow} = H_{\downarrow\uparrow} = \left\langle -\frac{1}{2}, m_F + \frac{1}{2} \left| \hat{H} \right| \frac{1}{2}, m_F - \frac{1}{2} \right\rangle$$
$$= \frac{1}{2}a\hbar^2\sqrt{(I + \frac{1}{2})^2 - m_F^2} \tag{3.8c}$$

Put those matrix elements back into the Hamiltonian 3.5 and solve the Schrodinger's equation $\hat{H}|i\rangle = E_i|i\rangle$, the eigenvalues of the energy are obtained as the Breit-Rabi formula [92]:

$$E_i(F = I \pm \frac{1}{2}, m_F, x) = -\frac{\Delta E}{2}\left[\frac{1}{2I+1} - \frac{\gamma_n B m_F}{\Delta E/2} \pm \sqrt{1 + \frac{4m_F}{2I+1}x + x^2}\right]$$
$$\approx -\frac{\Delta E}{2}\left[\frac{1}{2I+1} \pm \sqrt{1 + \frac{4m_F}{2I+1}x + x^2}\right] \tag{3.9}$$

The term $-\frac{\gamma_n B m_F}{\Delta E/2}$ is neglected here because the nuclear gyromagnetic ratio γ_n is so small that in practice it hardly contributes. For a given total spin F, its projection along the external field m_F can take $-F, -F+1, ..., F$, thus there are four energy eigen states for Hydrogen atom and six energy eigen states for Deuterium atom. These eigen states (i.p. there eigen values and wave functions) are functions of the external magnetic field x.

We shall now search for the wave function $|E_i\rangle$ for each energy eigen state E_i. In the spin space $|m_S, m_F - m_S\rangle$ 中 $|E_i\rangle$, $|E_i\rangle$ is expressed as a linear combination of the base vectors $|\uparrow\rangle = \left|\frac{1}{2}, m_F - \frac{1}{2}\right\rangle$ and $|\downarrow\rangle = \left|-\frac{1}{2}, m_F + \frac{1}{2}\right\rangle$, i.e.

$$|E_i\rangle = c_i^\uparrow \left|\frac{1}{2}, m_F - \frac{1}{2}\right\rangle + c_i^\downarrow \left|-\frac{1}{2}, m_F + \frac{1}{2}\right\rangle \tag{3.10}$$
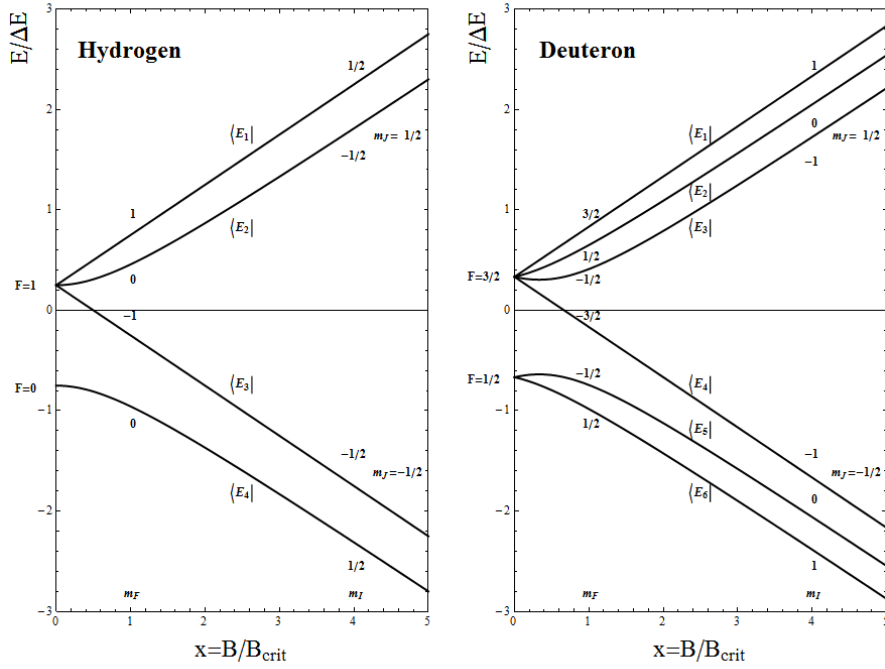
Figure 3.10: Breit-rabit diagram for Hydrogen and Deuterium atom

The coefficients $c_i^\uparrow$ and $c_i^\downarrow$ can be worked out analytically by solving the Hamiltonian function

$$\begin{pmatrix} H_{\uparrow\uparrow} & H_{\uparrow\downarrow} \\ H_{\downarrow\uparrow} & H_{\downarrow\downarrow} \end{pmatrix} \begin{pmatrix} c_i^\uparrow \\ c_i^\downarrow \end{pmatrix} = E_i \begin{pmatrix} c_i^\uparrow \\ c_i^\downarrow \end{pmatrix} \tag{3.11}$$

together with the equation

$$c_i^{\uparrow 2} + c_i^{\downarrow 2} = 1 \tag{3.12}$$

which ensures the normalization condition. At this point the procedure of how to work out the Zeeman sates of the Hydrogen/Deuterium atoms in the spin space is clear. As a summary and for the convenience in the discussion of the polarizations, the eigen energies as well as the corresponding wave functions of both the hydrogen and deuterium atoms in external magnetic field are given below.

For hydrogen the eigen energies are

$$E_1 = \frac{\Delta E}{2} \left[-\frac{1}{2} + (1+x) \right] \tag{3.13a}$$

$$E_2 = \frac{\Delta E}{2} \left[-\frac{1}{2} + \sqrt{1+x^2} \right] \tag{3.13b}$$

$$E_3 = \frac{\Delta E}{2}\left[-\frac{1}{2} + (1-x) \right] \tag{3.13c}$$

$$E_4 = \frac{\Delta E}{2}\left[-\frac{1}{2} - \sqrt{1+x^2} \right] \tag{3.13d}$$

with the hyperfine split $\Delta E = 1420$ MHz for Hydrogen atom at the ground state $1S_{\frac{1}{2}}$. These eigen energies are plotted in the left panel of Fig. 3.10 as functions of external field x. The corresponding wave functions are

$$|E_1\rangle = \left| \frac{1}{2}, \frac{1}{2} \right\rangle \tag{3.14a}$$

$$|E_2\rangle = \frac{1}{\sqrt{2}}\left(\sqrt{1+k}\left| \frac{1}{2}, -\frac{1}{2} \right\rangle + \sqrt{1-k}\left| -\frac{1}{2}, \frac{1}{2} \right\rangle \right) \tag{3.14b}$$

$$|E_3\rangle = \left| -\frac{1}{2}, -\frac{1}{2} \right\rangle \tag{3.14c}$$

$$|E_4\rangle = \frac{1}{\sqrt{2}}\left(\sqrt{1-k}\left| \frac{1}{2}, -\frac{1}{2} \right\rangle + \sqrt{1+k}\left| -\frac{1}{2}, \frac{1}{2} \right\rangle \right) \tag{3.14d}$$

where $k = \frac{x}{\sqrt{1+x^2}}$. The Zeeman states $|E_1\rangle$ and $|E_3\rangle$ are pure states in the spin space whose wave functions are irrelevant to the external magnetic field. On the other hand, the other two states $|E_2\rangle$ and $|E_4\rangle$ are superpositions of spin eigenstates, and the superposition coefficients depend on the external magnetic field, as a results the polarizations (both electronic and nuclear) are functions of magnetic field x. Fig. 3.11 shows how the nuclear polarization $P_z(x) = \frac{N_\uparrow - N_\downarrow}{N_\uparrow + N_\downarrow}$[2] vary with the magnetic field for all the hydrogen Zeeman states, as can be seen from this plot the polarizations of the pure states are always the maximum value ($+1$ and -1 respectively). In the case of superposition states, the nuclear spin is unpolarized without the presence of external magnetic field, and the polarizations increase with magnetic field x until the maximum polarizations are achieved in strong field ($x > 10$). The polarizations are calculated as the weighted average

---

[2]$N_\uparrow$ and $N_\downarrow$ are the occupation fraction (multiplied by a common constant if the wave functions are not normalized.) of atoms with nuclear spin parallel and atiparalle to the quantization axis, which are calculated as the squares of the superposition coefficients $c_i^\downarrow$ and $c_i^\uparrow$.

of the occupied components if the target ensemble is composed of several Zeeman states.
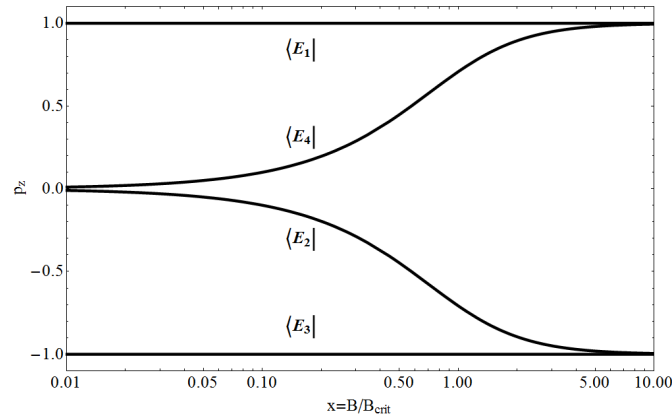
Figure 3.11: Vector polarizations of Hydrogen Zeeman components as functions of x.

Similarly, there are six Zeeman states for deuterium, their eigen energies are

$$E_1 = \frac{\Delta E}{2} \left[-\frac{1}{3} + (1 + x) \right] \tag{3.15a}$$

$$E_2 = \frac{\Delta E}{2} \left[-\frac{1}{3} + \sqrt{1 + \frac{2}{3}x + x^2} \right] \tag{3.15b}$$

$$E_3 = \frac{\Delta E}{2} \left[-\frac{1}{3} + \sqrt{1 - \frac{2}{3}x + x^2} \right] \tag{3.15c}$$

$$E_4 = \frac{\Delta E}{2} \left[-\frac{1}{3} + (1 - x) \right] \tag{3.15d}$$

$$E_5 = \frac{\Delta E}{2} \left[-\frac{1}{3} - \sqrt{1 - \frac{2}{3}x + x^2} \right] \tag{3.15e}$$

$$E_6 = \frac{\Delta E}{2} \left[-\frac{1}{3} - \sqrt{1 + \frac{2}{3}x + x^2} \right] \tag{3.15f}$$

with the hyperfine split $\Delta E = 327$ MHz for deuterium atom at the ground state $1S_{\frac{1}{2}}$. These eigen energies are plotted in the right panel of Fig. 3.10 as functions of magnetic field x. The corresponding wave functions are

$$|E_1\rangle = \left|\frac{1}{2}, 1\right\rangle \tag{3.16a}$$

$$|E_2\rangle = \frac{1}{\sqrt{2}}\left(\sqrt{1+m}\left|\frac{1}{2}, 0\right\rangle + \sqrt{1-m}\left|-\frac{1}{2}, 1\right\rangle\right) \tag{3.16b}$$

$$|E_3\rangle = \frac{1}{\sqrt{2}}\left(\sqrt{1+n}\left|\frac{1}{2}, -1\right\rangle + \sqrt{1-n}\left|-\frac{1}{2}, 0\right\rangle\right) \tag{3.16c}$$

$$|E_4\rangle = \left|-\frac{1}{2}, -1\right\rangle \tag{3.16d}$$

$$|E_5\rangle = \frac{1}{\sqrt{2}}\left(\sqrt{1-n}\left|\frac{1}{2}, -1\right\rangle - \sqrt{1+n}\left|-\frac{1}{2}, 0\right\rangle\right) \tag{3.16e}$$

$$|E_6\rangle = \frac{1}{\sqrt{2}}\left(\sqrt{1+m}\left|-\frac{1}{2}, 1\right\rangle - \sqrt{1-m}\left|\frac{1}{2}, 0\right\rangle\right) \tag{3.16f}$$

where $m = \frac{x+\frac{1}{3}}{\sqrt{1+\frac{2}{3}x+x^2}}$ and $n = \frac{x-\frac{1}{3}}{\sqrt{1-\frac{2}{3}x+x^2}}$. Like the case of Hydrogen, the two states with the maximum and minimum projections of total spin along the magnetic field, i.e. state $|E_1\rangle (m_F = \frac{3}{2})$ and state $|E_3\rangle (m_F = -\frac{3}{2})$ are pure states, while the others are superposition states. In Fig. 3.12, the left plot shows the dependence of the vector polarization $P_z = \frac{N_\uparrow - N_\downarrow}{N_\uparrow + N_\downarrow}$ on the external magnetic field for each deuterium Zeeman state, and the right plot is for the tensor polarization $P_{zz} = \frac{N_\uparrow + N_\downarrow - 2N_0}{N_\uparrow + N_\downarrow + N_0}$. As usual $N_\uparrow$, $N_\downarrow$ and N_0 denote the occupation number of deuterium atoms with $m_I = \frac{1}{2}$, $m_I = -\frac{1}{2}$ and $m_I = 0$ respectively. The corresponding superposition coefficients are squared to get these occupation numbers. Refer to the Breit-Rabi diagram Fig. 3.10, one would find that the Stern-Gerlach type separator (multiple magnets) can only separate an unpolarized ensemble into two groups: the Zeeman components with $m_S = \frac{1}{2}$ in strong magnetic field and others with $m_S = -\frac{1}{2}$.

(a) Vector polarization P_z of Deuterium.

(b) Tensor polarization P_{zz} of Deuterium.
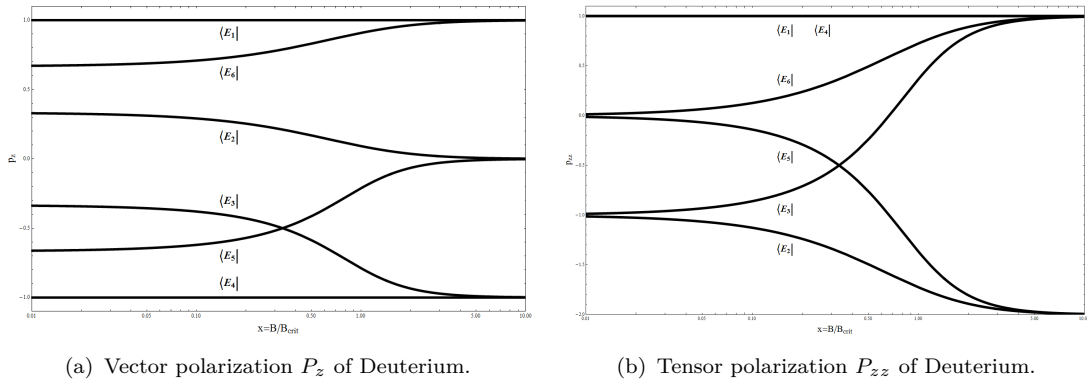
Figure 3.12: Vector polarization(P_z) and tensor polarization(P_{zz})of the deuterium atoms in the external magnetic field.

It is hardly possible to further separate the components within the same group using the same trick due to the small energy splits between them. Take the deuterium as example, the states $|E_1\rangle$, $|E_2\rangle$ and $|E_3\rangle$ can be easily separated from the other states $|E_4\rangle$, $|E_5\rangle$ and $|E_6\rangle$ utilizing an inhomogeneous magnetic filed, however the states with the same m_S in strong magnetic field, for example $|E_1\rangle$, $|E_2\rangle$ and $|E_3\rangle$, are hard to be separated further. Thus, for an atom ensemble from an ideal Stern-Gerach separator, the nuclear polarization (either P_z or P_{zz}) in strong magnetic field is zero for both Hydrogen and Deuterium. Due to the hyperfine interaction between the electron and the nucleus (proton or deuteron in our case), the polarizations will be increased in the medium and weak filed[3], but the maximum polarizations are far beyond reach. In order to obtain higher nuclear polarizations, the occupation numbers of the hyperfine Zeeman components have to be changed. The adiabatic passage method was proposed more than half century ago [90] to transit the atoms between different hyperfine Zeeman states. It has been proven to be very effective in increasing the nuclear polarization and has been employed widely in the spin physics community. In what follows, we shall present the basic idea of the adiabatic passage method in a semi-classical way. Strict analytic solutions with time-dependent Schrödinger equations can be found in Refs. [93–95].

A particle with magnetic moment in a magnetic field will precess about the direction of the magnetic field due to the torture exerted by the magnetic field. This motion is usually referred as Larmor precession, it can be visualized in Fig. 3.13, which illustrates a proton precessing around a magnetic field $\vec{B}$. In this plot the

---

[3]For example, without external field the vector polarization for is proton $P_z = \pm\frac{1}{2}$, and the deuteron tensor polarization is $P_{zz} = \pm\frac{1}{3}$.
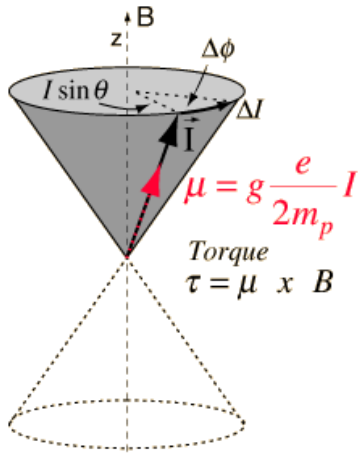
Figure 3.13: Larmor precession of proton in a magnetic field. The black and red arrows indicate the angular momentum and the magnetic moment respectively. Note only the case where the gyromagnetic ratio $\gamma > 0$ is illustrated in this plot, the red arrow should point to the opposite direction of the angular moment if $\gamma < 0$.

proton spin is denoted as $\vec{I}$, and the associated magnetic moment is

$$\vec{\mu} = \gamma \vec{I} = g \frac{e}{2m_p} \vec{I} \tag{3.17}$$

the proton experiences a torque

$$\vec{\tau} = \vec{\mu} \times \vec{B} \tag{3.18}$$

which causes the angular moment to precess. Denote the change of the angular moment in a infinitesimal time Δt as ΔI, it can be expressed as

$$\Delta \vec{I} = \Delta \vec{\phi} I \sin \theta \tag{3.19}$$

where $\Delta \vec{\phi}$ is the change of the azimuthal angle and θ is the angular between magnetic field $\vec{B}$ and angular moment $\vec{I}$. By definition the torque is the change rate of the angular momentum:

$$\vec{\tau} = \frac{d\vec{I}}{dt} \tag{3.20}$$

Combine Eq. 3.17, 3.18, 3.20 and the directive form of Eq. 3.19, the angular velocity of the Larmor precession, which is often referred as Larmor frequency, is calculated steadily as

$$\vec{\omega}_L = \frac{d\vec{\phi}}{dt} = \gamma \vec{B} \tag{3.21}$$

Above discussion is only confined to the case of static magnetic field, it can be seen that the angular moment is aligned with the external magnetic field. Image the magnetic field is reversed to its opposite direction, the magnetic moment will follow if the process goes slowly enough, in the manner the angular moment will get

flipped as well. In the case of the Hydrogen or Deuterium atom, the nuclear spin will flip along with the electron spin. This is the basic principle of how to change the hyperfine Zeeman states. The remaining issue is how to reverse the external magnetic field. The adiabatic passage method, which is employed in the polarized atomic beam source (ABS) to realize the magnetic filed reversal, will be presented in the following. Essentially, the so-called adiabatic passage is a combination of one gradient static magnetic field and one homogeneous radio-frequency (rf) magnetic field, which are perpendicular to each other. In the laboratory reference frame, we define the beam direction as z axis and the direction of the magnetic field as y axis, x axis is chosen in such a manner that the usual right-handed coordinate is formed. The rf magnetic field oscillates along x axis with certain frequency ω_0 as indicated by the dashed double-sided arrow in the left panel of Fig.3.14, it is expressed as

$$\vec{B}_x = 2B_1 \cos \omega_0 \vec{e}_x \tag{3.22}$$

in the laboratory system. This oscillating magnetic field can be viewed equivalently as two magnetic fields rotating about the y axis clockwise and counterclockwise with frequency ω_o in the xz plane, i.e.

$$\vec{B}_+ = B_1[\cos (\omega_0 t)\vec{e}_x - \sin (\omega_0 t)\vec{e}_z] \tag{3.23a}$$
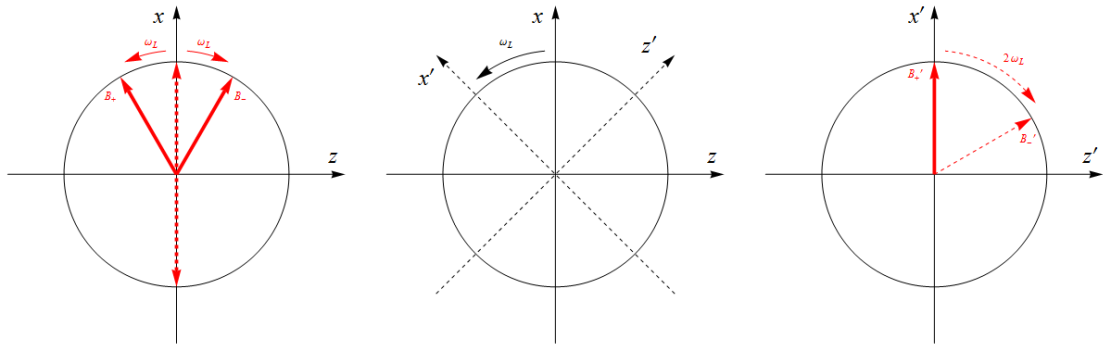
Figure 3.14: The homogeneous magnetic field is realized by an rf field B_{rf} (dashed double arrow in the left panel), it can be regarded as two field B_- and B_+, rotating clockwise and counterclockwise with frequencies $\pm\omega_L$ respectively. In the co-rotating frame, which co-rotate with B_+ (see the middle panel), the rf field is decomposed into a static field B'_+, and a rotating field whit a frequency $2\omega_L$, as illustrated by the right panel.

and

$$\vec{B}_- = B_1[\cos(\omega_0 t)\vec{e}_x + \sin(\omega_0 t)\vec{e}_z] \tag{3.23b}$$

The spin reversal process is best described in a Cartesian coordinate which co-rotates with $\vec{B}_+$. As illustrated in the middle panel of Fig. 3.14, this co-rotating coordinate is linked to the lab-fixed coordinate by the following relations:

$$\vec{e}_{x'} = \cos(\omega_0 t)\vec{e}_x - \sin(\omega_0 t)\vec{e}_z \tag{3.24a}$$

$$\vec{e}_{y'} = \vec{e}_y \tag{3.24b}$$

$$\vec{e}_{z'} = \sin(\omega_0 t)\vec{e}_x + \cos(\omega_0 t)\vec{e}_z \tag{3.24c}$$

In the co-rotating system the rf-magnetic field is decomposed into one static homogeneous magnetic field

$$\vec{B'_+} = B_0 \vec{e'_x} \tag{3.25a}$$

and one magnetic field rotating with frequency $2\omega_0$

$$\vec{B'_-} = B_0[\cos(2\omega_0 t)\vec{e'_x} + \sin(2\omega_0 t)\vec{e'_z}] \tag{3.25b}$$

The counterclockwise rotating field $\vec{B'_-}$ does not play a role since it is off resonance.

As depicted by the solid arrows in Fig. 3.15, the static inhomogeneous magnetic field changes slowly from an initial value $B_y = B_0 + \Delta B_0$ to a final value $B_y = B_0 - \Delta B_0$ along the beam direction in the laboratory system. Note that B_0 stands for a magnetic field in which the magnetic moment precesses synchronously with the clockwise rotating field $\vec{B}_+$ with a Larmor frequency $\omega_L = \omega_0$, this statement is equivalent to the following expression:

$$\omega_0 = \gamma B_0 \tag{3.26}$$

The dotted arrows indicate the field variation from ΔB_0 to $-\Delta B_0$ in the co-rotating system. If observed in the co-rotating system, the magnetic moment does not precess around the y' axis as it dose in the laboratory system. Instead, it precesses around the effective magnetic field $\vec{B}_{eff}$ which is superposed by the
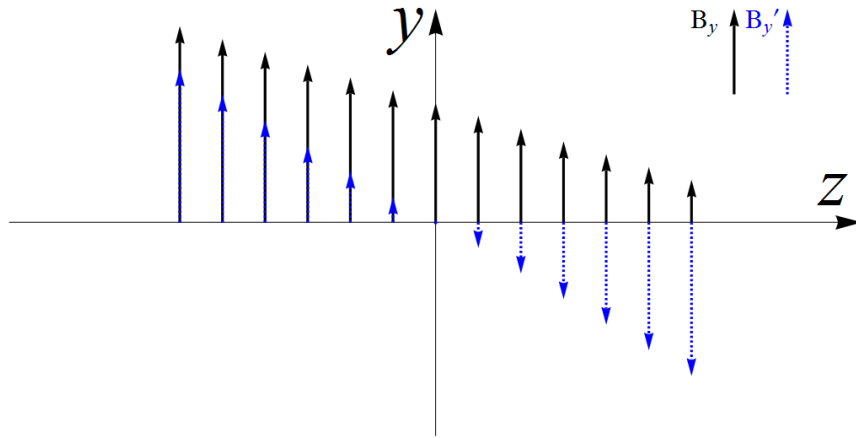
Figure 3.15: The static magnetic field varying with respect to the beam direction. The sold and dashed arrows represent the field in the laboratory and co-rotating frames respectively. A negative gradient is indicated, while in the real case the gradient can be also plus.

homogeneous field $\vec{B}_x = B_1 \vec{e_x}$ and the gradient field $\vec{B}_y$. It is straightforward that, if the initial and final values of the gradient field are much larger than the homogeneous field in the co-rotating system, i.e.

$$\Delta B_0 \gg B1 \tag{3.27}$$

the effective filed will point approximately upward in the beginning, and change its direction as ΔB_0 decreases, finally it will point downwards, in another words, the effective magnetic field gets flipped. This process is illustrated intuitively in Fig. 3.16, the effective field is indicated by green arrows. As mentioned before, the magnetic moment, which precesses around the effective magnetic field gets flipped as well, as long as the effective field changes adiabatically.

To satisfy the adiabatic condition, the Larmor frequency should be much larger than the frequency which the effective field varies with at all points. Denote the angle between y axis and effective field by θ, from the basic geometry relation

$$\tan\theta = \frac{B_1}{B'_y} \tag{3.28}$$

the angular velocity of the effective field $\vec{B}_{eff}$ can be derived as

$$\omega_{eff} = \frac{d\theta}{dt} = -\frac{B_1}{B_1^2 + B_y'^2}\frac{dB'_y}{dz}v_{atom} \tag{3.29}$$

where v_{atom} is the z component of the atom velocity. Assume the gradient field $B_y(z)$ varies linearly along z axis, then the effective field rotates most quickly and the Larmor frequency is minimum at the point where $\vec{B}'_y = 0$, therefore the adiabatic condition is

$$\frac{v_{atom}}{B_1}\frac{dB_y}{dz} \ll \gamma B_1 \tag{3.30}$$

In Summary, both the polarization condition 3.27 and the adiabatic condition 3.30 should be satisfied in order to achieve a complete spin reversal. It should be noted that, in the above discussion the oscillating rf field is chosen to be perpendicular to the beam direction, actually it can be oriented in any direction, as long as it is orthogonal to the gradient field. For instance in the weak-field (WFT) and medium-field (MFT) transition units of the ANKE ABS [96] and of the HERMES ABS [96], the rf field is parallel to the beam direction, whereas in the strong-field transition unit (SFT) it is oriented as to form an angle with the beam.

According the strength of the magnetic field B_0 the rf transitions can be classified into three types:

- WFT (Weak-field transition, $B_0 \ll B_{crit}$): in weak magnetic field the electron spin and the nuclear spin are coupled thus F is a good quantum number, mutual transformations take place between Zeeman states with opposite m_Fs. Zeeman states of the same atomic spin number F are nearly equidistant on the Breit Rabi diagram (refer Fig. 3.10). Since quantum transitions between non-neighboring states are forbidden, the rf frequency is adjusted to
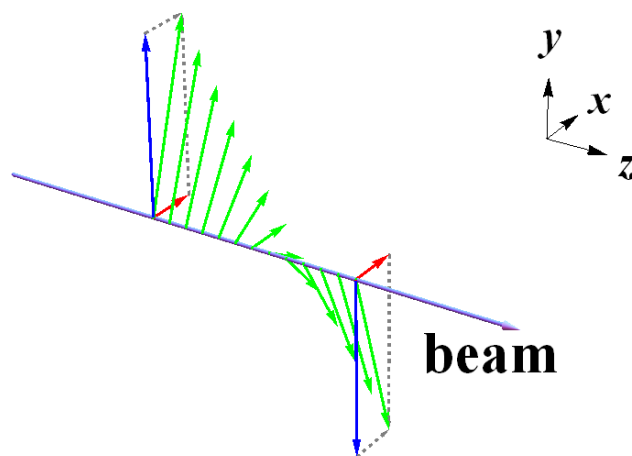
Figure 3.16: Visualization of the spin reversal. The effective magnetic field B_{eff}, which is indicated in green, is the superposition of the gradient B_{grad} (blue) and homogeneous B_{hom} (red) fields. The spin, which is coupled to B_{eff}, gets reversed along with B_{eff}. Note B_{hom} can lie in any direction in the xz plane.

match the energy difference between the neighboring Zeeman states. Transformation between non-neighboring states is realized by a series of successive transitions between neighboring states. Via WFT, interchange between Zeeman states $|E_1\rangle$ and $|E_3\rangle$: $1 \leftrightarrow 3$ occurs for hydrogen, and for deuterium the interchanges

$$1 \leftrightarrow 4,\ 2 \leftrightarrow 3,\ 5 \leftrightarrow 6$$

take place simultaneously.

- MFT (Medium-field transition, $B_0 < B_{crit}$): in this case the difference of energy splits between different pairs of Zeeman components are larger enough to allow single transitions between states of same F. Typical transitions are

$$1 \leftrightarrow 2,\ 2 \leftrightarrow 3$$

for hydrogen and

$$1 \leftrightarrow 2,\ 2 \leftrightarrow 3,\ 3 \leftrightarrow 4,\ 5 \leftrightarrow 6$$

for deuterium.

- SFT (Strong-field transition, $B_0 \geq B_{crit}$): unlike WFT and MFT, which can only induce transitions within one multiplet, the strong-field transition can be also employed to realize transitions between the states belonging to different multiplet. The most commonly used strong-field transitions are

$$1 \leftrightarrow 4$$

for hydrogen and

$$2 \leftrightarrow 6,\ 3 \leftrightarrow 5$$

for deuterium. Furthermore, the gradient field and the rf frequency can be configured in such a way that certain consecutive transitions, e.g. $3 \rightarrow 4$, $2 \rightarrow 3$, $1 \rightarrow 2$, which is equivalent to $1 \rightarrow 4$, can be achieved.

In correspondence to the rf transitions discussed above there are three types of rf transition units which, together with the multiple magnet, are the basic tools employed in the polarized atomic beam source (ABS) for the spin manipulation.

Various polarization modes can be prepared using these tools in different configurations. Depending on the change of the quantum number m_F the rf transition can be classified as π transition ($\Delta m_F = 0$) or σ transition ($\Delta m_F = \pm 1$). According to the rotation symmetry the π transition can only be induced by the rf magnetic filed perpendicular to the static magnetic field and the π transition can only be induced by the rf magnetic filed parallel to the static magnetic field [111]. In practice the WFT and MFT only induce π transitions ($\Delta F = 0, \Delta m_F = \pm 1$), whereas the SFT can induce both π and σ transitions ($\Delta F = \pm 1, \Delta m_F = 0, \pm 1$).

3.3.1.2 Components of ABS

In section 3.3.1.1, we discussed the hyperfine Zeeman effect of Hydrogen and Deuterium, the Stern-Gerlach type spin separation, and the rf transitions of Zeeman states, which are all essential to understand the working principle of the polarized atomic beam source (ABS). Now we shall turn to the units which enable the spin separation and Zeeman-state transitions, as well as other important components. Fig. 3.17 is a front sectional drawing of the polarized atomic beam source (ABS) at the ANKE spectrometer, the storage cell (SC) is indicated as well. Different colors are used for the representations of different functional components. Molecules (H_2 or D_2) are first dissociated into atoms in the dissociator and then injected through a skimmer and a collimator into the chambers which house the devices used for spin manipulations. These spin-manipulation devices include two groups of sextupole magnets for spin separation and three rf transition units (WFT, MFT and SFT) for spin reversal. The medium-field transition unit is placed between the two sextupole-magnet groups, while the weak-field and strong-field transition units are placed after the second sextupole-magnet group and before the exit of the ABS.
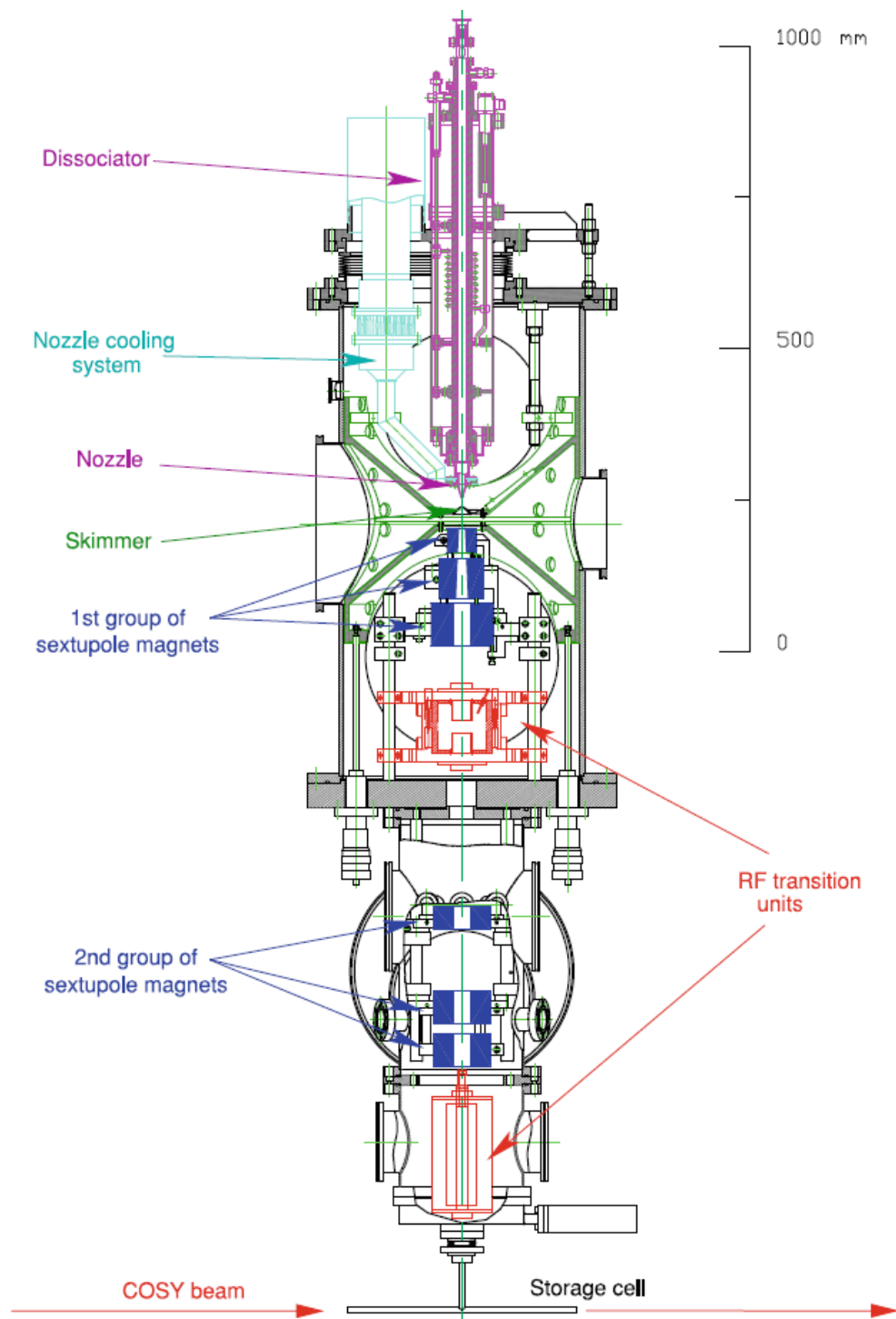
Figure 3.17: Profile of the polarized atomic beam source (ABS) at the ANKE spectrometer. Components of different functionalities are distinguished by color. The dissociator tube and the nozzle which is installed at its lower end are drawn in mulberry, the nozzle cooling system is indicated by cyan. The skimmer, together with the conical baffles, are represented by green color. The two groups of spin separate devices, each comprising of three sextupole magnets, are drawn in blue. The components drawn in red are the rf transition units, the medium field transition units (MFT) is placed in the middle chamber whereas the weak (WFT) and strong (SFT) field transitions units are installed in the last chamber. The storage cell as well as the COSY beam are schematically draw at the bottom. Auxiliary parts such as pumps and control system are not drawn.
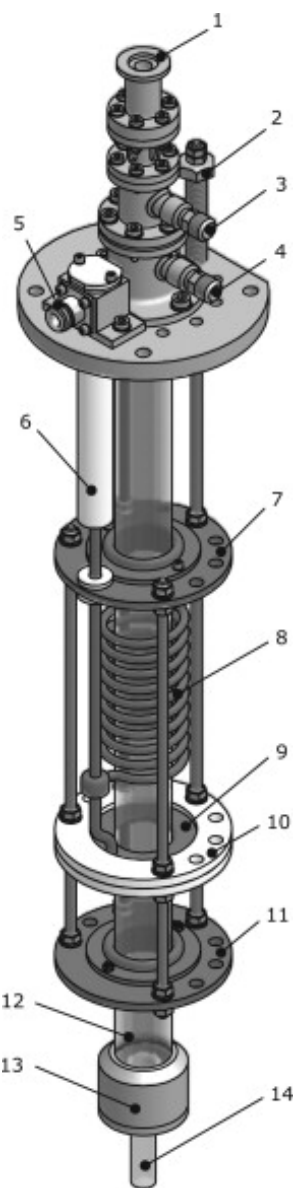
(a) 3D view of the dissociator tube.
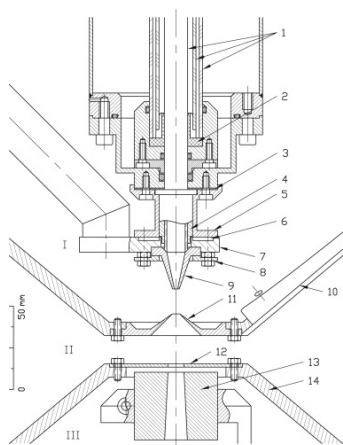
(b)

Figure 3.18: Dissociator.

Unpolarized atomic beam source In order to perform spin manipulations one has to first dissociate the hydrogen/deuterium molecules into neutral atoms. This function is realized by the unpolarized atomic beam source, which, as shown in Fig. 3.18, is made up of a dissociator, a beam forming system consisting of nozzle, skimmer and collimator, as well as a nozzle cooler. The stereogram in Fig. 3.18(a) illustrates the dissociator, which is based on an rf plasma discharge. The discharge is essentially composed of a pair of rf capacitor (7, 9) and coil (8) which are fed by a 13.56 MHz generator through the rf input (5). The molecules enter the discharge tube through the gas inlet (1). Under the effect of the rf electric field produced by the capacitor the molecules will be ionized as plasma, which in turn will transform into neutral atoms outside the discharge region. The magnetic field generated by the coil increases the distances that the electrons travel in the electric field thus increases the ionization rate. The sliding ground connection (2) and rf connection (6) enable the distance from the rf capacitor and coil, which are fixed rigidly to each other, to the exit of the discharge tube，to be adjustable within certain freedom. To maintain the discharge process in a stable condition the released heat has to be transferred out of the discharge tube timely, for this purpose two extra glass tubes are installed coaxially with respect to the discharge tube (see label (1) in the cross-section plot 3.18(b)). The space between the discharge tube and the middle tube allows the coolant to cool the discharge tube by heat convection, at the lower end the coolant is reversed by the reversal piece and flows upwards to the coolant outlet through the slit between the middle and outer tubes. The

coolant is a mixture of water and ethanol with approximately the same amounts, circulating in a closed loop, its temperature at the inlet is stabilized using a thermostat. As shown in Fig. 3.18(b), the beam forming system includes the nozzle (9), skimmer (11) and collimator (12), the nozzle is installed at he lower end of the dissociator while the skimmer and the collimator are fixed at the upper and lower baffles respectively. The nozzle is made of 99.5% Al and is cooled via connecting to the coolhead by a Cu heat-bridge. Note the lower baffle is not attached to the vessel and can be move axially, the same is true for the dissociator, as results the positions of the collimator and of the nozzle can be adjusted in the beam direction. Therefore the maximum beam intensity can be achieved by tune the distances between plasma, nozzle, skimmer and collimator.

Spin-separator: sextupole magnets As already mentioned in section 3.3.1.1, cylindrically symmetric multiple magnet rather than tapered dipole magnet ought to be adopted as spin separator so that beam of high quality can be produced. For a 2m-pole magnet its scalar potential is expressed in a general form as

$$\Phi = cr^m \cos m\phi \tag{3.31}$$

in the polar coordinate, the coefficient c above is a constant which does not concern the present discussion. Using the relation $\vec{B} = -\nabla\Phi$ the field magnitudes of the most popular multiple magnets, i.e. the quadrupole and sextupole magnets, are obtained:

$$B = \frac{B_{tip}}{r_{tip}} \cdot r \ (quadrupole) \quad and \quad B = \frac{B_{tip}}{r_{tip}^2} \cdot r^2 \ (sextupole), \tag{3.32}$$

here B_{tip} is the field strength at the pole tips and r_{tip} is distance from the pole tips to the center. In a magnetic field the force exerted on an atom is

$$\vec{F} = -\nabla W = -\frac{\partial W}{\partial B} \cdot \frac{\partial B}{\partial r} = \mu_{eff}\nabla_r B. \tag{3.33}$$

The notation μ_{eff} stands for the effective magnetic moment, which is constant for a pure hyperfine Zeeman state but varies with the magnetic strength for a superimposed state. The field gradients $\nabla_r B$ is calculated by differentiating the magnetic filed with respect to the radius, which yields

$$\nabla_r B = \frac{B_{tip}}{r_{tip}} \ (quadrupole) \quad and \quad \nabla_r B = \frac{2B_{tip}}{r_{tip}^2} \cdot r \ (sextupole), \tag{3.34}$$
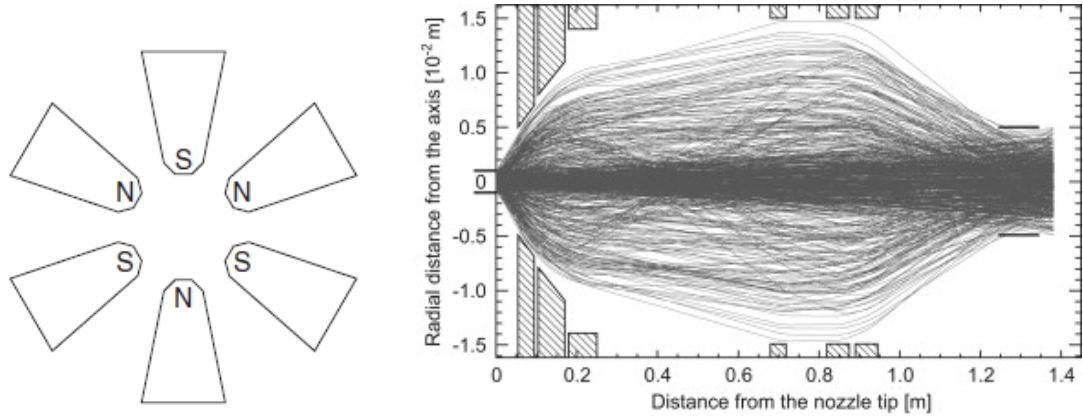
Figure 3.19: The arrangement of the sextupoles in the ABS at ANKE, the lines are the simulated trajecroies of the atoms with positive μ_{eff}. From left to right the tip-field stengths of these magnets are 1.630, 1.689, 1.628, 1.583, 1.607 and 1.611 T.

One would immediately notice that the focusing/deocusing force acting on an atom is independent of the radius r in the quadrupole filed, whereas is proportional to r in the sextupole. This distinctive feature of the sextupole leads to a advantage that the chromatic aberration caused by the beam momentum spread can be compensated, therefore sextupole is widely used as the spin separator in the polarized atomic beam source. Fig. 3.19(a) schematically shows the cross section of a sextupole (with its field lines indicated), note the inner radius is exaggerated compared with the poles. The attributes of the spin separator system that affect the spin separation efficient and the beam transmission rate are the field strengths and the geometries, which were optimized by performing track simulation. Fig. 3.19(b) shows the magnet arrangement of the ABS at ANKE, the field strengths of these magnets are given in the caption.

RF transition units From the discussion on the principle of the rf transition it is clear that an rf transition unit is nothing but a combination of an rf magnetic field B_{rf} and a static magnetic field B_{stat}, which is gradient with respect to the beam axis. In what follows, we shall introduce the techniques and components that realize these magnetic fields as well as the auxiliary parts. In the pioneering researches [8] the gradient static magnetic field B_{stat} was provided by a permanent dipole magnet which is tapered along the beam direction. Electromagnets with adjustable pole faces were reported latter [98, 99]. Presently a type of novel gradient magnet has been developed and successfully used in the modern polarized

(a) Three-quarter-section view of MFT unit.

(b) Circulate producing the static gradient magnetic field.
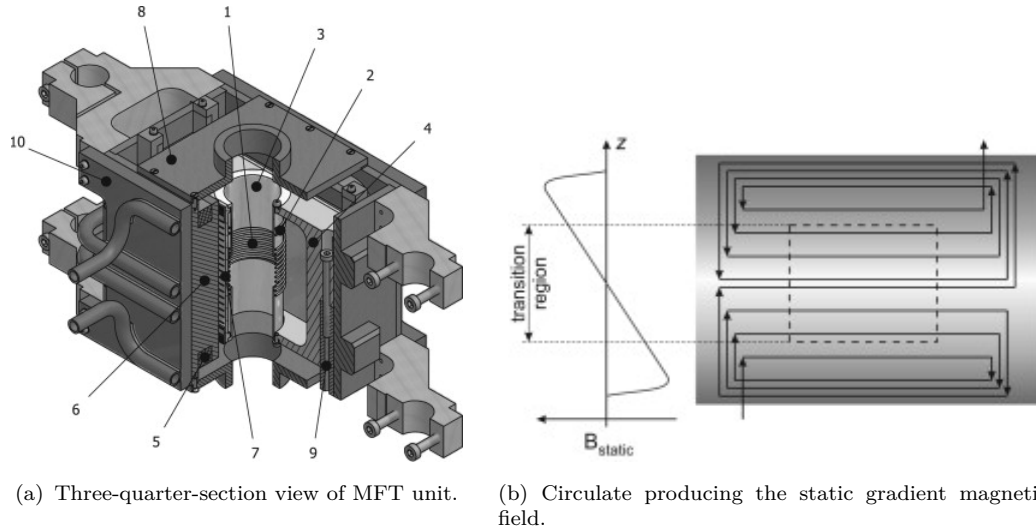
Figure 3.20: Layouts of the rf transition unit.

atomic beam sources [85, 96]. Fig. 3.20(a) shows a three-quarter-view of the medium field transition unit (MFT) installed on the polarized atomic beam source at ANKE, where the gradient static magnetic filed B_{stat} is essentially a superposition of a homogeneous magnetic field B_{hom} and a gradient magnetic field B_{grad}. The homogeneous magnetic field B_{hom} is produced by a pair of Helmholtz coil (6). On the other hand the gradient component B_{grad} is maintained by a separate circular (see Fig. 3.20(b)) which is installed on a grooved aluminium plate (see label 7 in Fig. 3.20(a)). On the left-hand side of Fig. 3.20(b) B_{grad} is plotted as a function of the positions on the beam axis (z). Note only the region where the field gradient $\frac{dB}{dz}$ is constant is used for transition. For the weak-field (WFT) and mediate-field (MFT) transition units, the radio frequency field B_{rf} is produced by an rf solenoid coil. As shown in Fig. 3.20(a) the solenoid is installed inside a grooved aluminium tube (3) which is placed along the beam axis. To induce the transitions between different Zeeman multiplets the strong field transition unit (SFT) is operated at frequencies higher than the hyperfine splitting frequencies[4]. In addition the SFT ought to accomplish not only the π transitions ($\Delta F = 1$, $\Delta m_F = \pm 1$) but also the σ transitions ($\Delta F = 1$, $\Delta m_F = 0$), which means the rf magnetic field should has both orthogonal and parallel components with respect to the static magnetic field. Such magnetic field can not be excited by the rf solenoid, instead it is produced by the two-line resonator, which will be introduced in the following.

A two-line resonator is consist of two copper $\frac{\lambda}{4}$ resonant rods inside a copper cavity. The two rods are fed by rf powers with a relative phase shift of π, as a

---

[4]1421.4 MHz for hydrogen and 372.4 MHz for deuterium respectively.

(a) Three-quarter-section view of MFT unit.

(b) Circulate producing the static gradient magnetic field.
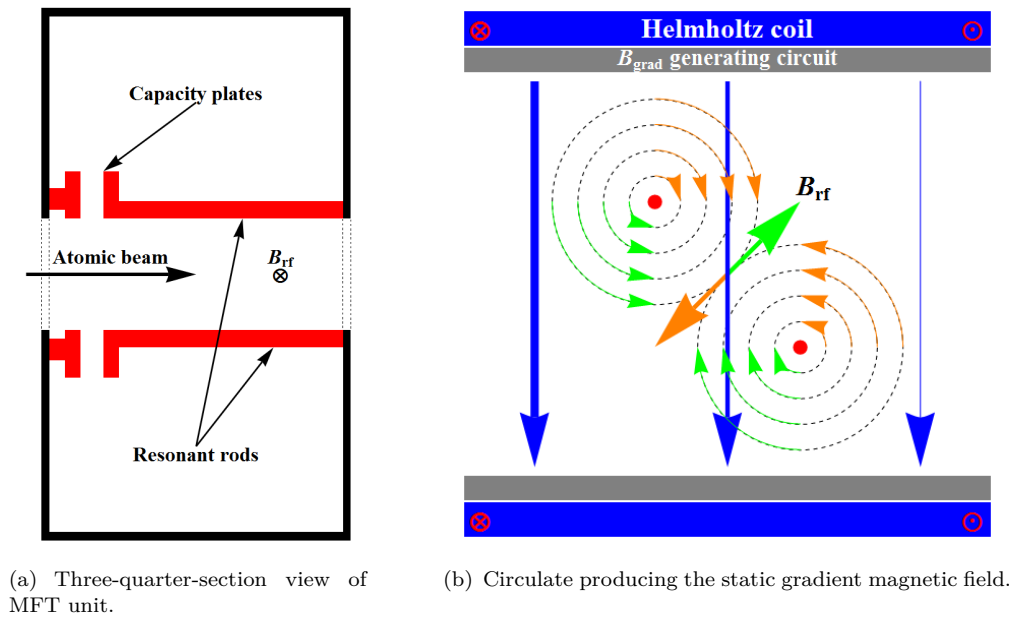
Figure 3.21: Layouts of the rf transition unit.

result the oscillating fields excited by the rods will superimpose to an rf magnetic field in between the two rods, oscillating perpendicularly to the plane where the rods locate in. In principle a resonant rod should have a length of a $\frac{\lambda}{4}$ with one open and one grounded end, however a capacity at the open end can shorten the rods. Moreover a variable capacity allows to tune the resonance frequency. In order that both π and σ transitions can be enabled, the resonator rods are placed in a plane which has a certain angle relative to the static magnetic field, so that both parallel and orthogonal fields are realized. In the ANKE ABS the SFT and WFT share a common Helmholtz coil.

3.3.1.3 Polarization modes

Combining the spin-separate magnets and the rf transitions units, a variety of polarized atomic beams can be prepared by the atomic beam source (ABS). Table. 3.2 and 3.3 present the polarization modes of the hydrogen and deuterium targets respectively. The rf transitions employed, as well as the Zeeman states in the polarized beams, are also listed along with the polarization modes. The deuterium modes marked by color were used in the present research.

Table 3.2: Polarized hydrogen target states.

Pol. mode	Transitions			Zeeman states				Ideal polarization
	MFT	WFT	SFT	$|E_1\rangle$	$|E_2\rangle$	$|E_3\rangle$	$|E_4\rangle$	P_z
1				●	●			0.00
2	$2 \to 3$			●				1.00
3	$2 \to 3$	$1 \to 3$				●		-1.00

Table 3.3: Polarized deuterium target states.

Pol. mode	Transitions			Zeeman states						Ideal polarizations	
	MFT	WFT	SFT	$|E_1\rangle$	$|E_2\rangle$	$|E_3\rangle$	$|E_4\rangle$	$|E_5\rangle$	$|E_6\rangle$	P_z	P_{zz}
1				●	●	●				0.00	0.00
2	$3 \to 4$			●	●					0.50	-0.50
3		$1 \to 4, 2 \to 3$			●	●	●			-0.67	0.00
4	$3 \to 4$	$1 \to 4, 2 \to 3$				●	●			-1.00	1.00
5			$2 \to 6$	●		●			●	0.33	1.00
6	$3 \to 4$		$2 \to 6$	●					●	1.00	1.00
7			$3 \to 5$	●	●			●		0.33	-1.00
8	$3 \to 4$		$3 \to 5$	●	●		●			0.00	0.00
9	$1 \to 4$				●	●				-0.50	-0.50
10	$1 \to 4$		$2 \to 6$			●			●	0.00	1.00
11	$1 \to 4$		$3 \to 5$	●				●		0.00	-2.00

3.3.2 Storage Cell

The maximum beam intensity of the hydrogen/deuterium jet produced by the polarized atomic beam source is $10^{17} \ s^{-1}$, which corresponds to a target thickness of $2 \times 10^{11} \ cm^{-2}$ [35] for a free ABS jet. On the contrary, the unpolarized cluster [55] target can generate cluster gas target with target thickness of $5 \times 10^{14} - 10^{15} \ cm^{-2}$. In order to accumulate high statistics thus obtain results of high precision, a storage cell[100, 101] has to be utilized to increase the luminosity when the polarized internal target is used for an experiment. As indicated in Fig. 3.17 a storage cell is installed at the bottom the atomic beam source. A storage cell is composed of a feeding tube and a beam tube, the atomic jet produced by the ABS enters the storage cell through the feeding tube and diffuses in the beam tube, where it interacts with the COSY beam. When a storage cell is used, the target thickness of the polarized internal target can be increased by two orders of magnitude[101]. Fig. 3.22(a) shows the variation of the atom density along the beam tube, which has the maximum value at the integration point with the feeding tube, and linearly decreases with the distance from the feeding tube. The atom density at the feeding tube is given by

$$\rho_0 = \frac{I_{ABS}}{C} \tag{3.35}$$

where I_{ABS} (s^{-1}) is the flux of the free ABS jet, and

$$C = 3.81 \times 10^3 \sqrt{\frac{T}{M}} \sum_{i=1}^{3} \frac{D_i^3}{L_i + 1.33 D_i} \qquad (3.36)$$

is the conductance [102]. In Eq. 3.36 T represents the temperature of the cell wall measured in Kelvin, M is the molar mass, D_i and L_i denote respectively the inner diameters and the lengths of the front $(i = 1)$ and back $(i = 2)$ parts of the beam tube as well as the feeding tube $(i = 3)$. The target thickness in the beam tube is calculated as the integration of the atom density along the beam line, since the atom density decreases linearly, the target thickness is given by

$$d = \frac{1}{2} L_b \rho_0 \propto \frac{1}{D_b^3} \qquad (3.37)$$

where $L_b = L_1 + L_2$ and $D_b = D_1 = D_2$ denote the total length and the inner diameter of the beam tube respectively. From Eq. 3.37 one concludes that the diameter of the beam tube ought to be made as small as possible in order to have a large target thickness. However, the minimum cross section of the beam tube is limited by the COSY beam size at the ANKE interaction point as well as by the betatron oscillations during the beam acceleration. Through studying the phase space of the COSY beam at different energies, the ANKE collaboration had determined the optimum cross section of the beam tube as a rectangle of 20×15 mm^2, which has four quadrants with diameters of 2 mm as its corners. The feeding tube is a 130-mm long cylinder with a inner diameter of 15 mm. Restricted by the geometry of the ANKE target chamber, the feeding tube is connected asymmetrically to the beam tube. Detailed structure and parameters of the storage cell are depicted in Fig. 3.22(b). In order to minimize the background events which are produced by the interaction between the beam halo and the cell walls, the storage cell is manufactured with Aluminum foil with a small thickness
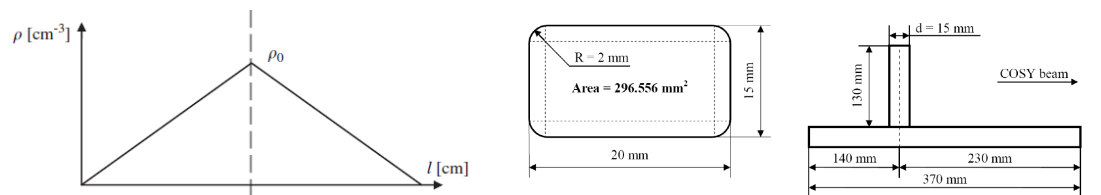
(a) Distribution of the atom density along the beam tube in the storage cell.

(b) Cross section of the beam tube and side view of the storage cell.

Figure 3.22: Storage cell.

of 25 μm. In addition, the inner walls are coated with a layer of Teflon to reduce to depolarization effects.
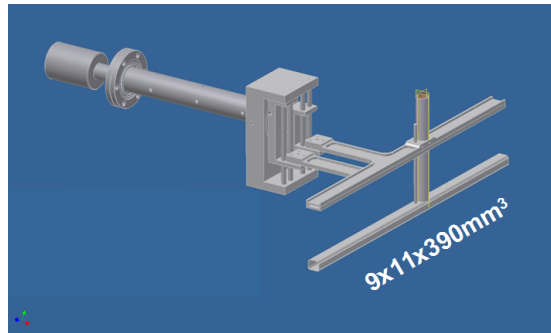
Figure 3.23: Openable storage cell.

For double polarized experiments, due to the low flux of the ions generated by the polarized sources [103], the beam intensity in the COSY ring can only reach 500 nA after a single injection, which can not meet the requirements of the experiments demanding high luminosities. A multiple-injection technique which involves the cooling-stacking procedure can significantly enhance the beam intensity in the storage ring by five times [104]. However, the beam transverse phase space during the cooling-stacking process is so big that a storage cell as described above will destroy the beam. To overcome this problem an openable storage cell has been developed. Fig. 3.23 shows the openable storage cell, the beam tube will keep open during the cooling-stacking process, it will be closed to increase the target density as soon as the cooling-stacking is finished. The openable storage cell is open, so its size is not limited by the betatron oscillations, consequently the cross section of the beam tube can be smaller than 20×15 mm^2, thus a higher target thickness can be achieved using the openable storage cell.

3.3.3 Lamb-shift Polarimeter

A reliable polarimeter is indispensable to a polarized target for measuring the polarizations as well as tuning the machine settings. For the polarized hydrogen/deuterium targets, the Breit-Rabi type and Lamb-shift type polarimeters are most commonly adopted. As one of the major components of the ANKE polarized internal target, a Lamb-shift polarimeter(LSP) [87, 88] has been developed and successfully used in many polarized experiments at ANKE. The Lamb-shift polarimeter utilizes the three-level interaction among the states $2^2S_{\frac{1}{2}}$, $2^2P_{\frac{1}{2}}$ and $1^2S_{\frac{1}{2}}$ [107] to select the atoms with particular nuclear spin orientations(m_I) and

measures the X rays released by Lyman transitions, whose intensities are proportional to the occupation numbers of the corresponding nuclear spin states. The Lamb-shift spin filter[109, 110] is the central part of the Lamb-shift polarimeter, therefore subsection 3.3.3.1 is devoted to its working principle. In subsection 3.3.3.2 the working process of Lamb-shift polarimeter will be introduced.

3.3.3.1 Three-level Interaction and Lamb-shift Spin Filter

According to Dirac theory, atomic states with the same principle quantum numbers n and total angular momentum quantum number j but different orbital angular momentum quantum number l should be degenerate. On the contrary, in 1947 Lamb and Retherford discovered that the energy of the hydrogen state $2^2S_{\frac{1}{2}}$ was slightly higher than that of $2^2P_{\frac{1}{2}}$ by 4.4×10^{-6} eV[106]. Customarily, the energy difference between the $2^2S_{\frac{1}{2}}$ and $2^2P_{\frac{1}{2}}$ states is referred as Lamb-shift. In the absence of external fields, the lifetime of state $2^2P_{\frac{1}{2}}$ is 1.6×10^{-9} s, it decays to the ground state $1^2S_{\frac{1}{2}}$ by dipole transition. On the other hand, $2^2S_{\frac{1}{2}}$ is a metastable state with a lifetime of about 0.1 s, its main decay mode is a two-photon radiation(lifetime $\tau \approx \frac{1}{7}$ s), the electric dipole and quadrupole transitions to the ground state are forbidden, the magnetic dipole transition is allowed but has a very long lifetime (about 2 days), the spontaneous transition to state $2^2P_{\frac{1}{2}}$ is negligible($\tau \approx 20$ years) because of the small energy difference. When a electric field $\vec{E}$ is applied, the Stark mixing [111] between the $2^2S_{\frac{1}{2}}$ and $2^2P_{\frac{1}{2}}$ states will reduce the lifetime of the $2^2S_{\frac{1}{2}}$ state τ_S and increase the lifetime of the $1^2P_{\frac{1}{2}}$ state τ_P, the relation between τ_S and τ_P can be expressed as

$$\tau_S = \tau_P \frac{\hbar^2(\omega^2 + \frac{\gamma^2}{4})}{V_E^2} \tag{3.38}$$

provided that τ_S is much longer than τ_P and much shorter than the life time of the unperturbed $2^2S_{\frac{1}{2}}$ state. In Eq. 3.38 $\Delta E = \hbar\omega$ is the energy difference between the states $2^2S_{\frac{1}{2}}$ and $2^2P_{\frac{1}{2}}$, $\gamma = \frac{1}{\tau_P}$ and the matrix element $V_E = \langle\psi_S| eEr |\psi_P\rangle$ represents the mixing strength.

In a magnetic field the Stark mixing will be affected due to the energy separations between different Zeeman states. Fig. 3.24(a) shows the Breit-Rabi diagrams of the hydrogen excited states $2^2S_{\frac{1}{2}}$ and $2^2P_{\frac{1}{2}}$, for convenience, the Zeeman components are labeled by the notations

$$\begin{array}{ll} \alpha_\pm & 2^2S_{\frac{1}{2}}, m_J = \ \ \frac{1}{2}, m_I = \pm\frac{1}{2} \\ \beta_\pm & 2^2S_{\frac{1}{2}}, m_J = -\frac{1}{2}, m_I = \pm\frac{1}{2} \end{array}$$

(a) Three-level interaction

(b) Lamb-shift spin filter
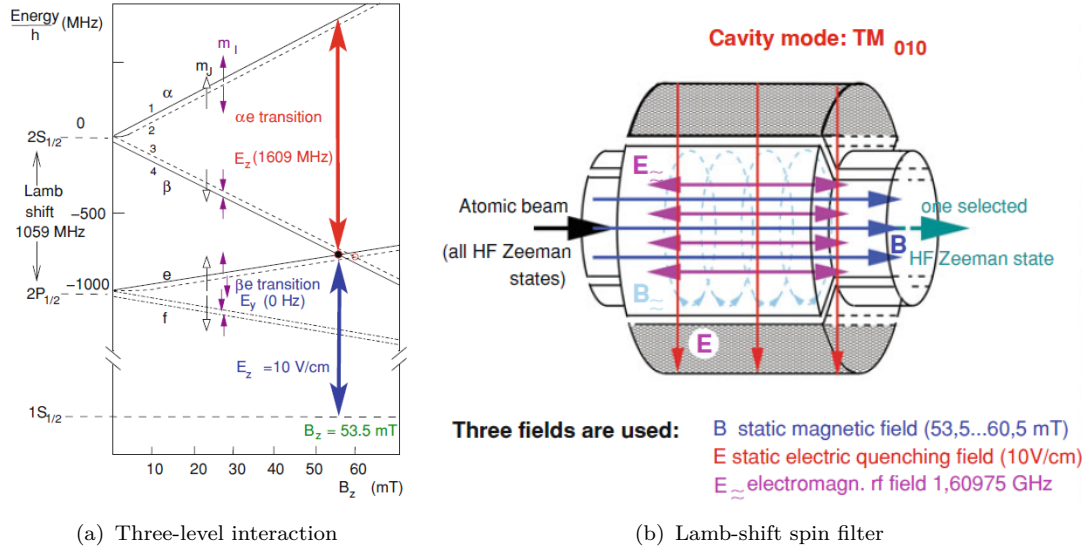
Figure 3.24: Fig. (a) is the Breit-Rabi diagrams of the hydrogen atom excited states $2^2S_{\frac{1}{2}}$ and $2^2P_{\frac{1}{2}}$, the double arrows indicated the three-level interaction. Fig. (b) shows schematically the Lamb-shift spin filter.

$$e_\pm \qquad 2^2P_{\frac{1}{2}}, \, m_J = \quad \frac{1}{2}, \, m_I = \pm\frac{1}{2}$$
$$f_\pm \qquad 2^2P_{\frac{1}{2}}, \, m_J = -\frac{1}{2}, \, m_I = \pm\frac{1}{2}$$

which were proposed by Lamb and Retherford[106]. The three-level interaction takes place in a magnetic field which is close to the level-crossings of the β and e states, where the nuclear spin $\vec{I}$ decouples with the electron angular moment $\vec{J}$, therefore the three-level interaction occurs only among the states with the same nuclear quantum number m_I. According to the selection rules related to the rotational symmetry, an electric field which is parallel to the magnetic field can only induce the mixing between the states with $\Delta m_J = 0$, while a perpendicular electric field only mixes states with $\Delta m_J = \pm 1$ [111]. In a Lamb-shift spin filter, the magnetic field is parallel to the beam direction, a transverse static electric field is applied to connect the states β and e, and a longitudinal rf electric field is applied to connect the states α and e. In normal cases[5], both α and β quench to the ground state rapidly by the Stark mixings with the state e. An equilibrium between the state α and β of a particular m_I will be established if the frequency of the rf electric field equals to the separation between these states, therefore the atoms with this nuclear spin quantum number m_I will be perservered, while other atoms will be quenched to the ground states. Selection of of the meatstable atoms with different nuclear spin states can be accomplished by adjusting the rf frequencies at a fixed magnetic field value, or by setting different magnetic values

---

[5]where the states α and β are not coupled

at a fix rf frequency. Fig 3.25 schematically shows a Lamb-shift spin filter, which is essentially a cylindrical resonant cavity composed of four quadrants, the static electric field is realized by applying dc voltages on two opposite quadrants, the magnetic field is generated by a longitudinal solenoid and the rf electric field is excited by operating the cavity in the TM_{010} mode.

3.3.3.2 Working Process of LSP
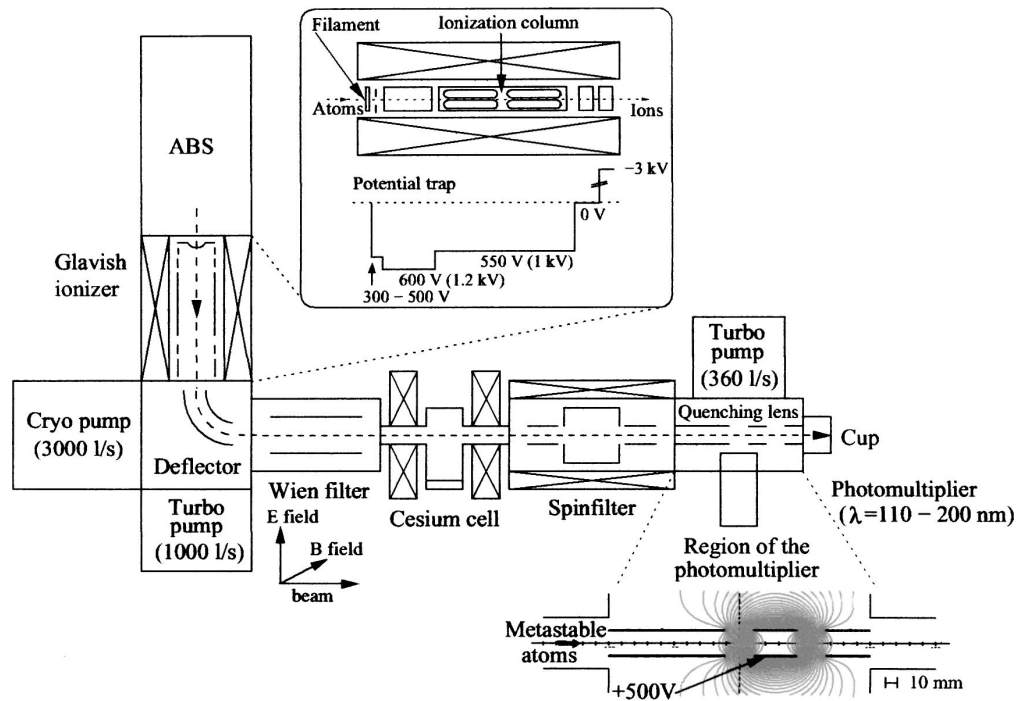
Figure 3.25: Schematic plot of the Lamb-shift polarimeter of the polarized internal target at ANKE spectrometer.

Fig. 3.25 shows a schematic plot of the Lamb-shift polarimeter at ANKE, which illustrates the main functional units as well as the working process of the L-SP. The ground-state hydrogen/deuterium atoms from the polarized atomic beam sources (ABS) are first ionized in a vertically placed Glavish-type electron-collision ionizer, in order to preserve the nuclear spin a strong magnetic field is present in the ionizer to decouple the electron and nuclear spins. The produced protons/deuterons are then directed to move along the horizontal beam line by a electrostatic deflector. The Wien filter installed next to the deflector mainly serves as a spin rotator, it rotates the nuclear spins by 90° thus provides a longitudinal polarization axis, besides, it also filters out the unwanted ions. From the discussion on the Lamb-shift spin filter (subsection 3.3.3.1) it is clear that the hydrogen/deuterium atoms have to be in the metastable state $2^2S_{\frac{1}{2}}$ in order to be filtered through

the three-level interaction. The Cesium cell installed in between the Wien filter and the Lamb-shift spin filter is used to convert the protons/deuterons into the metastable atoms by the charge-exchange reaction

$$H^+ + Cs \rightarrow H_{(2S)} + Cs^+.$$
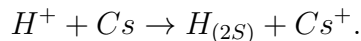
The Cesium cell is filled with Cesium vapor which is maintained by a sample of liquid Cesium of 160 $^\circ C$. A magnetic field which is sufficiently strong with respect to the critic field of the metastable atom[6] has to be applied longitudinally so that the nuclear polarization is preserved in the charge-exchange process. The Lamb-shift spin filter at ANKE is operating at a fixed frequency of 1609.8 MHz. By setting the magnetic field at the value where the hyperfine split between the α and β states with the desired nuclear spin number equals to the rf frequency, only the α state with this particular nuclear spin number can be transmitted, while other states will be quenched to the ground state. The magnetic field in the spin filter is required to be very homogeneous along the beam line, otherwise the α state to be preserved will be quenched. The transmitted metastable atoms will transit to the ground state in the quenching lens, the released Lymman-α X rays are detected by a selective photon multiply tube (PMT) which is only sensitive to the photons with wave lengths between $110 - 120$ nm. The atoms and ions leaving the quench region are finally dumped in the Faraday cup. Fig. 3.26 illustrate two
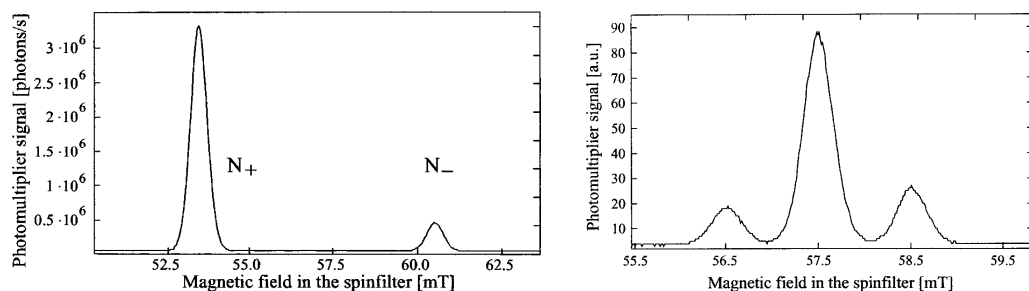
(a) A typical Lyman-α spectrum of hydrogen beam measured with the LSP, the events at the magnetic strengths 53.5 mT and 60.5 mT are of $m_I = +1$ and $m_I = -1$ respectively. The polarization corresponds to this spectrum is about $P_z \approx 0.78$.

(b) A typical Lyman-α spectrum of deuterium beam measured with the LSP, the events at the magnetic strengths 56.5 mT, 57.5 mT and 58.5 mT are of $m_I = +1$, $m_I = 0$ and $m_I = -1$ respectively. The polarizations correspond to this spectrum are about $P_z \approx -0.06$ and $P_{zz} \approx -1.09$.

Figure 3.26: Examples of the Lyman-α spectra measured with the Lamb-shift polarimeter, the left and right panels correspond to hydrogen and deuterium respectively.

---

[6]The critic field is calculated as $B_c = \Delta W/(g_J - g_I)\mu_B \approx \Delta W/2\mu_B$, where ΔW is the hyperfine split of the metastable atom. The critical field is 6.34 mT for H_{2S} and 1.46 mT for D_{2S}[8].

typical distributions of the X rays registered by the PMT in the quenching region as functions of the magnetic field value in the spin filter, the photon intensities at one particular magnetic strengths are in principle proportional to the occupation numbers of the atoms with the corresponding nuclear spin state (m_I). However, it has to be noted that the photon intensities measured by the PMT are actually not exactly proportional to the occupation numbers of the initial nuclear spin states. Some processes, for instance the collisions between the atoms with the residual gas in the quench region, can produce background. In addition, different hyperfine states are affected differently when the atoms/ions undergo variant processes (such as ionization, charger exchange etc.) in the LSP, consequently the coefficient which connect the initial occupation number and the final photon intensity is different for different state. Therefore the background has to be subtracted carefully and necessary corrections has to be made in order to perform a precise measurement [87]. It has been demonstrated that the ANKE LSP can measure the polarizations of a slow hydrogen/deuterium beam with energy up to 2 keV/4 keV with high a high precision, which depends on both beam intensity and measurement time.

Chapter 4

Study of the Proton–Deuteron Charge–Exchange Reaction

It has been stressed in chapter 2 that, in order to extend the np study at ANKE to the energy region of $T_N > r$ 1.135 GeV, one has to adopt the inverse kinematics, i.e. bombarding the deuterium target with the pron beam. Basically the research methodology remain the same, namely to measure the observables of the deuteron–proton charge-exchange reaction $pd \rightarrow n\{pp\}_s$, and to extract the elementary neutron–proton scattering amplitudes from these observables by the phase-shift analyses (PSA). However, the method of inverse kinematics has consequences in three aspects:

- A polarized deuterium target is needed, which had never been used in the previous experiments at ANKE. At ANKE, the polarized deuterium target is produced by the polarized internal target installation (PIT) [77, 78], which had been successfully used to supply polarized hydrogen target in the first phase of the ANKE np study. In addition, the laboratory measurements with the Lamb-shift polarimeter (LSP) [87, 88] had proved that the PIT was able to stably provided high-polarized deuterium target with sufficient target thickness. In spite of the above facts, one has to verify the target performances at the real experimental conditions, since the factors, such as the D2 stray field, the wall of the storage cell etc., will effect the target performances. Besides, a reliable target polarimetry has to be established prior to the production experiment in future.

- When using a deuteron beam, the protons ejected from the process $dp \rightarrow \{pp\}_s n$ are energetic enough to enter the forward (Fd) or the positive side
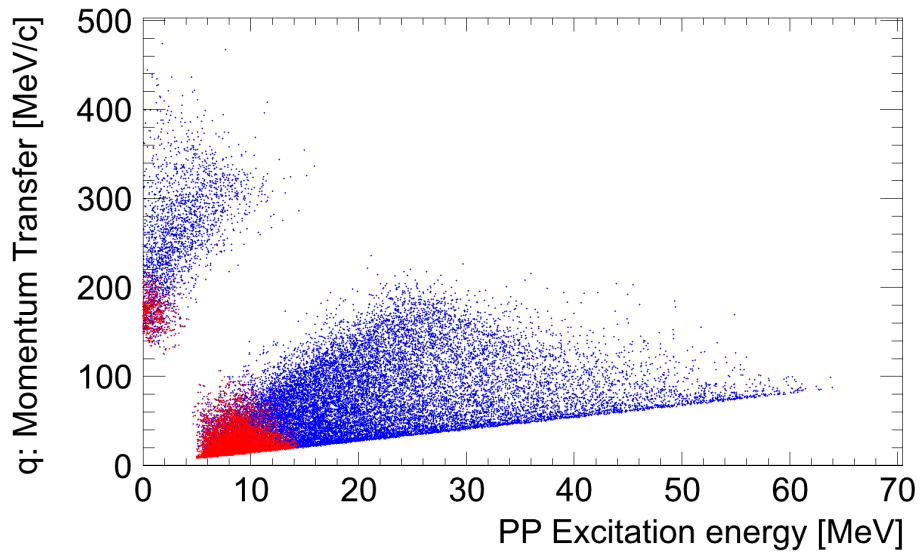
Figure 4.1: Simulation of the STT acceptance for the deuteron-proton charge exchange reaction $pd \to n\{pp\}_s$. The red and blue areas correspond the STT configurations with an without the third layer of silicon micro-strip detector. This simulation shows: 1. the third layer of silicon micro-strip detector is indispensable; 2. The STT can not cover the kinematics region where both E_{pp} and q are small, which was routinely accessible in the first phase of the ANKE np study.

(Pd) detection system. On the contrast, in the case of the inverse-kinematics process $pd \to n\{pp\}_s$ the final protons have small energies and emitted isotropically , thus are best detected by the silicon tracking telescopes (STT) that placed nearby the target. Therefore it is essential to investigate the influences of the STTs on the np study.

- As has been discussed in chapter 2 that the P wave will come into play when the excitation energy of the final proton pair E_{pp} is large (> 3 MeV), and that the multiple scattering and the relativistic effect should be taken into account if the three-momentum transfer q is large. Before the experiment, the Monte-Carlo study using the event generator PLUTO [112] and the detector simulation toolkit Geant4 [113] had shown the STT system was not able to cover the kinematics region where both E_{pp} and q are small (see Fig. 4.1. It is therefore clear that one has to study how the higher-wave component, the multiple scattering and the relativistic effect influence the impulse approximation and the phase-shift analyses (PSA) at energies where the neutron–proton amplitudes have been measured reliably, and improve the

experimental schemes as well as perform some possible modifications on the impulse approximation.

Through above discussion it can be seen that the second phase of the np study at ANKE using the inverse-kinematics method is not the simple repeat of the research in the first phase at higher energies, one needs to verify and improve the whole investigation approach prior to the production experiments by a preparatory study. Throughout this chapter we shall describe the commissioning experiment. An overview of the experiment situation is given in section 4.1. Section 4.2 is dedicated to the deuterium target polarimetry, where different methods are discussed in details. Finally the measurement of the proton–deuteron charge exchange reaction $p\vec{d} \to n\{pp\}_{^1S_0}$ is discussed in section 4.3

4.1 Overview of the Experiment

In the first phase of the ANKE neutron–proton scattering investigation, the data at the beam kinematic energy $T_d = 1200$ MeV were mainly used for polarimetry. The reason was that there were several reactions in the vicinity of this energy whose analyzing powers were measured very well previously. Besides, the np scattering amplitudes at this energy were known to be reliable, thus the comparison with the impulse approximation based on those amplitudes is meaningful. Due to above reasons this proof-of-principle (POP) experiment was performed with an unpolarized proton beam kinematic energy $T_p = 600$ MeV, which corresponds to a revolution frequency of $f = 1294.55$ kHz at COSY. In each cycle, about $N \approx 8 \times 10^9$ protons were accumulated through an injection-stacking process [59], then the data-taking lasted for 900 s, until the beam intensity was too low. After that a new cycle started. The beam intensity Nf was monitored by a beam current transformer (BCT), which picked up a voltage signal $U = NfeR$[1], induced by the circulating beam. The resolution of the BCT signal was about 1%.

The ANKE subsystems forward detector (Fd) and positive side detector (Pd) were employed to detect the fast positively charged particles ejected in the forward directions. Two silicon tracking telescopes (STTs) were placed close to the target to detect the slow particles emitted at large angles. In order to access the kinematic regions of interest, both the ANKE settings and the STT positions were optimized by monte carlo simulations using the Geant package [113] prior to the experiment. The D2 magnetic field was set to be 0.48488 Tesla, and accordingly the deflection

---

[1]e stands for the proton charge, and R is the BCT impedance.

angle was $\alpha = 8.2°$ (see Eq. 3.1). The acceptance of the detection systems Fd, Pd and STT are plotted in Fig. 4.2 in terms of the rigidity and the projection of the scattering angle in the xz-plane. Kinematical loci of the charged particles from the processes of interest are plotted as well.
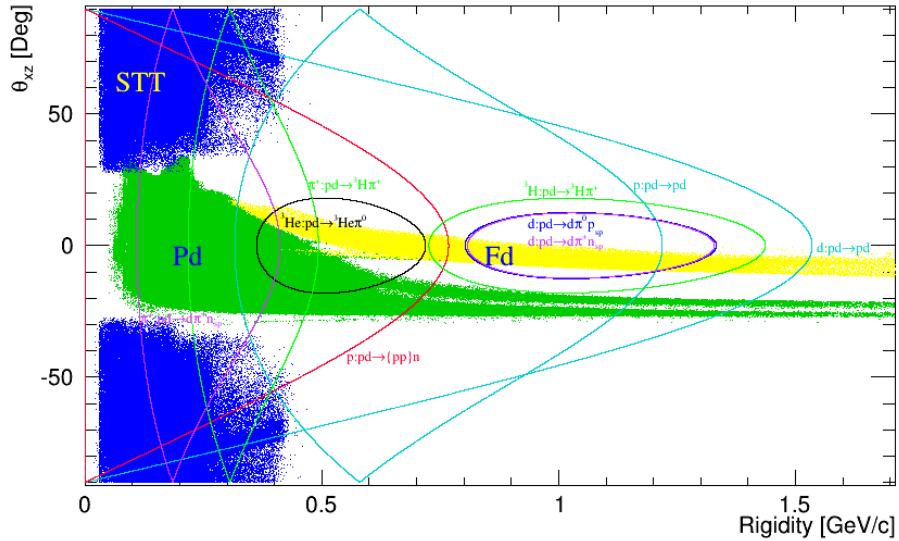
Figure 4.2: Acceptances of the ANKE sub-detection systems Fd, Pd and STT, indicated in different colors. The scatter data are from the experiment. The loci of the particles are simulated with the PLUTO [112].

Mainly three triggers were used in present experiment. The first one (Tr1) was triggered by particles passing through two adjacent counters in the first and second layers of the forward hodoscope. The second trigger (Tr2) was set two select heavy particles (such as ${}^3He$) according the the energy deposit in the forward counters. The third trigger (Tr3) was generated by particles transversing either of the left and right silicon tracking telescopes (STTs). Any of the three triggers mentioned above would trigger the ANKE DAQ process, through which the signals from all the sub detection systems of ANKE would be digitalized and stored. Each data readout process took about 100 μs, during which any other triggered events could not be written. in order to analyze DAQ efficiency in the offline data analyses, all the trigger signals were recorded in a scaler. A periodical trigger (Tr4) was triggered every 100 ms to readout the scaler.

The target used in the experiment are listed in Table 4.1. Four modes of the polarized deuterium target[2] were employed in the experiment. The state 1

---

[2]Modes 4, 5 and 10, 11 in Table 3.3, in this chapter they are referred as state 1, 2 and 3, 4 respectively.
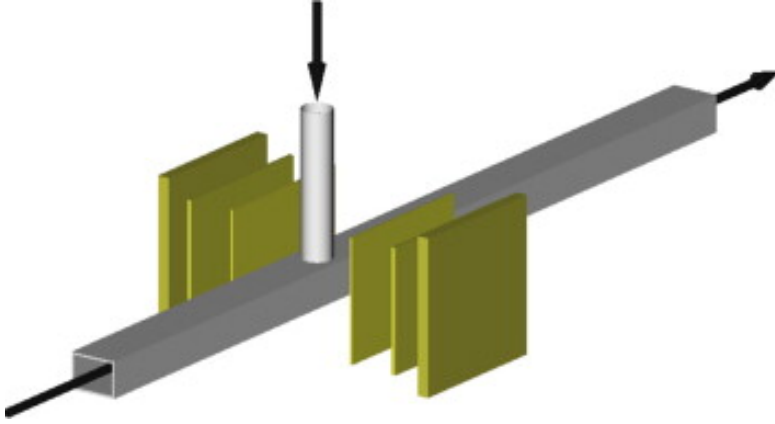
Figure 4.3: Schematic view of the ANKE target area showing the positions of the polarized deuterium cell target and its feeding tube and the two Silicon Tracking Telescopes (STT). The COSY beam direction is indicated by the long horizontal arrow.

and 2 were grouped as one pair, target were switched between them every 10 sec. The rf transitions which are exploited to produce state 1 are MFT $(3 \rightarrow 4)$ and WFT $(1 \rightarrow 4, 2 \rightarrow 3)$, and those used for state 2 are MFT $(3 \rightarrow 4)$ and SFT $(2 \rightarrow 6)$. Thus the switch between is realized by alternating the transitions WFT $(1 \rightarrow 4, 2 \rightarrow 3)$ and SFT $(2 \rightarrow 6)$. Parameters of other components of the ABS, such as the dissociator (3.3.1.2) and the sextupoles (3.3.1.2) remain unchanged. The transitions units only transit the spin state and does not affect the intensity of the atomic beam, therefore the target thicknesses of states 1 and 2 are identical. The same is true for states 3 and 4. The target thickness of the free atomic jet from the ABS is roughly $n_{ABS} = 2 \times 10^{11} \ cm^{-2}$ (see 3.3.2), which would provide a luminosity of $L_{ABS} = fN \cdot n_{ABS} = 1294.55 \times 10^3 \ s^{-1} \cdot 8 \times 10^9 \cdot 2 \times 10^{11} \ cm^{-2} \approx 2 \times 10^{29} \ cm^{-2}s^{-1}$ under the conditions of present experiment. Such a small luminosity is unacceptable. In this experiment the target thickness was increased by 2 orders of magnitudes by using a storage cell (Fig. 4.3). Thus the luminosity was about $2 \times 10^{31} \ cm^{-2}s^{-1}$ with polarized targets. Data were also taken with unpolarized deuterium gas filled in the storage cell, so that comparison could be performed between the polarized and unpolarized data. The unpolarized deuterium was provided a unpolarized gas supply system, its density was was set to be 2 time of the ABS density. The major background in this experiment was caused by the interaction between the beam halo and storage cell. The shape of this background can be imitated by the beam interaction with nitrogen [114]. Therefore nitrogen target was also used in the experiment. During the cryopump regeneration [85] of the ABS, data was collected with empty cell.

Deuterium Targets		
	Q_y	Q_{yy}
Polarized State 1	+1	+1
Polarized State 2	-1	+1
Polarized State 3	0	-2
Polarized State 4	0	+1
Unpolarized State	0	0
Nitrogen		
Empty Cell		

Table 4.1: The targets used in the commissioning experiments. Two pairs of the polarized deuterium targets ((1, 2) and (3, 4)) were used. In order to minimize the systematic error the polarization states in the same pair alternated between each other every 10 sec during the experiment. Unpolarized deuterium data are used to be compared with the polarized data. The nitrogen and empty target were used for the purpose of background subtraction.

4.2 Target Polarimetry

In section 3.3.3 the polarimetry with the Lamb-shift polarimeter has been discussed in details. With the Lamb-shift polarimeter, a quick measurement of the target polarization with an absolute precision better than 1% can be achieved [87]. However, the polarization of the ABS jet does not equal to the polarization of the gas in the storage cell which actually collides with the COSY beam because of following reasons:

- The holding field in the storage cell provided by the D2 magnet decreases as the distance to the D2 magnet increases [115] thus the target palatalization varies along the storage cell.

- The collisions between the deuterium atoms and the wall of the storage cell and the atom recombination to molecules reduce the target polarization [19].

Therefore the Lamb-shift polarimeter is usually not adopted to measure the target polarization during experiment, instead, it is used to optimize the settings of ABS before experiment and to monitor the stability of the ABS. So a polarimetry which is able to measure the polarizations of the target in storage cell is indispensable. In what follows, the general principle of the polarimetry with nuclear reactions which meets the preceding requirement is given.

General principle of polarimetry with nuclear reaction

From the view of experiment, the most characteristic feature that distinguishes the experiments using polarized reactants from those using unpolarized

reactants is the azimuthal asymmetry of the distributions of the particles emitted from the nuclear reaction[3], which is a function of both the analyzing powers that connect with the dynamics and the polarizations of the beam or/and target. Therefore, one can in principle extract the polarizations from the azimuthal asymmetry (if it is measurable) provided that the analyzing powers of this reaction are known. The analyzing powers of the nuclear reactions used for polarimetry are required to be large enough, otherwise the azimuthal asymmetry will be distorted by the systematic errors. In addition, sufficiently large cross sections are also expected so that enough events can be accumulated for polarization measurement. Practically it is however not always the case that one could find some nuclear reactions which simultaneously fulfill all the above requirements at the exact energies where the experiments is to be performed. In order to overcome this difficulty, a method called export technique has been invented and successfully applied in previous experiments at ANKE [58]. The central idea of this technique is to conduct the production measurements at the energies of interest in between two polarimetry measurements which are performed at the energy where reliable polarimetry exists. If the polarizations were measured to be identical before and after the production measurements, conclusion can be made that the polarizations during the production measurements are the same with those measured at the polarimetry energy. It is worthwhile to note here, that in the case where polarized beam is used [58] special care has to be taken to avoid any possible depolarization [116] during the beam energy ramps between polarimetry energy and production energies. Although the polarization export technique was necessary in this experiment, it has to be exploit in the future production experiment [117].

To summarize, the polarizations of beam/target are measured by using the nuclear reactions with large and well known analyzing powers, which can be registered by the detectors with sufficient statistics. Polarimetry at the polarimetry energy is extended to other energy by the export technique.

4.2.1 Polarimetry with $p\vec{d} \rightarrow pd$

From the plot of acceptance (see Fig. 4.2) it can be seen that the deuterons emitted at small polar angles from the deuteron-proton elastic reaction $pd \rightarrow pd$ mainly fall into the silicon tracking telescopes (STTs). In addition the vector (A_y) and tensor (A_{xx}, A_{yy}) analyzing powers of $p\vec{d} \rightarrow pd$ have been measured by Argonne[118], Sature[119, 120] and ANKE[57] in the vicinity of 600 MeV, which

---

[3]Hereafter we shall call it azimuthal asymmetry for brevity

agree with each other quit well. Besides, the elastic process $pd \to pd$ has considerably large cross section in comparison to other processes, which may contribute to the background, therefore the background hardly affect the measurement. Due to above reasons the deuteron-proton elastic scattering $pd \to pd$ is very suitable to be used as the reference reaction for the dueteron target polarimetry. During the data analysis different methods were tried to measure the target polarization. In the following we shall first introduce the general analysis procedure of the STT data in section 4.2.1.1, and then discuss the analyzing powers of $p\vec{d} \to pd$ and the STT acceptance in section 4.2.1.1, finally in sections 4.2.1.2 and 4.2.1.3 present the procedures for extracting the target polarizations for $pd \to pd$ with and without the upolarized data respectively.

4.2.1.1 General Procedure of STT Data Analysis

The four-momentum reconstruction is a crucial step of the experimental data analysis. For the STT detection system the four-momentum reconstruction generally consists of two parts, i.e. the track reconstruction and the energy measurement, which will be discussed in the following. The STT is composed of double-layer silicon-strip detectors, therefore every event contains some three-dimensional coordinates with certain errors, i.e. $(x \pm \delta x, y \pm \delta y, z \pm \delta z)$. Some of these coordinates are the position where the emitted particles interacted with the detector, while others are produced by the cosmic rays or by the intrinsic noise of the detector itself. To reconstruct real tracks out of a bunch of special coordinates, the first step is to list all the possible straight lines that defined by the combinations of the coordinates in the first and second layers. Then these lines are checked one by one to see if they pass through the storage cell (CS). If one line passes through the storage cell it is regarded as a real track, and all the other lines that contain the associated coordinates are excluded from the list. This procedure continues until there are no more straight lines on the list. The search of the hits in the third layer are performed via scanning the region within a certain solid angle around the selected the straight lines. For those events with two (or more) tracks their vertices can be reconstructed using the method described below. First, based on all the points that located at the selected tracks a plane is built through linear iteration. For the elastic process the plane is further required to be parallel to the beam axis. This plane is regarded as the one which the true tracks locate in. Projecting all the points on the reconstructed tracks into this plane, new tracks will be formed, the cross of the new tracks is the reconstructed vertex. Furthermore

the sum of the squared distances of all the selected points to the plane can be used to evaluate the quality of the track and vertex reconstructions quantitatively. The kinetic energy of the particles are measured as the sum of the energy deposit in each layers, which in turn are obtained by multiplying the QDC signals with the pre-determined energy-calibration factors. In STT the energy deposit in quantitatively silicon micro strip detectors can be used for particle identification (PID). For a charged particle of low energy ($\beta \ll 1$), its energy loss per unit thickness in material is given by the simplified Bethe-Bloch formula

$$-\frac{dE}{dx} = \frac{4\pi n z^2}{m_e v^2} \cdot \left(\frac{e^2}{4\pi\varepsilon_0}\right)^2 \cdot \ln\left(\frac{2m_e v^2}{I}\right), \tag{4.1}$$

where m_e is the electron mass, ε_0 is the vacuum permittivity, n and I are the electron density and mean ionization energy of the material, z 和 v are the charge and the velocity of the particle. Consider a case with a charge particle and two silicon micro-strip detectors. If the energy of the particle is too small it will be stopped in the first detector. Now image that its energy increases gradually. At some point it will be sufficiently energetic to pass the first detector and reach the second one. With the energy increase, the energy deposit in the first detector will decrease according to the Bethe-Bloch formula 4.1, while in the second detector the energy loss increases due the increase thickness. This process goes on until the particle pass through the second detector. Then the energy loss in the second detector decrease as well due to the same reason as in the first detector. From above discussion it can be seen that for the particles that pass through the first detector their energy losses in the first detector decrease as the increase of their kinetic energies, whereas in the second detector their energy losses increase first and then decrease. Therefore on the scattering plot of the energy losses in the first and second detectors particles are distributed in two connected bands, corresponding respectively to those deposited in and passing through the second detector. As an example Fig. 4.4(a) shows a scattering plot of the energy losses of the first and second layers of the STT, the upper and lower bands with downward trends represent respectively the deuterons and protons deposited in the second layer.

Consider two particles of different masses with the same electric charge. Suppose they lost the same energy in the first detector, then it means their (effective) velocities before entering the first detector are identical and thus the heavier one has higher energy. After losing the same amount of energy in the first detector the heavier particle still has higher energy, therefore the heavier one will deposit

more energy in the second detector if both particles are stopped in the second detector. On the other hand, in the case where the particles pass through the second detector the energy losses depend on their velocities. Since the heavier particles loss smaller velocity in the first detector, it has higher velocity in the second detector, thus it losses less energy. This is exactly the principle how the particles are identified using the energy deposit. Form Fig. 4.4(a) it can be seen that the particles stopped in the second layer can be well distinguished, however the particles passing through the second layer are hard to separate since they are overlapped with each other. Fortunately these particles pass through the detector and their energy can not be measured, therefore we don't need to identify them. However there are some particles that passed through the second detector mixing with some stopped particles. It is better to selected these stopped particles. By
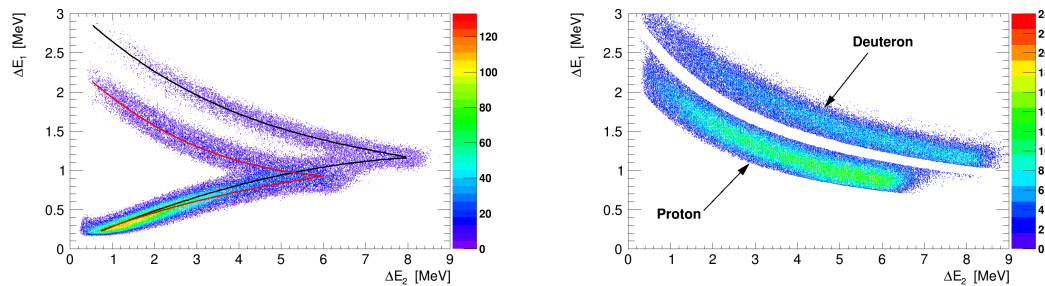
Figure 4.4: The particles in the STTs are identified by the $\Delta E/E$ method. Here ΔE_1 and ΔE_2 denote the energy deposit in the first and second layers of the silicon micro-strip detectors in the STTs. In the left panel, the two regions indicated with black and red lines represent deuterons and protons respectively. It is hard to select the protons around the knee point since they are mixed with the passing-through deuterons. The artificial network technique [121] is found to be effective to identify these protons at the knee point (see the right panel).

the method of artificial network it is possible to judge if a particle in the overlap region stopped in the second layer or not [121]. Fig. 4.4 shows the events after the filtering of the artificial network, it can be seen that the passing-through particles in the overlap region are filtered effectively.

Acceptance of STT and Analyzing Powers of $p\vec{d} \to pd$

In last subsection we discussed the method of particle identification (PID) in STT, it shows that particles of different species can be well distinguished by comparing their energy deposit in different layers of silicon micro-strip detector. It can be seen from the acceptance plot (Fig. 4.2) that only the scattered deuterons from the proton-deuteron elastic scattering reaction can be detected by STT,

the protons are beyond the coverage of STT. One therefore only needs to select deuterons in the single-track events. Fig. 4.4 is a scattering plot of the energy deposit in the second the upper bands correspond to the deuterons stopped in the third layer. By the same method the deuterons stopped in the second layer can be also selected. Using the four-momenta of the proton beam and of the selected deuterons, the missing-mass spectrum of process $pd \to dX$ was built (see Fig. 4.5). As shown, most events are located within $\pm 5\sigma$ of the proton invariant mass. Since the cross section of the elastic reaction are extremely large compare to other processes, the background signal generated by the collision between the beam halo and and the wall of the storage cell are negligibly weak (see the shadow area) thus has little influence on the measurement. Nevertheless those background are subtracted during the data analysis. The bump close to 1.2 GeV corresponds to the pion production. The deuteron-proton elastic reaction $pd \to pd$ is a two-body
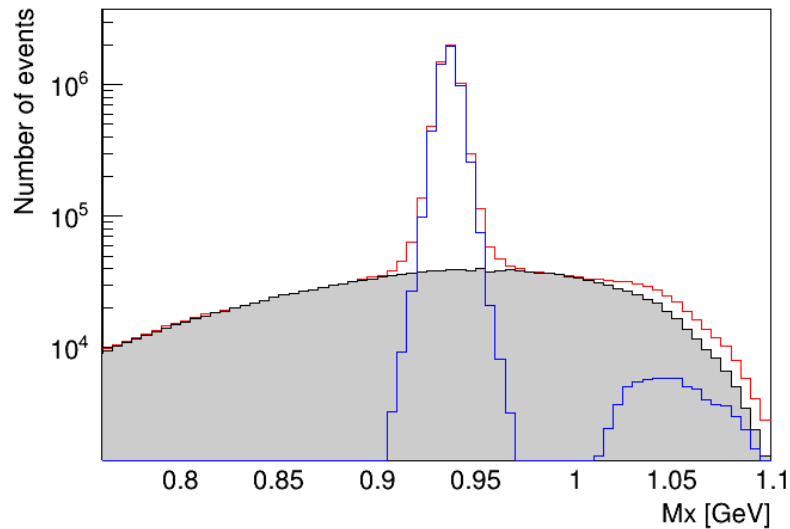
Figure 4.5: The $pd \to dX$ missing mass spectrum of the STT data. The red histogram represents the data of the deuteron target; the background drawn in grey is the nitrogen data scaled by a factor, which is determined by the fitting beyond the peak region; the blue histogram is the distribution after the background subtraction. The peak at the neutron mass represents the d-p elastic scattering events, the peak around 1.05 MeV corresponds to the π production.

process, there exists one-to-one relation between the energies and the scattering angles of the ejected particles. It is therefore possible to derive the scattering angle based on the measured energy, which can be measured with very small uncertainty in the STT. It was found out that the angular resolution obtained by energy derivation is much higher than that from direct measurement, therefore the former is used in the subsequent analysis. The plot in Fig. 4.6 shows the distribution of
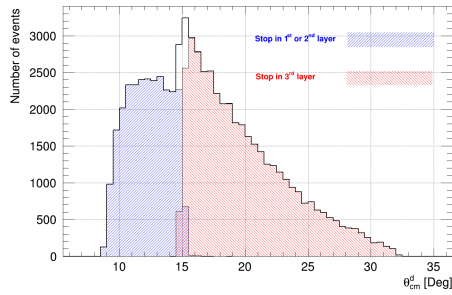
Figure 4.6: The distribution of $pd \rightarrow pd$ as a function of the deuteron polar angle in CM system.
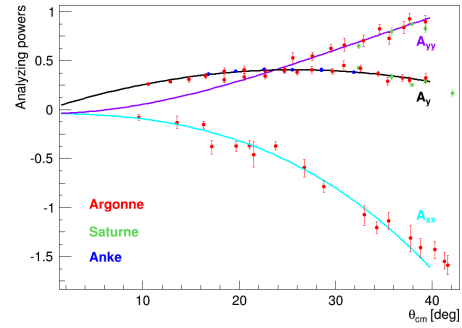
Figure 4.7: Measured analyzing powers (A_y, A_{yy} and A_{xx}) of $p\vec{d} \rightarrow pd$ as a function of the deuteron polar angle in CM system.

the $pd \rightarrow pd$ events as a function of the scattering angle of the recoiled deuteron in the center-of-mass (CM) reference. On can see that the deuterons scattered at large angles ($\theta_{cm}^d > 15°$) had higher energies thus were stopped in the third layer, whereas those scattered at small angles were less energetic and were stopped in the second layer. The data plotted in Fig. 4.7 are the vector (A_y) and tensor (A_{yy}, A_{xx}) analyzing powers of the reaction $p\vec{d} \rightarrow pd$ measured in the vicinity of the proton injection energy $T_p = 600$ MeV. These data were measured at $T_d = 1194$ MeV by Argonne[118], at $T_d = 1198$ MeV by SATURNE[119, 120], at $T_d = 1170$ MeV by ANKE [57]. All these measurements were conducted by bombarding polarized deuteron beam at hydrogen target, so the data from Argonne, SATURNE and ANKE correspond respectively to the proton injection energies of $T_p = 597$ MeV, $T_p = 599$ MeV and $T_p = 585$ MeV. From Fig. 4.7 one sees that the data from different experiments agree with each other within the errors, which means the analyzing powers do not vary too much with respect to energy and these data are reliable. Therefore these data can be used for the deuteron target polarimetry at $T_p = 600$ MeV. For convenience all the three analyzing powers are fitted by polynomials. The polynomials are chosen in such a manner that they can describe the data but will not include the systematic errors of those data. The adopted polynomials are

$$A_y(\theta) = a_1\theta + a_2\theta^2, \tag{4.2a}$$

$$A_{yy}(\theta) = -0.04 + b_2\theta^2 + b_3\theta^3, \tag{4.2b}$$

$$A_{xx}(\theta) = -0.04 + c_2\theta^2 + c_3\theta^3. \tag{4.2c}$$

The constant term of $A_y(\theta)$ is fixed to be zero according to its definition, while the $A_{yy}(0)$ and $A_{xx}(0)$ are set as -0.04, which is taken from measurement [118]. As a result only two parameters are free in each of the fitting procedures. In Fig. 4.7 the fit functions of the analyzing powers A_y, A_{yy} and A_{xx} are indicated by black, purple and caeruleus respectively.

4.2.1.2 Method 1: Measurement with Unpolarized Data

Generally speaking, the polarizations of target/beam are in principle extracted from the azimuthal asymmetries, which, in practice can be either the difference between the distributions of the polarized and unpolarized data at the same azimuthal angle(s), or the difference between the distributions of the polarized data at different azimuthal angle(s), e.g. the left-right asymmetry which corresponds two different azimuthal angles: 0° and 180°. The method utilizing asymmetry between different azimuthal angles requires that the azimuthal angles at different regions (at least two regions) have to be covered experimentally. On the contrary, the method which makes use of the asymmetry between the different target/beam states is more flexible and can even apply to an single-armed detector. At this point, one would think that the method which compares polarized and unpolarized data is better because it does not require a double-armed detector, which is more expensive. However, if we look at the other side of the coin, the previous conclusion would become not that reliable: one has to first determine the ratio of the integrated luminosity of the polarized state to that of the unpolarzied state[4] in order to use the first method. On the other hand the problem of luminosity ratio does not arise at all if one uses the second method, but the systematic error which comes from the efficiency difference of the detectors at different azimuthal angles has to be considered instead. Now we see both of the methodologies mentioned above have advantages and disadvantages of their own，one needs to find out the best solution according to the experiment situation.

For the particular case which we are considering right now, i.e., to measure both the vector and tensor analyzing powers by using the elastic reaction $p\vec{d} \rightarrow pd$, the left and right STTs are used as a two-armed polarimeter, meanwhile the unpolarized target is also employed for the investigation, which suggests that we could combine those two methods discussed in last paragraph to exploit both

---

[4]In what follows, we call it luminosity ratio.

of their advantages and overcome their difficulties. For this purpose, a quantity named cross ratio is defined. In what follows, the detailed procedure of how to configure the cross ratio is discussed.

The cross section of a two-body single-polarized reaction with a spin-1 particle polarized in the initial channel is given in subsection 1.3.2.2 by Eq. 1.55. In the case of present experiment, where the polarization quantization axis is aligned perpendicular to the COSY plane, the polar angle β of the quantization axis in the projectile helicity system is $\frac{\pi}{2}$ (refer Fig. 1.2), thus the cross section reduces to[5]

$$\frac{d\sigma}{d\Omega}^{P}(\theta,\phi) = \frac{d\sigma}{d\Omega}^{0}(\theta)\{1 + \frac{3}{2}Q_y A_y(\theta)\cos\phi$$
$$+ \frac{1}{4}Q_{yy}[A_{yy}(\theta)(1+\cos 2\phi) + A_{xx}(\theta)(1-\cos 2\phi)]\} \quad (4.3)$$

where $\frac{d\sigma}{d\Omega}^{0}(\theta)$ is the unpolarized differential cross section, $A_y(\theta)$, $A_{yy}(\theta)$ and A_{xx} are the analyzing powers. Through observation, one would find that in Eq. 4.3 the second term $\frac{3}{2}Q_y A_y(\theta)\cos\phi$ is actually the asymmetry associated with the vector polarization Q_y, and similarly the third term $\frac{1}{4}Q_{yy}[A_{yy}(\theta)(1+\cos 2\phi) + A_{xx}(\theta)(1-\cos 2\phi)]$ is the asymmetry associated with the tensor polarization Q_{yy}. Hereafter we shall note them by A_V and A_T respectively to simplify the procedure of derivation, namely

$$A_V(\theta,\phi) = \frac{3}{2}Q_y A_y(\theta)\cos\phi \qquad (4.4a)$$

$$A_T(\theta,\phi) = \frac{1}{4}Q_{yy}[A_{yy}(\theta)(1+\cos 2\phi) + A_{xx}(\theta)(1-\cos 2\phi)] \qquad (4.4b)$$

Furthermore we shall also give the notations for event number and integrated luminosity, as well as for detector efficiency here in advance, which will be frequently used afterwards,

1. $N_{L/R}^{P/0}(\theta)$: Number of the events registered in the left/right STT with polarized/unpolarized target.

2. $L^{P/0}$: Integrated luminosity with polarized/unpolarized target.

---

[5]Actually the cross section Eq. 4.3 is derived in the polarization system. In the present case the laboratory system and the c.m. system are aligned in the same sense with respect to the polarization system, therefore it also applies to the laboratory and c.m. systems

3. $\varepsilon_{L/R}^{P/0}(\theta)$: Detection efficiency of the left/right STT with polarized/unpolarized target.

The number of events registered in a particular STT with a specific target state can be expressed in terms of cross section, integrated luminosity and detection efficiency. Take the number of events registered in the left STT with a polarized target P $(Q_y\ Q_{yy})$ as an example, it can be expressed in term of the notations declared previously as

$$N_L^P(\theta, \phi) = \frac{d\sigma}{d\Omega}^0(\theta)[1 + A_V(\theta, \phi) + A_T(\theta, \phi)]L^P \varepsilon_L^P(\theta, \phi) \tag{4.5}$$

For a given polarized state P $(Q_y\ Q_{yy})$, the cross ratio $CR(\theta)$, which is a function of both the scattering angle θ and azimuthal angle ϕ, is defined as[6]

$$CR = \frac{N_L^P N_R^0 - N_R^P N_L^0}{N_L^P N_R^0 + N_R^P N_L^0} \tag{4.6}$$

To examine all the sources that contribute the cross ratio, we expend the cross ratio in terms of cross section, integrated luminosity and detector efficiency by substituting the terms representing the numbers of events in Eq. 4.6 with their specific expressions that similar to Eq. 4.5, i.e.

$$CR = \frac{L^P \varepsilon_L^P (1 - A_V + A_T) L^0 \varepsilon_R^0 - L^P \varepsilon_R^P (1 + A_V + A_T) L^0 \varepsilon_L^0}{L^P \varepsilon_L^P (1 - A_V + A_T) L^0 \varepsilon_R^0 + L^P \varepsilon_R^P (1 + A_V + A_T) L^0 \varepsilon_L^0} \tag{4.7a}$$

$$= \frac{(\frac{\varepsilon_L^P}{\varepsilon_R^P}/\frac{\varepsilon_L^0}{\varepsilon_R^0})(1 - A_V + A_T) - (1 + A_V + A_T)}{(\frac{\varepsilon_L^P}{\varepsilon_R^P}/\frac{\varepsilon_L^0}{\varepsilon_R^0})(1 - A_V + A_T) + (1 + A_V + A_T)}. \tag{4.7b}$$

It can be further simplified as

$$CR = \frac{(1 - A_V + A_T) - (1 + A_V + A_T)}{(1 - A_V + A_T) + (1 + A_V + A_T)} = \frac{-A_V}{1 + A_T} \tag{4.7c}$$

if $\frac{\varepsilon_L^P}{\varepsilon_R^P}/\frac{\varepsilon_L^0}{\varepsilon_R^0} = 1$, which is equivalent to say that the ratio of the detection efficiencies between the left and right STT $\frac{\varepsilon_L}{\varepsilon_R}$ kept unchanged for the measurements with polarized and unpolarized targets. Since the detection efficiency is entangled with the polarization effects, there is no way to directly check if the efficiency ratio $\frac{\varepsilon_L}{\varepsilon_R}$

---

[6]To shorten the formulae, either θ or ϕ are not written specifically, the reader should recognize by context.

was identical or not for the polarized and unpolarized data-taking. On the other side, one can check if $\frac{\varepsilon_L}{\varepsilon_R}$ changed between the unpolarized data-taking and the nitrogen data-taking. Fig. 4.8 shows the ratio of left-right counting ratio between between the unpolarized deuterium data and the nitrogen data $\frac{N_L^0}{N_R^0} / \frac{N_L^{N_2}}{N_R^{N_2}}$, which is equivalent to $\frac{\varepsilon_L^0}{\varepsilon_R^0} / \frac{\varepsilon_L^{N_2}}{\varepsilon_R^{N_2}}$. It was found out that the over value of $\frac{\varepsilon_L^0}{\varepsilon_R^0} / \frac{\varepsilon_L^{N_2}}{\varepsilon_R^{N_2}}$ is rather close to 1. In the experiment the data-taking with unpolarized deuterium target and with nitrogen target were performed during different time, so it is convincing that the detection efficiency ratio also did not change when data were taken with the polarized target.
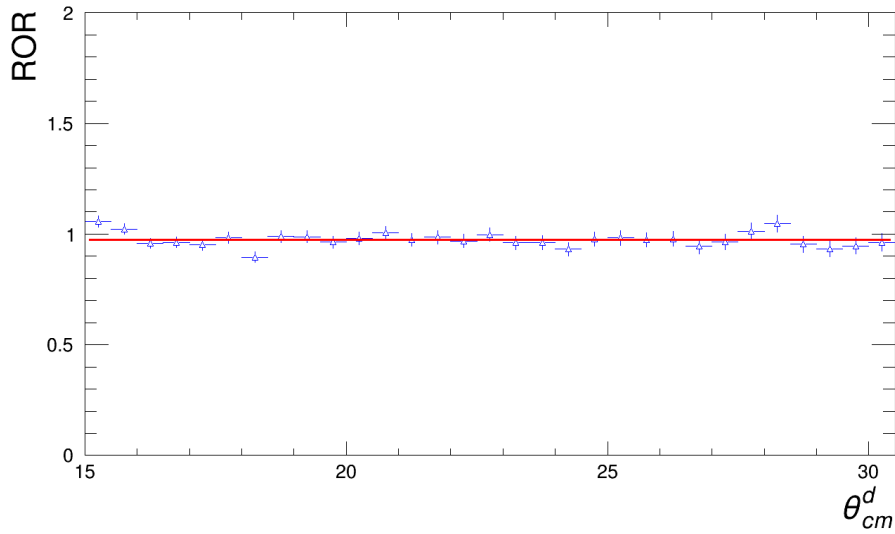
Figure 4.8: Ratio of left-right detection efficiency ratio between unpolarized deuterium and nitrogen data.

Take the expressions 4.4a and 4.4b back into 4.7c, we obtain

$$CR = \frac{-\frac{3}{2} Q_y A_y(\theta) \cos\phi}{1 + \frac{1}{4} Q_{yy} [A_{yy}(\theta)(1 + \cos 2\phi) + A_{xx}(\theta)(1 - \cos 2\phi)]} \quad (4.7\text{d})$$

Taking into account that the STTs were installed at the left and right sides with respect to the target, corresponding to the azimuthal angles close to 0° and 180° respectively, we immediately notice that the contribution $A_{xx}(\theta)(1 - \cos 2\phi)$ from the analyzing power A_{xx} is relatively small compared with the contributions from A_y and A_{yy} because of the smallness of $(1 - \cos 2\phi)$ at those regions. If the azimuthal angle is confined to such immediate vicinities of the azimuthal angles $\phi = 0°$ and $\phi = 180°$ where $\cos\phi \to 1$ and $\cos 2\phi \to 1$, the cross ratio (CR)

becomes a quite simple expression

$$CR \approx \frac{-\frac{3}{2}Q_y A_y(\theta)}{1 + \frac{1}{2}Q_{yy} A_{yy}(\theta)} \qquad \phi \to 0°, 180° \tag{4.8}$$

which depends on both the vector polarization (Q_y) and tensor polarization (Q_{yy}). Therefore it is possible to extract both vector polarization (Q_y) and tensor polarization (Q_{yy}) of the deuterium target simultaneously through fitting the measured quantity cross ratio (CR) (Eq. 4.6) with Formula 4.8.

(a) State 1

(b) State 2

(c) State 3

(d) State 4
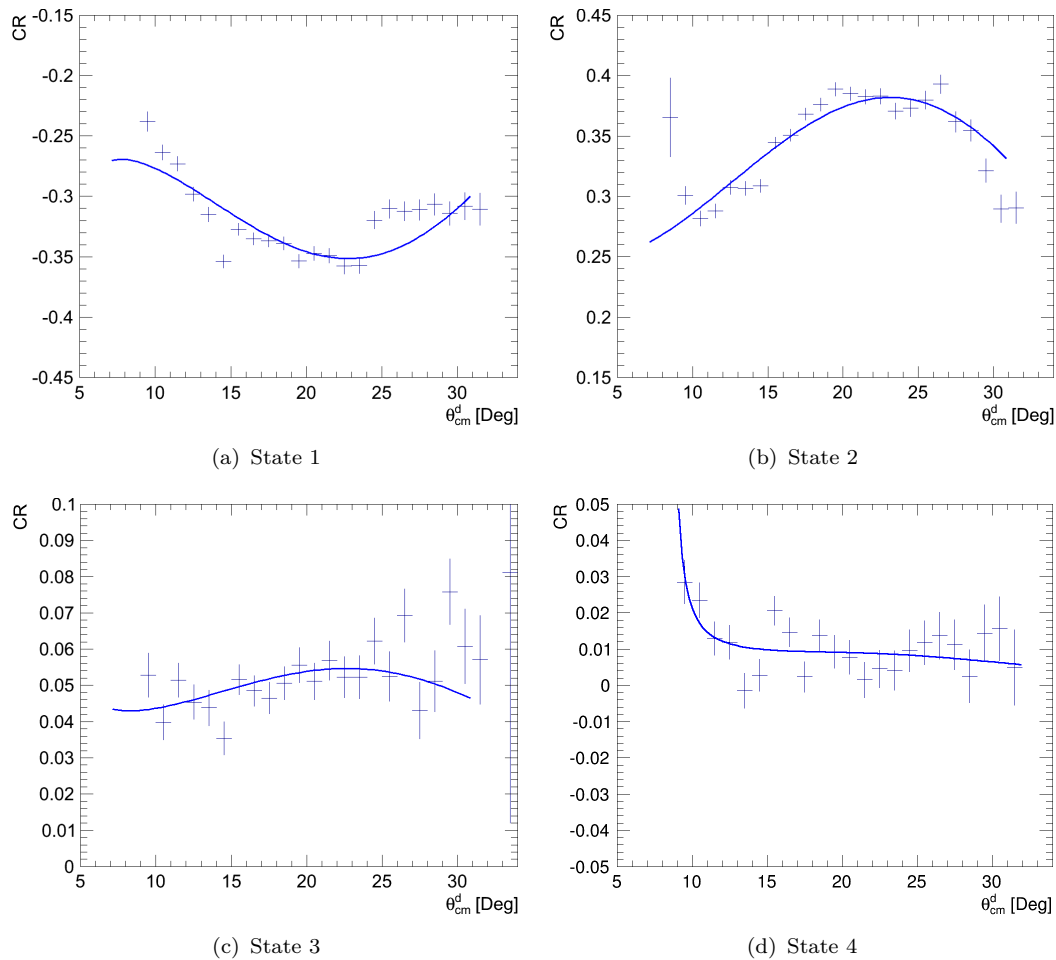
Figure 4.9: Cross ratio (CR) as a function of deuteron scattering angle for all the four states. To extract vector (Q_y) and tensor (Q_{yy}) polarizations, data points are fitted by Formula 4.8

The measured cross ratio is depicted in Fig. 4.9 as a function of deuteron scattering angle in the c.m. reference system for all the polarized target modes used in the commissioning experiment. For each mode the cross ratio is fitted by Eq. 4.8. The polarizations (Q_y and Q_{yy}) of the state 1 (+1, +1) and state 2 (-1, +1)

were measured to be Q_y^1=0.689±0.006, Q_{yy}^1=0.917±0.073 and Q_y^2=-0.730±0.006, Q_{yy}^2=0.673±0.063 respectively.

Fig. 4.9(c) and 4.9(d) demonstrate that the cross ratios of the mode 3 (0, -2) and 4 (0, +1) almost vanish, which means the vector polarizations of these modes are rather close to their ideal value ($Q_y = 0$). Due to the smallness of the cross-ratio signal, the polarization Q_{yy} of these modes can not be measured by fitting the cross ratio since the cross ratio is not sensitive to it in those cases. On the other hand, one would expect that the contribution of the vector polarization to the azimuthal asymmetry is small enough to be neglected, thus in this case it is possible to measure the tensor polarization (Q_{yy}) from the event ratio between of the polarized and unpolarized targets

$$\frac{N^P(\theta, \phi)}{N^0(\theta)} \approx R_{Lum.}[1 + \frac{1}{4}Q_{yy}A_{yy}(\theta)(1+ < \cos 2\phi >)] \qquad \phi \to 0°, 180°. \quad (4.9)$$

if the detection efficiencies in the polarized and unpolarized measurements are identical. Note that besides the tensor polarization which we are aiming to measure, the luminosity ratio ($R_{Lum} = \frac{Lum^P}{Lum^0}$) can also be determined simultaneously as a by-product. Above procedure can be applied either to the left-STT data or to the right-STT data. In principle one should get the same results in both cases if the detection efficiency does not change (too much) between the measurements with unpolarized and polarized targets. However the fitting results from left and right STT data were found to be inconsistent with each other, this means the detection efficiency did not keep invariant during the experiment. In next subsection a method which eliminates the influence of the instability will be presented.

4.2.1.3   Method 2: Polarization Measurement without Unpolarized Data

When data were taken with polarized target in this experiment the polarization modes in the same pair (refer Table 4.1) were switched between each other every 10 seconds. In such a short time scale, both the beam intensity and the detector efficiencies were stable. Moreover, the atomic beam source (ABS) provided identical gas densities for the polarization modes in the same pair. As a result both the luminosity and the detection efficiency were the same for the polarization modes in one pair. This was experimentally verified using background events that were free from polarisation effects. Such events were collected from the vicinity of the missing-mass peak corresponding to the elastic pd scattering. By evaluating

the ratio of the counts for two members of a polarisation pair, which is directly the product of relative efficiency times the relative luminosity between the two modes, it was shown that the relative efficiency is unity within 1.5%.

Thanks to the above facts, the effects caused by the instabilities of the beam and target as well as of the detectors will cancel out between the modes in the same pair. It is therefor advantageous to use only the polarized data in the same pair for the polarization measurement. For the convenience of the following discussion, we denote the the polarizarion modes in the same pair which switch between each other by a and b. The most important task is to construct a quantity which is sensitive to the polarizations. It was found out that the ratio between the sum and the difference of the event number of the modes a and b, namely

$$R = \frac{N_a - N_b}{N_a + N_b} \tag{4.10}$$

was the most suitable configuration. Inserting the expression of the event number

$$N_{a/b}(\theta, \phi) = \frac{d\sigma}{d\Omega}^P (\theta, \phi) \cdot L_{a/b} \cdot \varepsilon_{a/b}(\theta, \phi) \tag{4.11}$$

into Eq. 4.10 and making use of the formula of the polarized cross section Eq. 4.3, one obtain the expression for the quantity R, i.e.

$$r(\theta, \phi) = \frac{\frac{3}{2} A_y(\theta) \cos \phi (Q_y^a - Q_y^b) + \frac{1}{4}[A_{xx}(\theta)(1 - \cos 2\phi) + A_{yy}(\theta)(1 + \cos 2\phi)](Q_{yy}^a - Q_{yy}^b)}{2 + \frac{3}{2} A_y(\theta) \cos \phi (Q_y^a + Q_y^b) + \frac{1}{4}[A_{xx}(\theta)(1 - \cos 2\phi) + A_{yy}(\theta)(1 + \cos 2\phi)](Q_{yy}^a + Q_{yy}^b)} \tag{4.12}$$

In principle the target polarizations Q_y and Q_{yy} can be determined by fitting the observable R . Note both the luminosity and the detection efficiency are absent in the above formula. Thus neither of them produces systemic error in the measurement. Practice showed that data only from one single STT could not impose sufficient constraints to obtain the polarizations. In order to increase the sensitivity to the polarizations, the whole data set were exploit. Build the two-dimensional map $R(\theta, \phi)$ for the ratio Eq. 4.10, and fit it by the formula 4.12 simultaneously in both variables θ and ϕ, one can get the target polarizations Q_y and Q_{yy}. Fig. 4.10 and Fig. 4.11 illustrate the two-dimensional fit for the polarization pair (1, 2) and (3, 4) respectively. The blue points represent the measured ratio and the red meshes are the functions obtained by fitting. To show the the fitting quality intuitively, the measured data together with the fit function are also presented in
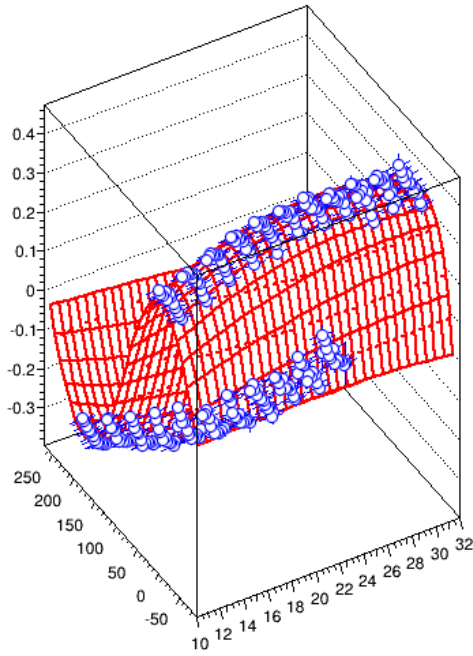
Figure 4.10: 2D fitting of R for states 1 and 2.
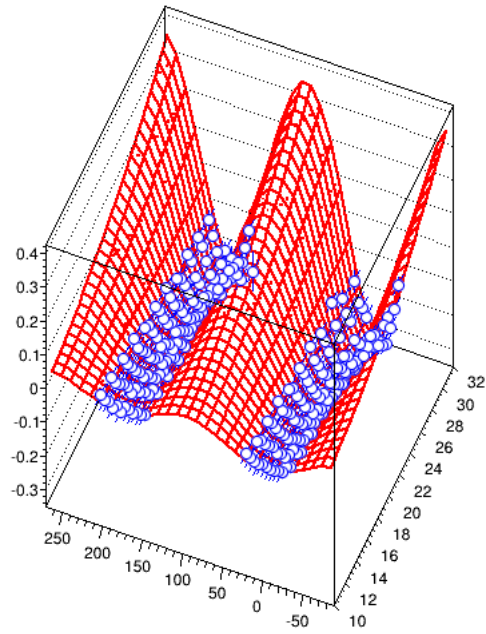
Figure 4.11: 2D fitting of R for states 3 and 4.

terms of one-dimensional plots. Fig. 4.12-4.13 and Fig. 4.14-4.15 are the R distributions in θ for pairs (1, 2) and (3, 4). The data of the left and the right STTs are plotted separately. The distribution in ϕ are presented in Fig. 4.16 and Fig. 4.17 for pairs (1, 2) and (3, 4) respectively.

The polarization values obtained through above procedure are ($Q_y^1 = 0.69 \pm 0.01$, $Q_{yy}^1 = 0.96 \pm 0.01$), ($Q_y^2 = -0.76 \pm 0.01$, $Q_{yy}^2 = 0.80 \pm 0.02$), ($Q_y^3 = -0.06 \pm 0.02$, $Q_{yy}^3 = -0.97 \pm 0.02$) and ($Q_y^4 = 0.01 \pm 0.03$, $Q_{yy}^4 = 0.69 \pm 0.25$). The errors given are statistical errors.

4.2.1.4 Systematic Error Estimation

In the approach introduced in subsection 4.2.1.3, the issue of instability is completely resolved by the comparison between the data of the polarization modes in the same combination, therefore the systematic error may only stem from the analyzing powers (A_y, A_{yy} and A_{xx}) of the reference reaction $p\vec{d} \rightarrow pd$. In other words the systematic errors in the polarization measurement can be estimated from the uncertainties of the analyzing powers which are inserting in the fit function Eq. 4.12. As discussed in subsection 4.2.1.1 the measured analyzing powers of the pd-elastic reaction used for the polarimetry are described by the polynomials Eq. 4.2. Therefore the uncertainties of A_y, A_{yy} and A_{xx} can be evaluated by varying
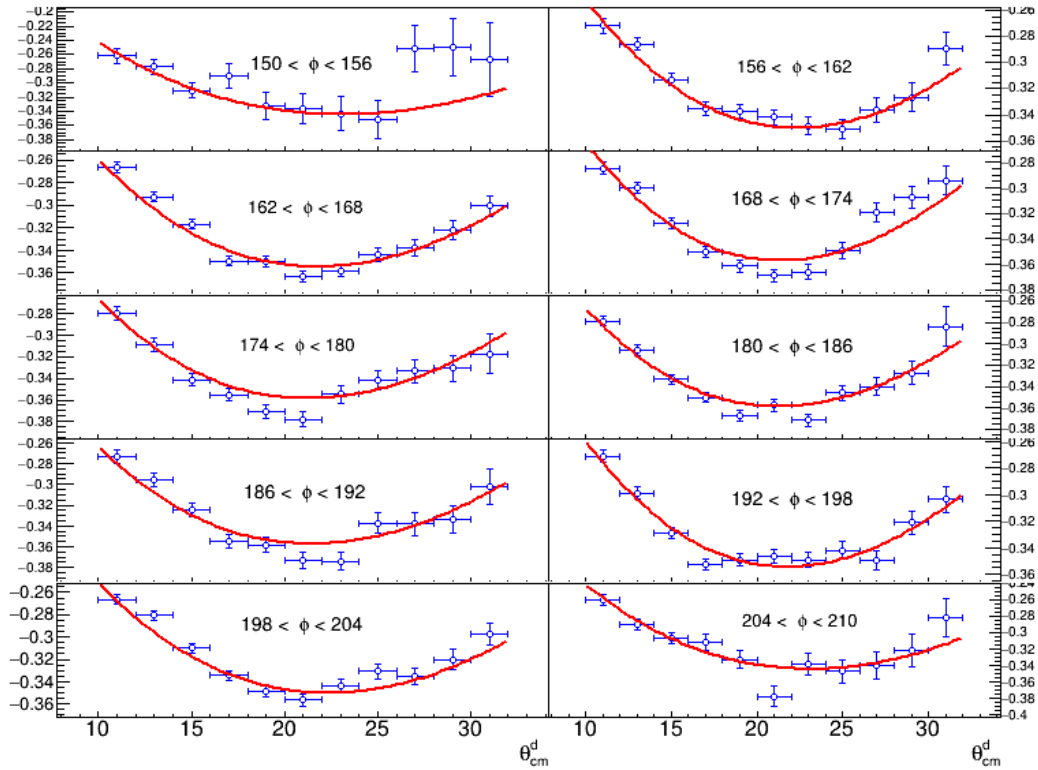
Figure 4.12: θ distribution of R for states 1 and 2, red curves are fit function.
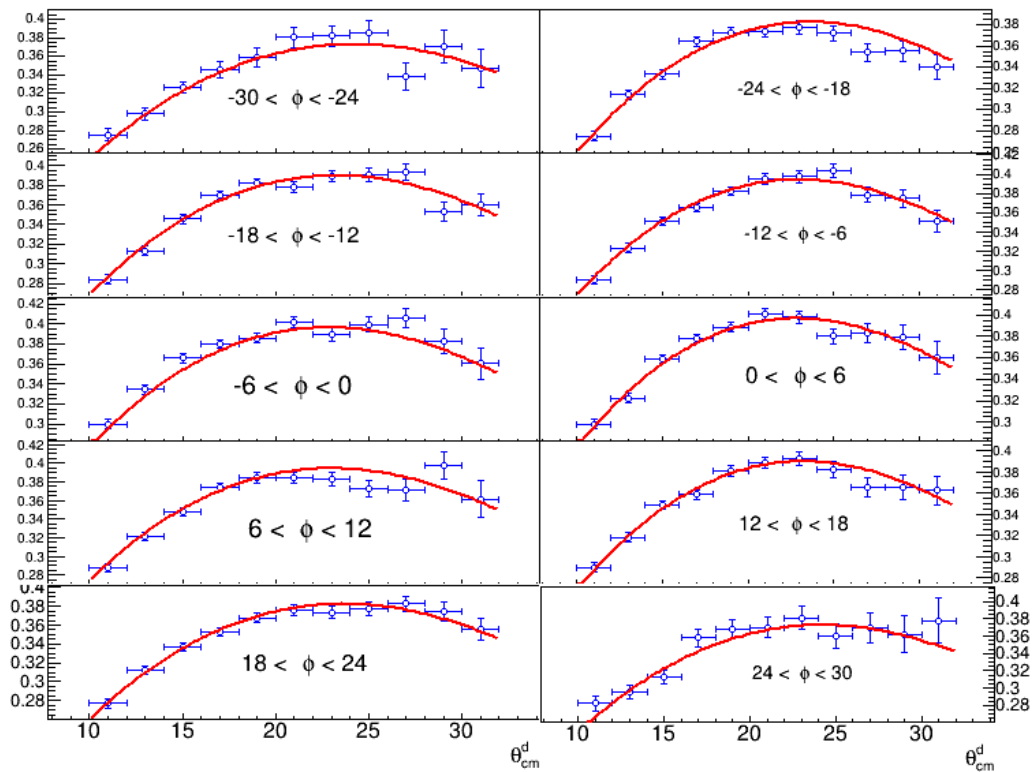
Figure 4.13: θ distribution of R for states 1 and 2, red curves are fit function.
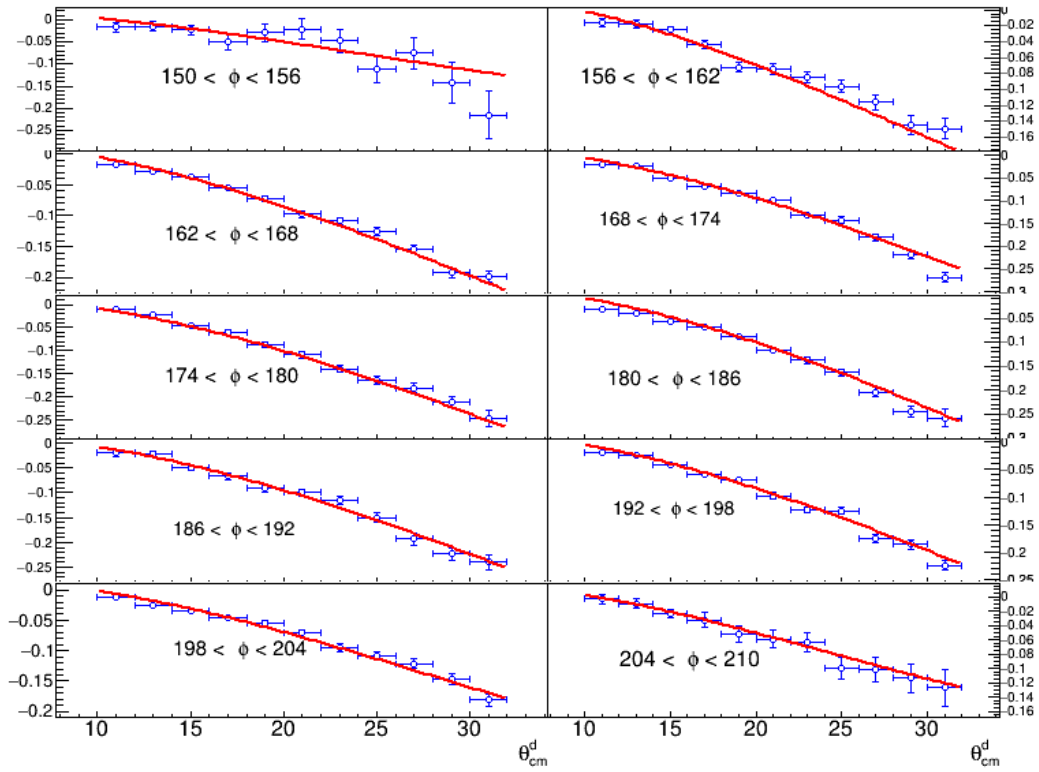
Figure 4.14: θ distribution of R for states 3 and 4, red curves are fit function.
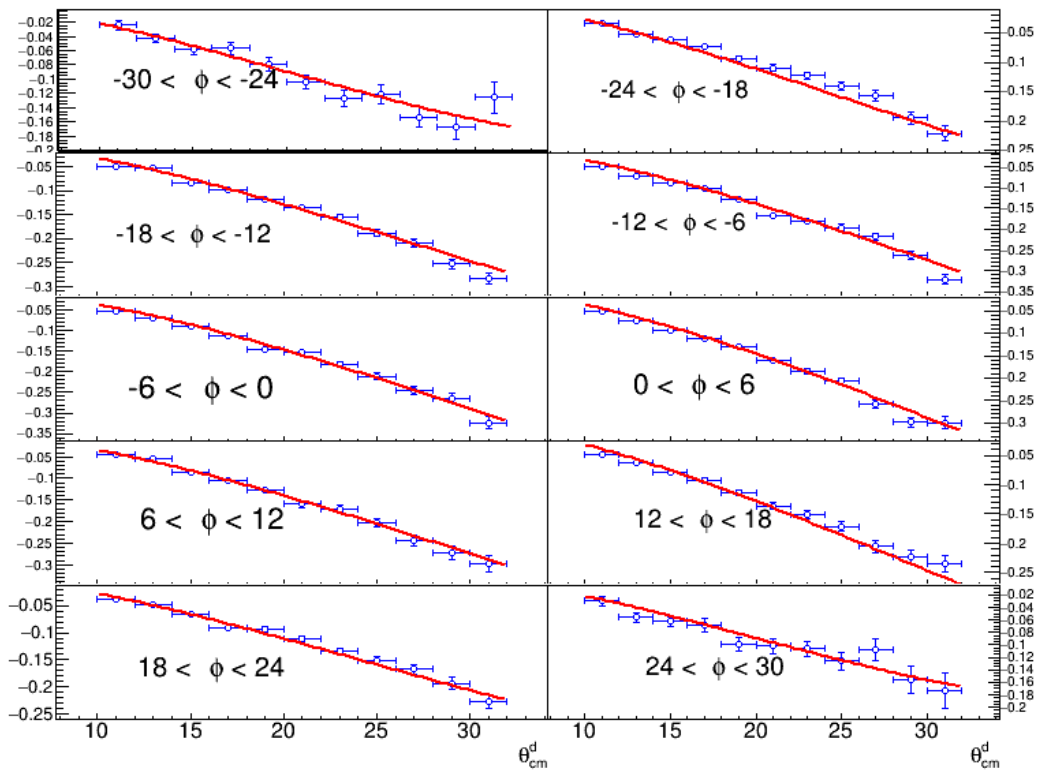
Figure 4.15: θ distribution of R for states 3 and 4, red curves are fit function.
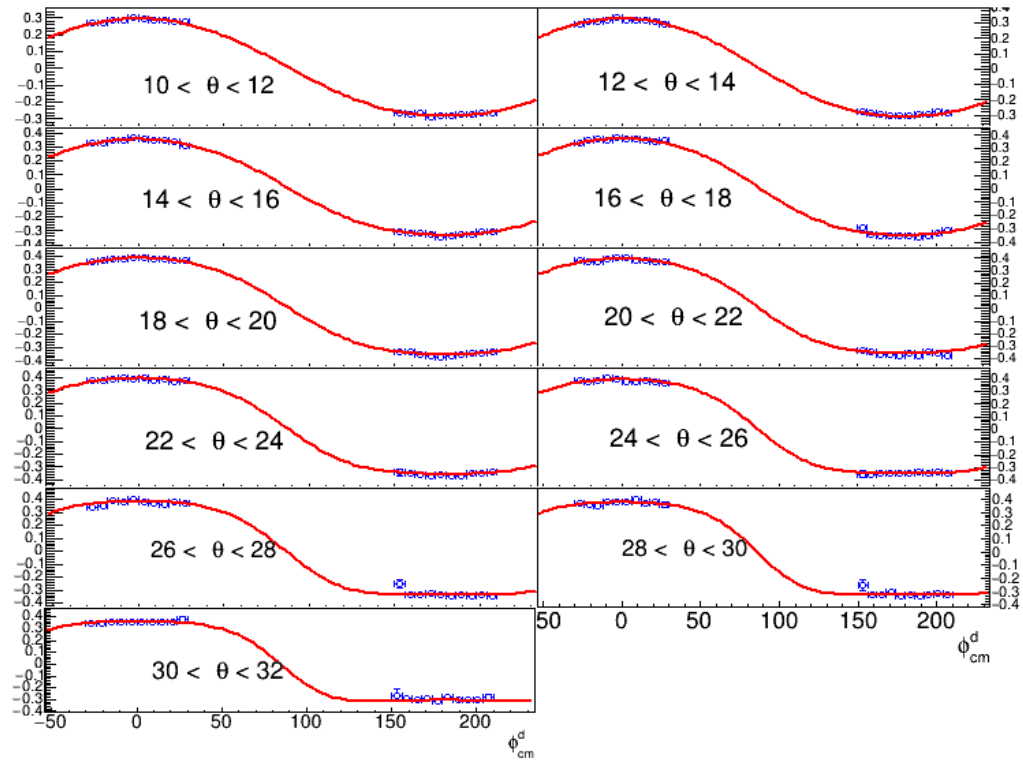
Figure 4.16: ϕ distribution of R for states 1 and 2, red curves are fit function.
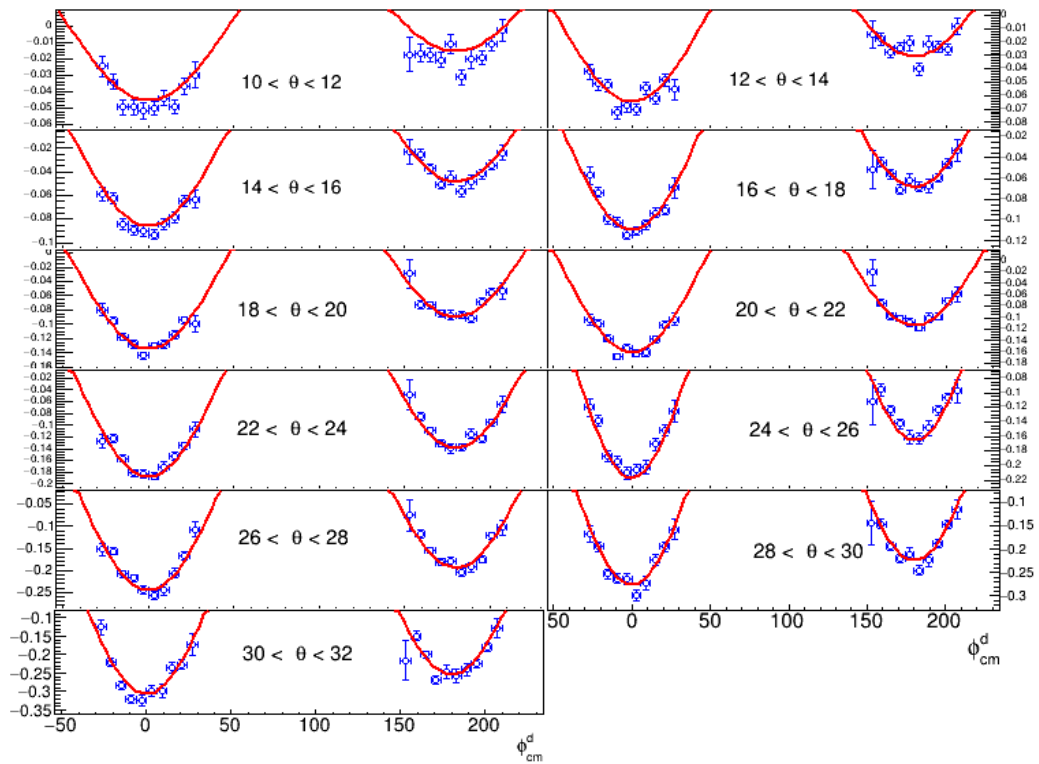
Figure 4.17: ϕ distribution of R for states 1 and 2, red curves are fit function.

the free parameters of those polynomials within their errors. The systematic errors of the measured polarizations can be in turn estimated by repeating the fitting of the ration R (Eq.4.10) with those new polynomials as input. This procedure is
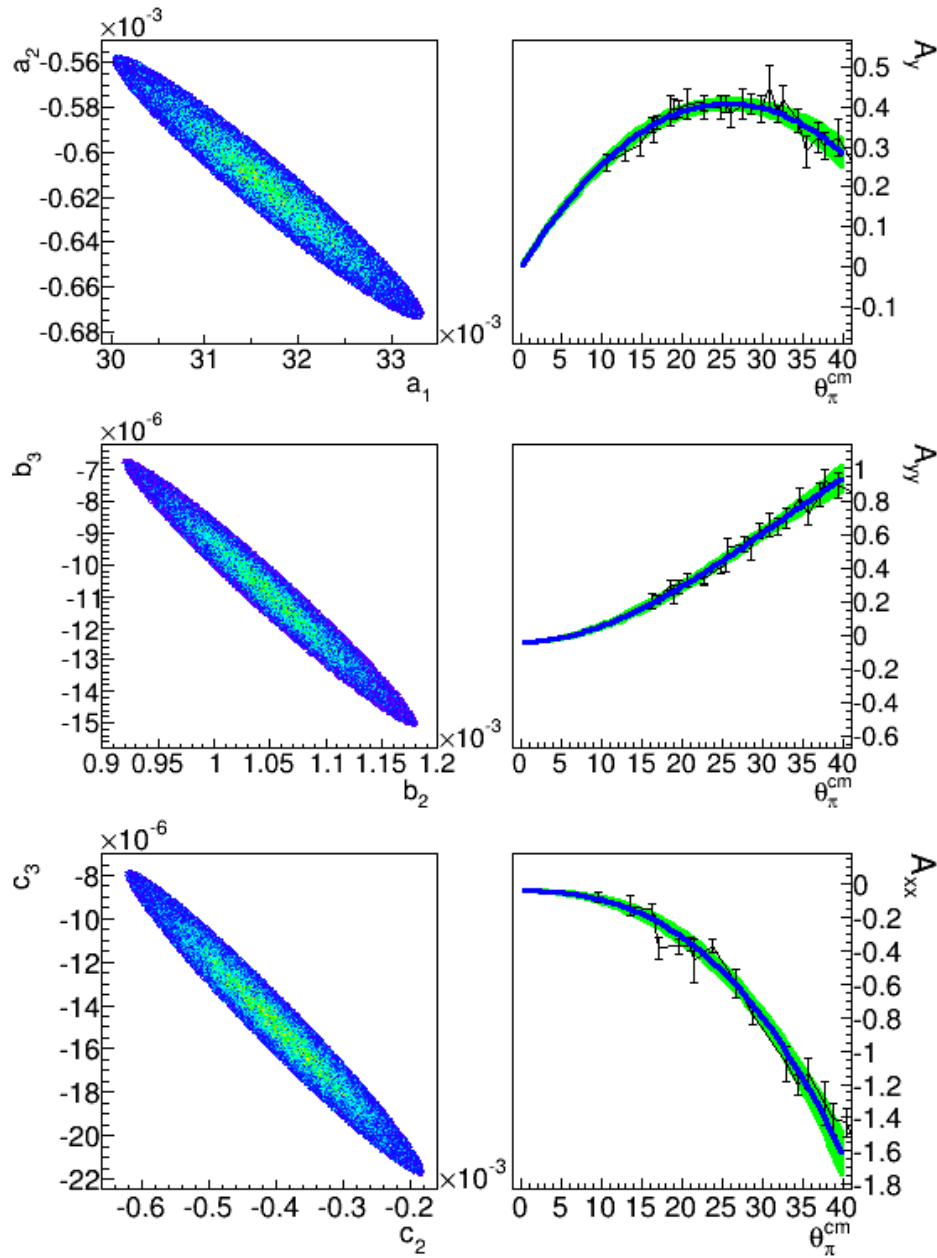
Figure 4.18: Variation of pd-elastic analyzing powers.

illustrated in Fig. 4.18 and 4.20. The data plotted in left column of Fig. 4.18 are the free parameters of the fit functions (Eq. 4.2) for the analyzing powers within the error ellipses. The new fit functions corresponding these varied parameters are plotted in the right side. Fig. 4.19 shows the distributions of the target polarizations obtained with varied fit functions. In Fig. 4.20 the distributions of the
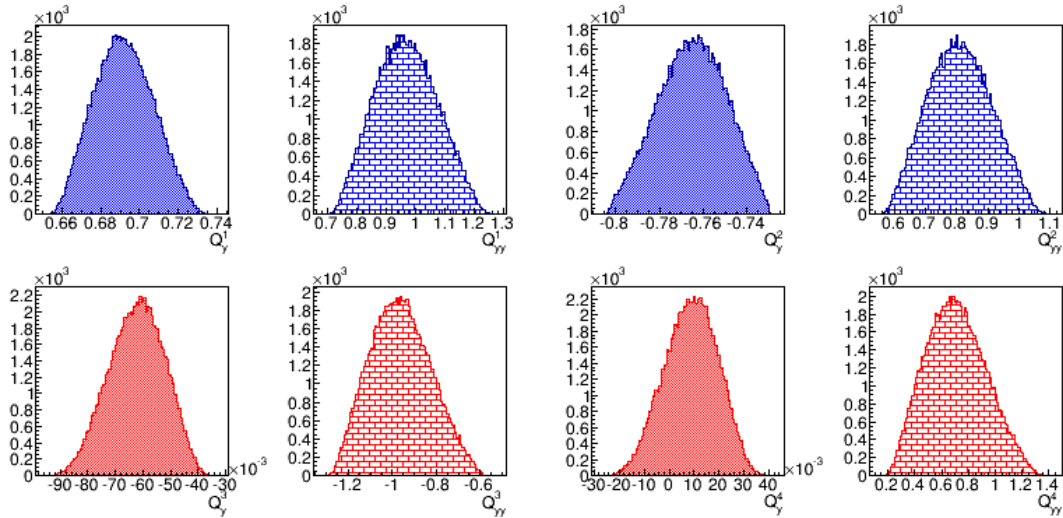
Figure 4.19: The distributions of the deuteron target polarizations measured using only the polarized data, with the analyzing powers of the d-p elastic scattering reaction varying within the error.

polarizations measured with new parameters are plotted, the upper and lower rows correspond to the polarization combination (1, 2) and (3, 4) respectively. The full widths at the half maximum (FWHM) of these distributions are the systematic errors of the corresponding polarizations, originated from the uncertainties of the analyzing powers A_y, A_{yy} and A_{xx}. The polarizations of all the four polarization modes measured using only the polarized data, together with the static and systematic errors are summarized in Table 4.2.

Table 4.2: The ideal and the measured polarizarions, as well as the statistic and systematic uncertainties.

Pol.	Q_y			Q_{yy}		
	Ideal	Measured	Sys. err.	Ideal	Measured	Sys. err.
Mode 1	+1	0.69 ± 0.01	0.02	+1	0.96 ± 0.01	0.11
Mode 2	−1	-0.76 ± 0.01	0.02	+1	0.80 ± 0.02	0.11
Mode 3	0	-0.06 ± 0.02	0.01	−2	-0.97 ± 0.02	0.15
Mode 4	0	0.01 ± 0.03	0.01	+1	0.69 ± 0.06	0.25

Using the same approach the systematic errors caused by the analyzing-power uncertainties in the polarization measurement that introduced in subsection 4.2.1.2 were evaluated as well. Table 4.3 presents the polarizations of the polarization modes 1 and 2, measured using both polarized and unpolarized data, together with the statistic errors and the systematic errors originated from A_y, A_{yy} ans A_{xx} of $p\vec{d} \rightarrow pd$. The results in Table 4.2 measured using the polarized data only, and those in Table 4.3 measured using both polarized and unpolarized agree with
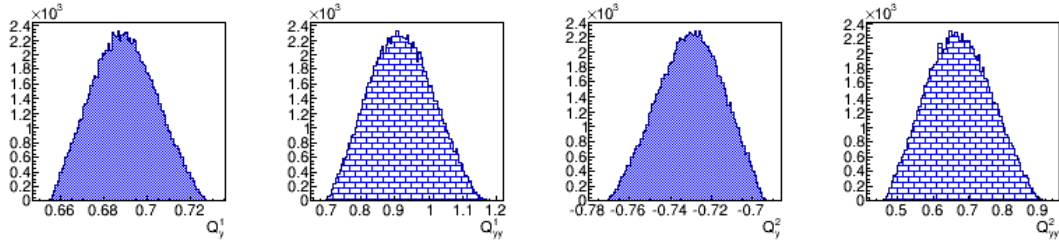
Figure 4.20: The distributions of the deuteron target polarizations measured using both the polarized and unpolarized data, with the analyzing powers of the d-p elastic scattering reaction varying within the error.

Table 4.3: The ideal and the measured polarizarions measured with both polarized and unpolarized data, as well as the statistic and systematic uncertainties.

Pol.	Q_y			Q_{yy}		
	Ideal	Measured	Sys. err.	Ideal	Measured	Sys. err.
Mode 1	$+1$	0.69 ± 0.01	0.02	$+1$	0.92 ± 0.07	0.10
Mode 2	-1	-0.73 ± 0.01	0.02	$+1$	0.67 ± 0.06	0.10

each other within the experimental error. This indicates that both approaches introduced in subsections 4.2.1.2 and 4.2.1.3 are valid. However, the measurement without the unpolarized data can evaluate systematic errors completely whereas the measurement with the unpolarized data is not able to steer clear of the instability problem, thus not all the error sources can be included. In addition the approach using the unpolarized data can not be applied to the mode 3 (0, -2) and 4 (0, +1). Due to these reasons the polarizations extract with the second approach are used to measured the analyzing powers of the deuteron–proton charge-exchange breakup reaction $p\vec{d} \to n\{pp\}$.

Since the difference and the mean value of the target polarizations are directly used when measuring the analyzing powers of the charge-exchange reaction (refer Sec. 4.3), it is preferable to have these values as well. Instead of working out the differences and the mean values from the polarizations, we measured them directly. By replacing the polarizations in Eq. 4.12 with the differences and averages $\Delta Q_y = Q_y^a - Q_y^b$, $\Delta Q_{yy} = Q_{yy}^a - Q_{yy}^b$ and $\langle Q_y \rangle = \frac{1}{2}(Q_y^a + Q_y^b)$, $\langle Q_{yy} \rangle = \frac{1}{2}(Q_{yy}^a + Q_{yy}^b)$ one gets

$$r(\theta, \phi) = \frac{\frac{3}{2}A_y(\theta)\cos\phi\Delta Q_y + \frac{1}{4}[A_{xx}(\theta)(1 - \cos 2\phi) + A_{yy}(\theta)(1 + \cos 2\phi)]\Delta Q_{yy}}{2 + 3A_y(\theta)\cos\phi \langle Q_y \rangle + \frac{1}{2}[A_{xx}(\theta)(1 - \cos 2\phi) + A_{yy}(\theta)(1 + \cos 2\phi)] \langle Q_{yy} \rangle}$$
(4.13)

The average and the difference can be extracted by fitting the observable R (4.10) with above formula. Table 4.4 presents the polarizations in terms of the difference

and average, together with the statistic and systematic errors.

Table 4.4: The ideal and the measured polarizarions in the form of difference and average, as well as the statistic and systematic uncertainties.

Pol.	Modes 1,2			Modes 3,4		
	Ideal	Measured	Sys. err.	Ideal	Measured	Sys. err.
ΔQ_y	$+2$	1.46 ± 0.01	0.03	0	-0.07 ± 0.01	0.01
$\langle Q_y \rangle$	0	-0.03 ± 0.01	0.01	0	-0.02 ± 0.02	0.01
ΔQ_{yy}	0	0.17 ± 0.02	0.01	-3	-1.68 ± 0.02	0.14
$\langle Q_{yy} \rangle$	$+1$	0.88 ± 0.03	0.11	-0.5	-0.13 ± 0.06	0.03

4.2.2   Polarimetry with $p\vec{d} \to d\pi^+ n_{sp}$

Simulation (Fig. 4.2) shows that at the beam incident energy of $T_p = 600$ MeV the quasi-free reaction $p\vec{d} \to d\pi^+ n_{sp}$ is covered by the forward and positive side sub-detectors of ANKE, and its vector analyzing power (A_y) within the ANKE acceptance is well measured. Therefore the deuteron vector polarization can be measured via the quasi-free reaction $p\vec{d} \to d\pi^+ n_{sp}$ as well, which can be used to verify the validity of the polarimetry that utilizes the proton-deuteron elastic reaction $p\vec{d} \to pd$. The track reconstruction becomes much more complicated in the presence of a long storage cell target because the event vertices are not known as precisely as in the case of a point-like target (e.g. a cluster jet target), therefore one has to determine the event vertices so that the momentum can be measured with a sufficient precision. First of all, the general procedure of Fd and Pd data analysis, and the technique of vertex fit and momentum reconstruction are discussed, which is followed by the event selection for the quasi-free reaction $p\vec{d} \to d\pi^+ n_{sp}$ and the procedure to extract the deuteron vector polarization via this reaction. Finally the vector polarizations (Q_y) measured via the quasi-free reaction $p\vec{d} \to d\pi^+ n_{sp}$ are compared with the results extracted from the proton-deuteron elastic reaction $p\vec{d} \to pd$.

4.2.2.1   General Procedure of Fd and Pd Data Analysis

In this subsection the general procedure of processing the data from the forward (Fd) and positive side (Pd) detection systems are introduced. In this experiment the information obtained from the the forward and positive side detection systems mainly include hit positions in the multiwire proportional chambers (MWPCs) and the time and energy signals measured by the plastic scintillators. In addition, the scintillators can also provide spatial information. The y-coordinate of a

hit in a scintillator is measured as the weighted average of the time signals which are provided by the upper and lower PMTs, with an precision of about 1.5-2.2 cm. The x and z coordinates are given by the positions of the scintillators, with resolutions defined by the width[7] and thickness of the scintillator respectively.

For the experiments which utilize the gas cluster target [74–76] or the solid strip target [72] the momentum reconstruction is relatively simple since in theses cases the event vertices are fixed. For a charged particle detected by the forward (Fd) or the positive side (Pd) detection system its trajectory can be separated into two parts. The first part begins from the vertex and ends at the exit window of the D2 magnet, it must be a curve because of the bend force of D2. On the contrary, the second part, which connects the start and stop scintillation counters and transverses the gas detectors, is basically a straight line since the magnetic field out of the D2 magnet is rather weak. Accordingly the momentum reconstruction is also consist of two stages. First one has to find the straight part based on the hit positions provided by the multiwire proportional chambers (MWPCs) and the scintillation counters. For an event one usually get many straight lines from these hit positions, it is therefore necessary to further filter these lines using some criteria. For instance the straight line is expected to pass through the D2 exit window, to include as many as hits, to have high confidence level[79]. The straight part of a trajectory is described by two parameters, namely the two-dimensional coordinate of the cross with the D2 exit window and its angle with respect to the D2 window. These two parameters are then used to determine the curved section of the trajectory in conjunction with the vertex coordinate and the magnetic field map inside D2. From the curved trajectory the rigidity of the track is deduced, based on which the momentum can be obtained as soon as the particle is identified. There many approaches to identify particles, for instance the $\Delta E/E$ method, the time-of-flight method etc. In the following we shall introduce a method via which both particle identification (PID) and event selection can be achieved simultaneously. Later this method will also be used in the vertex reconstruction.

The Δ_{TOF} method   Consider an event with two charged tracks detected. First we assume this event is of the process we are interested in and assign particle type for each track. Then we are able to calculate the difference of the time-of-flight (TOF) of these two particles based on the trajectories measured previously. The calculated difference of the time-of-flight (Δ_{TOF}^{cal}) and the measured difference of

---

[7]Since the two planes of the forward hodoscope are shifted by a half width with respect to each other(see Fig. 3.3), the resolution of x are roughly one half of the counter width.

the time-of-flight (Δ_{TOF}^{mea}) ought to agree within the experimental error provided our assumption is correct. Therefore by comparison of calculated and measured time-of-flight (TOF) differences one can identify particles as well as select events. Let's take the reaction $pd \to d\pi^+ n_{sp}$ as example. We denote the final particles of a two-tracked event as P_1 and P_2, assign one of them, say P_1 , as π^+, the other one (P_2) as deuteron. Since the lengths of the trajectories (L_1 and L_2) and the rigidities ($B\rho_1$ and $B\rho_2$) of P_1 and P_2 have already been obtained through the track reconstruction, their time of flight can be steadily calculated provided the particle types are assigned. For particle P_1 its time of flight from the vertex to the stop scintillation counter is

$$TOF_1 = \frac{L_1}{v_1} = \frac{L_1}{\frac{P}{\sqrt{P^2+M_\pi^2}}} = \frac{L_1\sqrt{(B\rho_1 Q_\pi)^2 + M_\pi^2}}{B\rho_1 Q_\pi}, \tag{4.14}$$

likewise TOF of P_2 is

$$TOF_2 = \frac{L_2}{v_2} = \frac{L_2}{\frac{P}{\sqrt{P^2+M_d^2}}} = \frac{L_2\sqrt{(B\rho_2 Q_d)^2 + M_d^2}}{B\rho_2 Q_d}, \tag{4.15}$$

thus the difference of the time-of-flight between P_1 and P_2 is calculated as

$$\Delta_{TOF}^{cal} = TOF_1 - TOF_2. \tag{4.16}$$

In the formula 4.14, 4.15 and 4.16 Q_π and Q_d represent respectively the electric charge of π^+ and deuteron. In this experiment the start time is unknown therefore the time of flight (TOF) itself is not measurable. However, since the the start time is identical for all the particles in the same event, the difference of the time of flight can be calculated as the difference of the stop time (t_1 and t_2), which were given by the stop scintillation counters, i.e.

$$\Delta_{TOF}^{mea} = t_1 - t_2. \tag{4.17}$$

Note the charged particles in the final state of the reaction are of different types, so one needs to exchange the particle-type assignments, i.e. assume that P_1 is dueteron and P_2 is π^+, or one can judge which particle is heavier and assign this particle as deuteron. As an example, Fig. 4.21 illustrates how the difference of time of flight is used for particle identification and event selection. In this plot the horizontal and vertical axes represent respectively the measured (Δ_{TOF}^{mea}) and

calculated (Δ_{TOF}^{cal}) time of flight with the assumption that both the final particles are protons. The events located on the diagonal are those with both final particles being protons. Events with proton and π^+ or deuteron and π^+ are also shown.
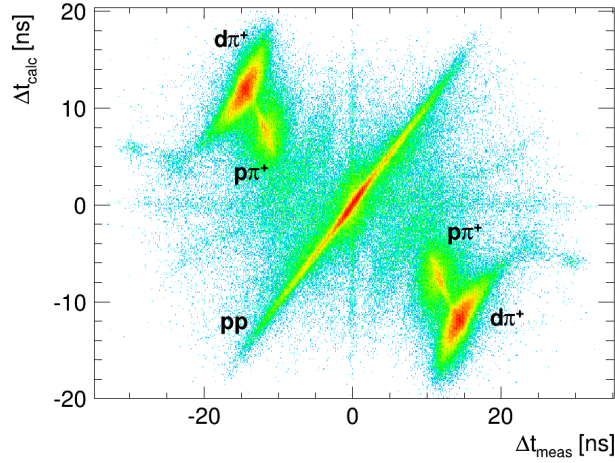
Figure 4.21: Time-of-flight difference.

In the above discussion the stop time is measured by the scintillation counters, which in the raw data is essentially the real time added by a time delay. Specifically speaking, the time signal given by a scintillation counter c is

$$t_c = t_c^{real} + \delta t_c \tag{4.18}$$

where t_c^{real} denotes the real time when particle hit the detector, and δt_c is the delay between the real time and the signal. Usually the time delays are different for different scintillation counters, therefore one has to adjust the time delays for all the counters in order to get correct time-of-flight difference. In the following we shall introduce the time delay corrections among the scintillation counters in the forward (Fd) and positive side (Pd) detection systems as well as the time calibration between these two detection system.

Time calibration for counters in Fd Since the data analyses in this thesis do not need the the time information provided by the TOF-stop scintillation counters in Fd, we only discuss the time delay correction for the TOF-start scintillation counters. Fig. 4.22 illustrates the time delay correction for the counters in the forward TOF-start array. The whole process can be divided into three stages. As the first step the correction are performed within plane A. As shown in the plot, there is a half-width shift between plane A and B. Such an alignment is especially designed for time calibration. Due to the smallness of the distances
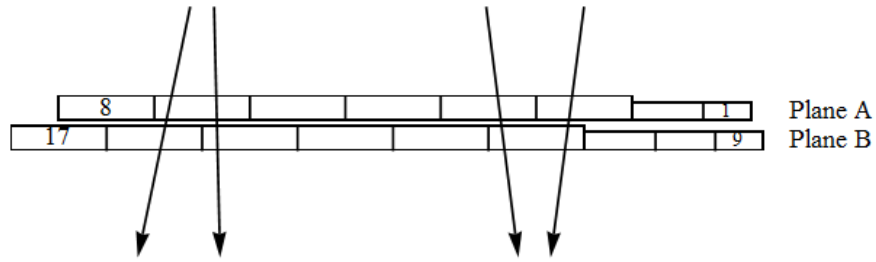
Figure 4.22: Time calibration for the forward hodoscopes.

between plane A and B, the time for a particle transversing two adjacent counters can be regarded as being identical within the time resolution. Therefore, for two neighbouring counters, say c_3 and c_4 in plane A and the counter facing the interval between them, i.e. c_{12}, the following relations

$$t_{c_{12}} - t_{c_3} = \delta t_{c_{12}} - \delta t_{c_3} \tag{4.19}$$

and

$$t_{c_{12}} - t_{c_4} = \delta t_{c_{12}} - \delta t_{c_4} \tag{4.20}$$

hold, from which the relative time delay between the counters c_5 and c_6 are derived, namely

$$\delta t_{c_3} - \delta t_{c_4} = [t_{c_{12}} - t_{c_4}] - [t_{c_{12}} - t_{c_3}]. \tag{4.21}$$

Using the same trick, relative time delays between all the neighbouring counters in plane A can be obtained. The time calibration for the counters in plane B is basically the same with what is employed for plane A, for example the relative time delay between counters c_{15} and c_{16} is

$$\delta t_{c_{15}} - \delta t_{c_{16}} = [t_{c_{15}} - t_{c_7}] - [t_{c_{16}} - t_{c_7}]. \tag{4.22}$$

As the second step one needs to adjust the relative delay between plan A and B. The relative time delay between two adjacent counters in plane A and B, for instance c_1 and c_9, is the difference between the time signal for a particle passing through them, i.e.

$$\delta t_{c_1} - \delta t_{c_9} = t_{c_1} - t_{c_9} \tag{4.23}$$

Finally, all the counters in plane A and B are calibrated uniformly using relative delays obtained the previous steps. Fig. 4.23 shows the spectra of the time delays between the adjacent Fd start counters in plane A and plane B.
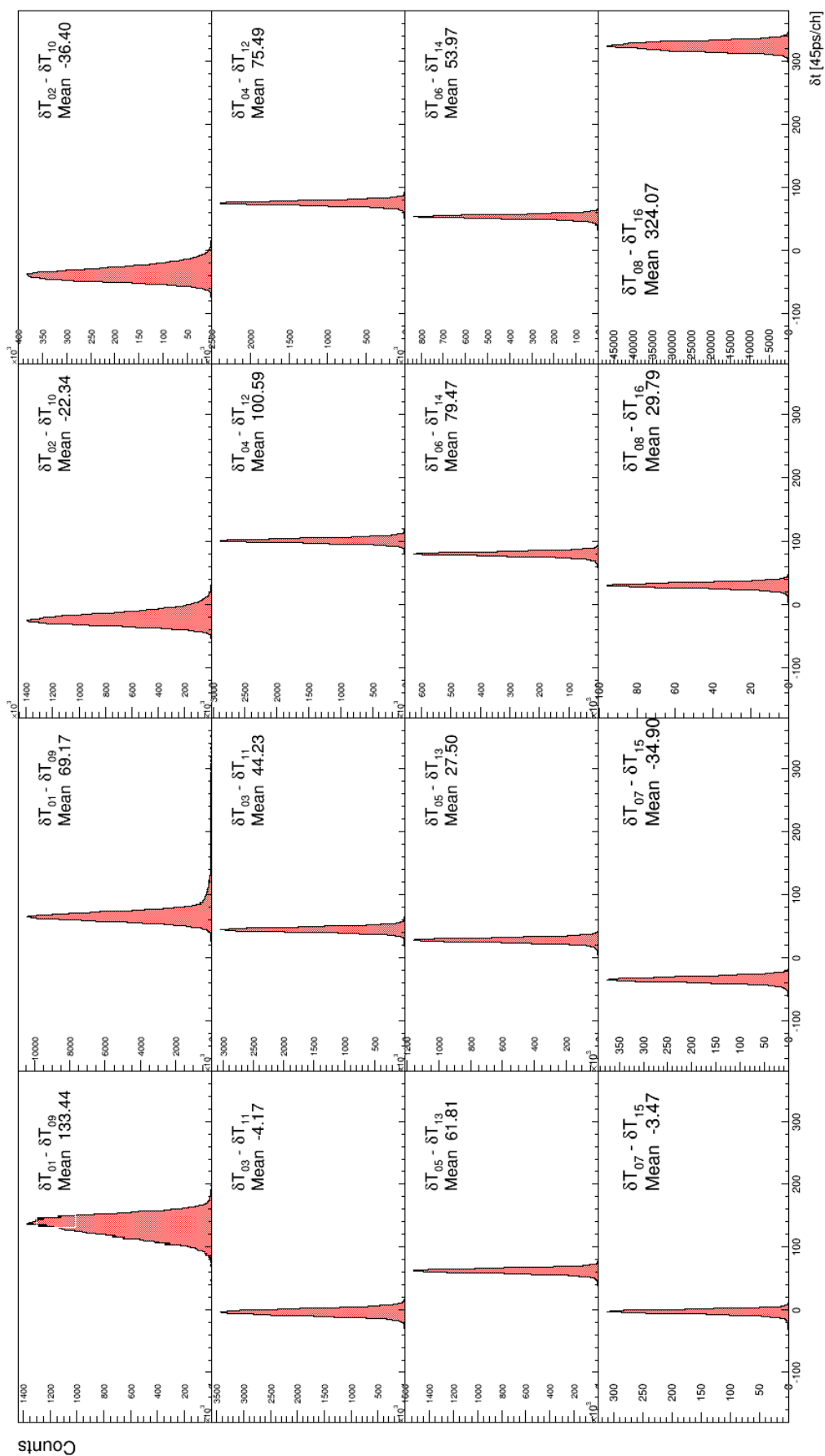
Figure 4.23: Time delay correction for Fd start counters.

Time calibration for counters in Pd In the positive side detection system the TOF-start counters are installed next to the exit window of D2, while the TOF-stop counters are placed in the focal plane. The large distance between storage cell and the focal plane makes it preferable to employ the stop counters for time measurement. Therefore only the stop counters need to be calibrated. The technique used here is similar to what is used for the start counters in the forward detection system. It was found that there were many tracks transverse the adjacent stop counters on the focal plane, which were regarded as transversing the adjacent counters at the same time. Therefore the relative time delay between two neighbouring counters, denoted c_i as and c_{i_1} , are $\delta t_{c_i} - \delta t_{c_{i+1}} = t_{c_i} - t_{c_{i+1}}$. Fig. 4.24 shows the time delay between the neighboring time counters in the TOF-stop array of Pd, through which the common time calibration was performed among all these counters.

Time calibration between Fd and Pd For some events of $pd \rightarrow d\pi^+ n_{sp}$, the final charged particles deuteron and π^+ are detected respectively by the forward (Fd) and positive side (Pd) detection systems. Due to the time delay between these two systems the measured value (Δ_{TOF}^{mea}) of the time-of-flight difference between deuteron and π^+ will differ from the real value by $\delta t_{Fd} - \delta t_{Pd}$. On the other hand the real value can be approximated as the calculated time-of-flight difference (Δ_{TOF}^{cal}). Therefore the relative time delay between the forward (Fd) and positive side (Pd) detection systems can be obtained by the comparison of the measured (Δ_{TOF}^{mea}) and the calculated (Δ_{TOF}^{cal}) difference of the time of flight between deuteron and π^+, i.e.

$$\delta t_{Fd} - \delta t_{Pd} = \Delta_{TOF}^{mea} - \Delta_{TOF}^{cal} \tag{4.24}$$

Fig. 4.25 shows the distribution of $\Delta_{TOF}^{mea} - \Delta_{TOF}^{cal}$, the deviation of the peak position from the coordinate origin is the time delay between Fd and Pd.

Vertex reconstruction and geometry correction In order to achieve sufficient luminosity a storage cell (SC) was employed in this experiment. The large extent of the storage cell (370 mm along the beam direction) makes the event vertices awfully uncertain. As a consequence, it is in principle impossible to determine the curved part of the particle trajectory. In other words, the momentum is immeasurable. Therefore one has to figure out an approach to determine the event vertecies, or strictly speaking, to reduce their uncertainties. As the preliminary step the event vertices are assumed to locate at the feeding tube exit. Based one
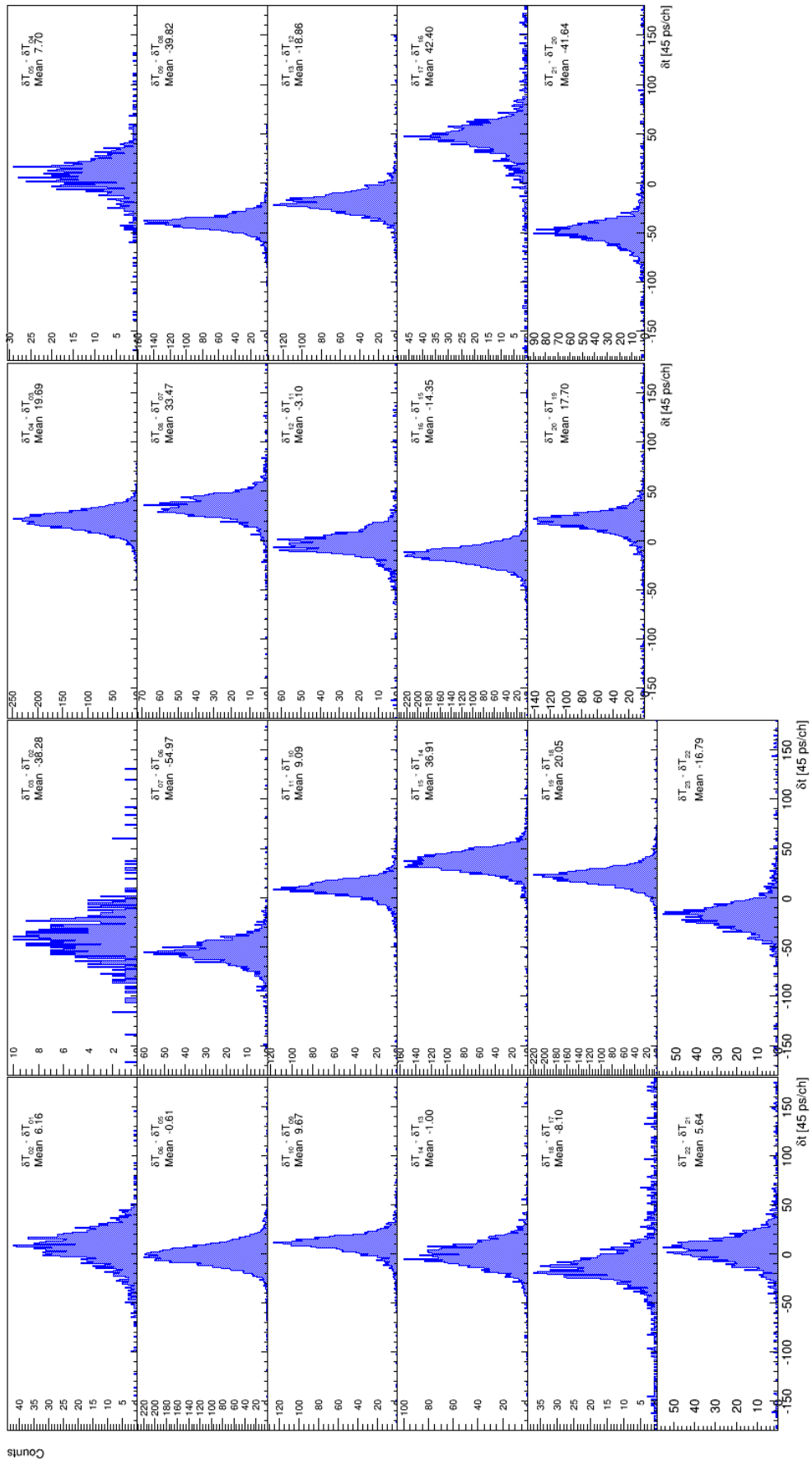
Figure 4.24: Time delay correction for Pd start counters.
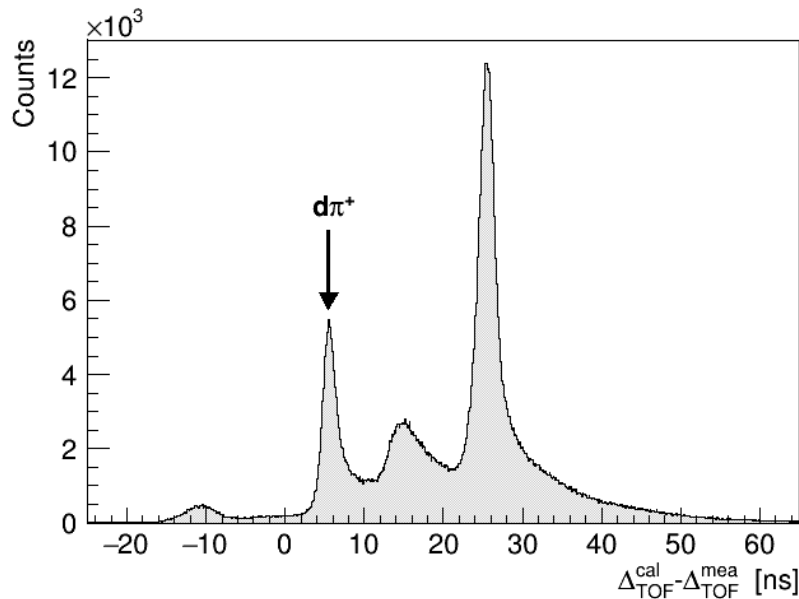
Figure 4.25: Time calibration between the forward detector (Fd) and positive side detector (Pd). The difference between zero and the position of the $d - \pi^+$ peak is the relative time delay between the two sub-detection systems.

this assumption one then determine the rigidity as well as the exit directions of the final charged particles. Evidently the tracks obtained with this procedure are rather rough, nevertheless it is sufficient to use these tracks for the purpose of time delay adjustment. In addition, the detector geometric parameters needed in the track reconstruction process, such as the positions and angles of the multiwire proportional chambers (MWPCs), are measured before experiment. However, due to the errors in the measurements there may exist non-negligible deviations from the real parameters, which in turn will cause errors in the track reconstruction. For the forward detection system (Fd), since the distances among the chambers are short and the tracks are less bent by the D2 magnet, the track reconstruction is more sensitive to the geometric parameters. It is clear from the above discussion that one has to reconstruct the event vertices as well as correct the geometric parameters in order to measure the momentum precisely. Fot this purpose the ANKE-Collaboration has developed an effective method[79, 122], which will be introduced in the following. The deviations of the momenta and trajectories caused by the errors of the event vertices and geometric parameters affect mostly the time of flight, the four-momentum conservation and the trajectory fitting qualities, therefore the event-vertex reconstruction and the correction of the geometric

parameters can can be achieved simultaneously by minimizing the quantity

$$\chi^2 = \sum \frac{(\Delta w)_i^2}{(\sigma^2 w)_i} + HW \cdot \sum (\Delta P)_i^2 + \sum \frac{(\Delta TOF)_i^2}{(\sigma^2 TOF)_i} \qquad (4.25)$$

In the above formula $\sum \frac{(\Delta w)_i^2}{(\sigma^2 w)_i}$ is calculated using the deviations between the fitted track and the clusters that measured by the chambers; ΔTOF is the deviation between the measured (Δ_{TOF}^{mea}) and calculated (Δ_{TOF}^{cal}) difference of the time of flight; $HW \cdot \sum (\Delta P)_i^2$ characterizes the kinematical restriction, the coefficient HW is used to enhance the sensitivity of χ^2 to the kinematical restriction. If all the final particles of one process are detected the the kinematical restriction manifest itself by the three-momentum conservation, whereas in the case where only one particle is not detected the invariant mass of the missing particle is used instead. In the present data analysis the Δ_{TOF}^{cal} between the final particles deuteron and π^+, the invariant mass of the undetected neutron of $pd \rightarrow d\pi^+ n_{sp}$, as well as the three-momentum conservation of $pd \rightarrow pd$ were used for the vertex reconstruction and geometry correction. Note the deuteron momentum of $pd \rightarrow pd$ is measured by the STT. Besides those discussed above an additional effective restriction was introduced later. The idea rest on the fact that all the beam particles which do not interact with the beam particles must travel along a common line[8] which is defined by the D2 magnet together with the beam momenta, which means that all the event vertices necessarily locate on this line. The vertex line can be obtained by simulation. Fig. 4.26 shows the vertex line for the settings in this experiment.
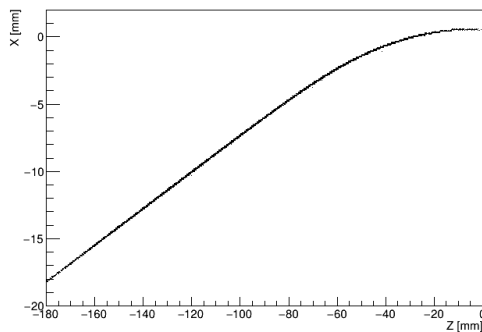
Figure 4.26: The beam line in the storage cell, projected in the xz plane.
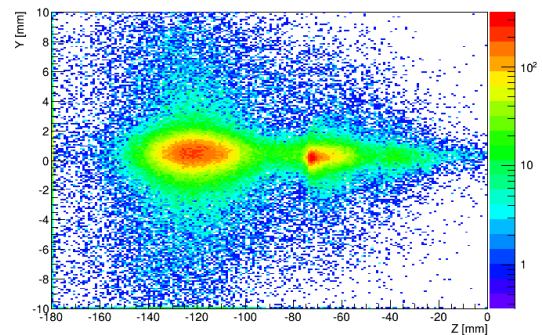
Figure 4.27: The reconstructed event vertices. The left and right spots correspond respectively to the cell target and the exit window of the target chamber.

---

[8]refereed as vertex line hereafter.

Event Selection and Kinematics of $pd \to d\pi^+ n_{sp}$

The reaction $pd \to d\pi^+ n_{sp}$ was selected with the Δ_{TOF} method which is introduced in paragraph 4.2.2.1. Refer to the plot of ANKE acceptance (Fig. 4.2), it is seen that all the deuterons produced in the reaction $pd \to d\pi^+ n_{sp}$ are detected by the forward detector (Fd), while the pions are detected by either the forward detector (Fd) or the positive side detector (Pd). Since the performances of the forward detector and the positive side detector are different, it is reasonable to perform the event selection for the events with pions in the forward (Fd) and positive side (Pd) detectors separately.[9] The events of $pd \to d\pi^+ n_{sp}$ are selected form the double-track events. Before assigning particle type a judgment is made on which particle is heavier by comparing the measured difference of the time of flight $\Delta_{TOF}^{mea} = t_{p_1} - t_{p_2}$[10] and the calculated valued with the assumption that both particles are protons, i.e. Δ_{ppTOF}^{cal}. p_1 is heavier if $\Delta_{ppTOF}^{cal} > \Delta_{TOF}^{mea}$. Then the heavy particle and light particle are assumed to be deuteron and pion respectively. The time-of-flight difference calculated with the $d - \pi^+$ assumption is compared with the measured time difference to select the reaction $pd \to d\pi^+ n_{sp}$. Fig. 4.28(a) and 4.28(b) are the distributions of $\Delta_{TOF}^{cal} - \Delta_{TOF}^{mea}$, events with in 3σ of the peaks at zero are selected as $pd \to d\pi^+ n_{sp}$. The corresponding missing-mass spectra of these events are plotted in Fig. 4.28(c) and 4.28(d), which show prominent peaks at the neutron invariant mass. The background are subtracted using the nitrogen data.

To analysis the quasi-free process $p\vec{p} \to d\pi^+$ properly one has to take into account the consequences due to the Fermi motion of the proton in the deuteron. First of all, the total energy of the reaction $p\vec{p} \to d\pi^+$ is not merely defined by the beam energy, the Fermi momentum also contribute to it. As a result the effective beam kinetic energy are distributed over a wide range instead of being a single value. The effective beam kinetic energy are given by [123]

$$T_{eff} = [s - (m_b + m_t)^2]/2m_t \tag{4.26}$$

where m_b and m_t are used to denote the masses of the beam particle and the target particle, both of which in the present case are proton mass. s is the square of the static mass of the quasi-free system, which is calculated based on the measured

---

[9]For brevity we note these two kinds of events by 'FdFd event' and 'FdPd event' respectively.
[10]p_1 and p_2 are used to denote the two charged particles.
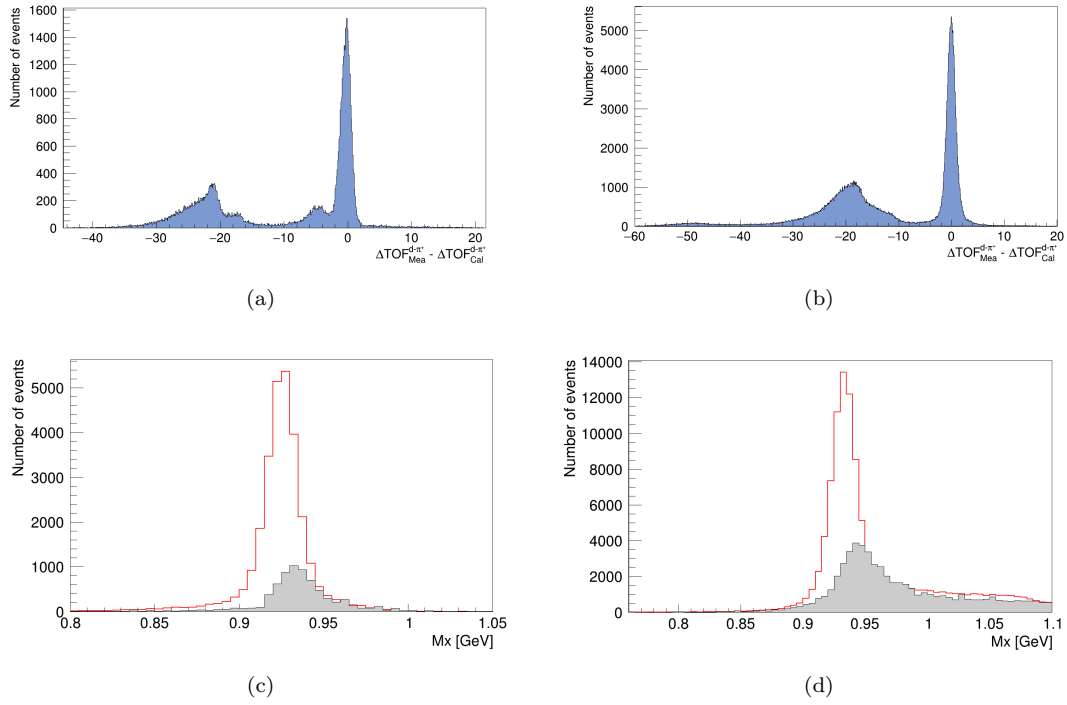
Figure 4.28: Event selection for the reaction $pd \rightarrow d\pi^+ n_{sp}$ based on the TOF difference method. Fig. (a) and Fig. (b) show the difference between the measured time-of-flight and the time-of-flight calculated with the assumption that the final particles are deuteron and π^+. The events within in $\pm 3\sigma$ of the peaks at $\Delta_{TOF}^{cal} - \Delta_{TOF}^{mea} = 0$ are selected for the subsequent analyses. Fig. (c) and Fig. (d) are the missing mass spectra of $pd \rightarrow d\pi^+ X$ for the selected events, the background caused by the collisions between the beam halo and the cell wall are subtracted using the nitrogen target data. The figures in the left and right colunms correspond to the FdFd and FdPd events respectively.

four-momenta of the final particles deuteron and pion as

$$s = (\breve{p}_d + \breve{p}_{\pi^+})^2 \tag{4.27}$$

In Fig. 4.29(a) the effective beam kinetic energy T_{eff} of the process $p\vec{p} \rightarrow d\pi^+$ in this experiment is plotted. The events distributed between 570 MeV and 620 MeV are used for the polarimetry. The proton analyzing power of $\vec{p}p \rightarrow d\pi^+$ between 570 MeV and 620 MeV, taken from the SAID database, is plotted in Fig. 4.29 as a function of the pion scattering angle in the c.m. system. Secondly, the reference frame of the quasi-free system is rotated with respect to the laboratory reference. Therefore the scattering angle $\theta_{pi^+}^{cm}$ is defined as the angle between π^+ and the beam particle proton in the quasi-free system. The azimuthal angle ϕ, which enters in the polarized cross section (Eq. 4.29), is defined as the angle between the

(a) T_{eff} of $pd \to d\pi^+ n_{sp}$ at $T_p = 600$ MeV.

(b) A_y of $\vec{p}p \to d\pi^+$ between 570 MeV (blue) and 620 MeV (red) from SAID
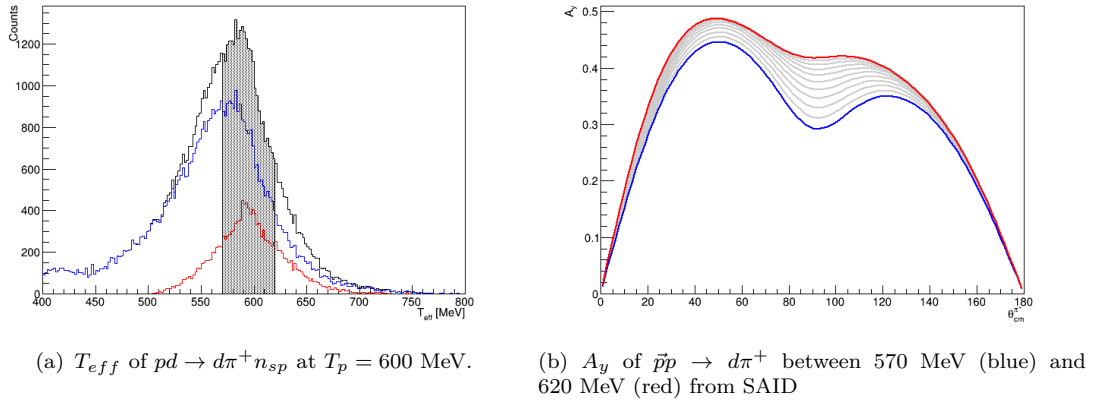
Figure 4.29: The left panel shows the distribution of the effective nucleon energy T_{eff} of the reaction $pd \to d\pi^+ n_{sp}$ at $T_p = 600$ MeV, Fd and Pd distributiions are marked with red and blue respectively. Events within the interval [570, 620] MeV are used. The proton analyzing power A_y of $\vec{p}p \to d\pi^+$ from the SAID database between 570 MeV (blue) and 620 MeV (red) are plotted as a function of the pion scattering angle on the right panel.
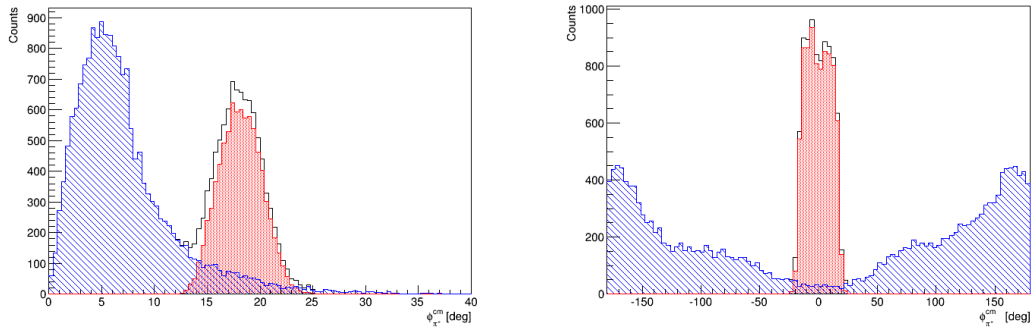
Figure 4.30: θ and ϕ distributions of $p\vec{p} \to d\pi^+$ in the projectile helicity frame

normal of the scattering plane[11] and the spin quantization axis[12]. The measured angles $\theta_{\pi^+}^{cm}$ and ϕ are plotted in Fig. 4.30(a) and 4.30(b) separately. Note the proton analyzing power $A_y(\theta)$ from the SAID database (Fig. 4.29(b)) is given for the process $\vec{p}p \to d\pi^+$, thus the transformation

$$\theta \to \pi - \theta \tag{4.28a}$$

$$\begin{cases} \phi \to \phi - \pi, & \text{if } \phi > 0, \\ \phi \to \phi + \pi, & \text{if } \phi < 0. \end{cases} \tag{4.28b}$$

---

[11]i.e. the y' axis of the projectile helichty system (refer Fig. 1.2)

[12]in present case the Y axis of the laboratory reference.
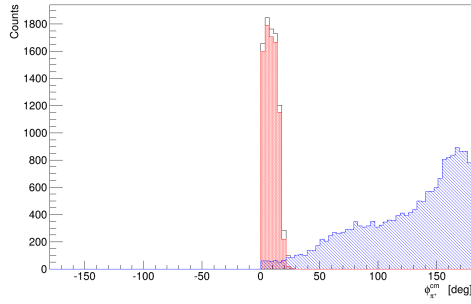
Figure 4.31: In order to have larger statistics, the events of $p\vec{p} \rightarrow d\pi^+$ with $\phi < 0$ are flipped to their opposite sides, where $\phi > 0$. Accordingly the sign of the polarization are changed, i.e. the events on the left part of Fig. 4.30(b) are flipped to the right side. By this trick the statics are approximately doubled.

has to be performed so that the analyzing power can be used in the present case where the target is polarized.

4.2.2.2 Extraction of deuteron vector polarization from $p\vec{d} \rightarrow d\pi^+ n_{sp}$

In the projectile helicity system which is defined by the final particles deuteron and π^+, the differential cross section of the quasi-free reaction $p\vec{p} \rightarrow d\pi^+$ is given by

$$\frac{d\sigma}{d\Omega}^P (\theta, \phi) = \frac{d\sigma}{d\Omega}^0 (\theta)[1 + Q_y A_y(\theta) \cos\phi] \tag{4.29}$$

where $\frac{d\sigma}{d\Omega}^0(\theta)$ is the cross section of the unpolarized reaction $pp \rightarrow d\pi^+$, Q_y and $A_y(\theta)$ are the polarization and the analyzing power. The number of events with π^+ in the solid angle $\Omega(\theta, \phi)$ is

$$N^1(\theta, \phi) = \frac{d\sigma}{d\Omega}^0 (\theta)[1 + Q_y^1 A_y(\theta) \cos\phi] \cdot L^1 \cdot \varepsilon^1 \tag{4.30a}$$

for the state 1, and

$$N^2(\theta, \phi) = \frac{d\sigma}{d\Omega}^0 (\theta)[1 + Q_y^2 A_y(\theta) \cos\phi] \cdot L^2 \cdot \varepsilon^2 \tag{4.30b}$$

for the state 2. The polarization states 1 and 2 were switched between each other every 10 seconds, thus the luminosity and the detection efficiency are identical for them, namely $L^1 = L^1$, $\varepsilon^1 = \varepsilon^2$. The ideal vector polarizations of states 1 and 2 satisfy $Q_y^1 = -Q_y^2$, the values measured by $p\vec{d} \rightarrow pd$ are very close (see Table 4.3). So it is reasonable to assume $Q_y^1 = -Q_y^2 = Q_y$. Combine these conditions and Eq. 4.30 one can get

$$\frac{N^1 - N^2}{N^1 + N^2} = A_y(\theta) \cdot \cos\phi \cdot Q_y. \tag{4.31}$$

The polarization Q_y can be extract by fitting the observable $\frac{N^1-N^2}{N^1+N^2}(\theta)$ with $A_y(\theta) \cdot \langle\cos\phi\rangle \cdot Q_y$. In order to fully make use of the available statistics the data of

$\cos\phi < 0$ are flip to the region where $\cos\phi > 0$, accordingly the sign of the polarization are changed as well. $\langle\cos\phi\rangle$ are taken as the weighted average of $\cos\phi$. Fig. 4.32 shows the fitting of $\frac{N^1-N^2}{N^1+N^2}(\theta)$ by $A_y(\theta) \cdot \langle\cos\phi\rangle \cdot Q_y$, the extract value polarization is 0.75 ± 0.07, which is in consistency with which is measure by STT data.
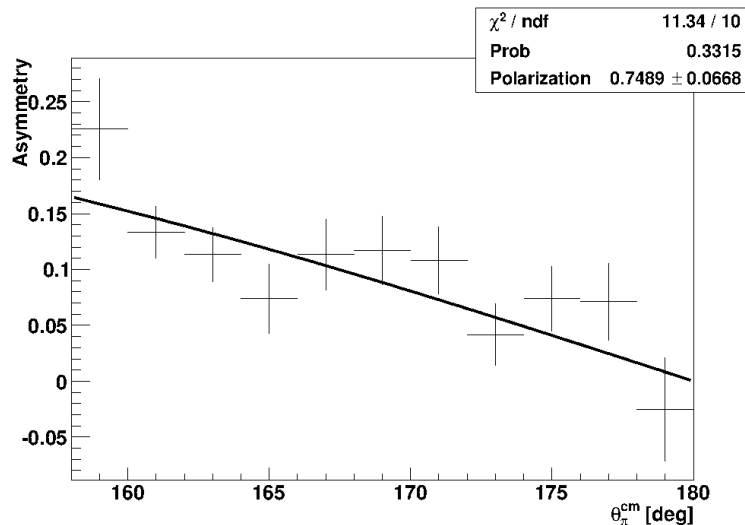
Figure 4.32: Vector polatization measured with $pp \to d\pi^+$.

4.2.3 Summary of the Polarization Measurement

Two reference reactions ($p\vec{d} \to pd$ and $p\vec{p} \to d\pi^+$) and three methods were used used for the target polarization measurement. The proton–deuteron elastic scattering were measured by the STTs, and the quasi-free reaction $p\vec{p} \to d\pi^+$ were registered in the forward (Fd) and positive side detection systems. When measuring the polarizations with $p\vec{d} \to pd$, comparisons were performed between the polarized and the unpolarized data, as well as between the polarized data of different modes. The data of the quasi-free reaction $p\vec{p} \to d\pi^+$ were mainly used to check the results form the STT data. Results from the three methods are consistent with each other with in the error, this means all the three methods are reliable. Note only in the method of comparing the pd–elastic data of different polarization modes can the systematic errors be estimated completely, therefore only the results form this method were used to measure the pd charge–exchange reaction $p\vec{d} \to n\{pp\}_s$ (see next section).

4.3   Measurement of the Proton-Deuteron Charge-Exchange Reaction

The deuteron charge-exchange reaction $pd \rightarrow n\{pp\}_s$ is selected from the events with two tracks in the silicon tracking telescopes (see Fig. 4.2). As illustrated in Fig. 4.33(a), protons in STTs are identified utilizing the energy deposit (Refer Sec. 4.2.1.1). Fig. 4.33(b) is the missing mass distribution of those double-track events, which shows a prominent peak at the neutron invariant mass. The background from the storage cell is subtracted using the nitrogen data scaled by a scaling factor, which is determined by the fitting beyond the peak. Note only the events within $\pm 3\sigma$ of the neutron peak are used in the subsequent analyses. In the kinematical region in terms of the three-momentum transfer q versus the
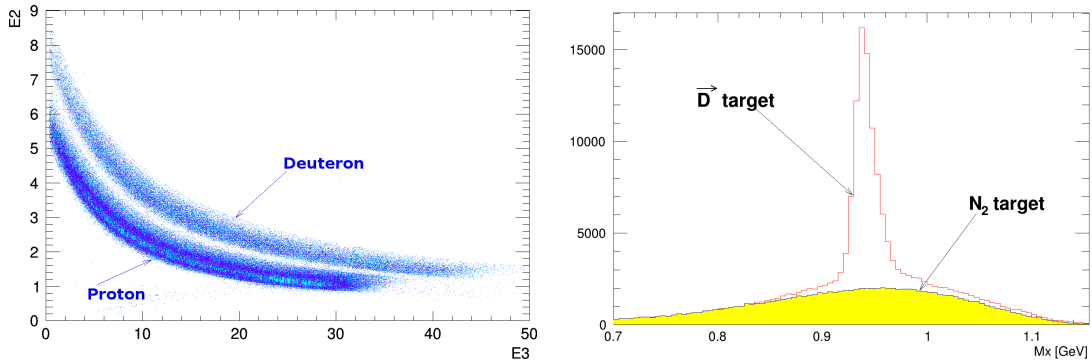
Figure 4.33: The left panel illustrates the particle identification for the double-track events in the STTs by the $\Delta E/E$ method. The right panel is the missing mass spectrum of $pd \rightarrow \{pp\}_s X$ for the diproton events. The nitrogen data is used for background subtraction. The events within $\pm 3\sigma$ of the neutron-mass peak are employed for the polarization measurement.

pp excitation energy E_{pp}, the events of $pd \rightarrow n\{pp\}$ are scattered in two separated areas (Fig. 4.34), which correspond to the cases where the two final protons enter the same (blue) or different (red) STT. In order to penetrate the most inner silicon microscope strip detector of one STT, a proton has to possess kinetic energy large than 2.5 MeV, which corresponds to momentum about 70 MeV/c. This necessarily means that, if the two final protons were detected by the same STT, the momentum transfer q to the proton pair must be larger than 140 MeV/c, and the excitation energy E_{pp} can be small. One the contrary, if the two protons are detected by two different STTs, E_{pp} must be large ($\gtrsim 6$ MeV) and q can be small because two protons are in opposite directions. As a result, the kinematic region where both q and E_{pp} are small, which is accessible in the first phase of the np
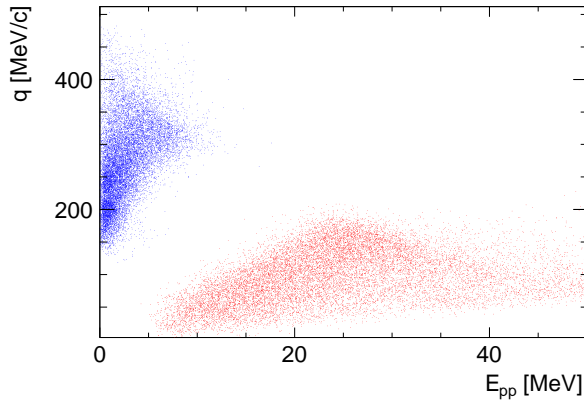
Figure 4.34: The three-momentum transfer q versus the pp excitation energy E_{pp} for the $pd \rightarrow n\{pp\}$ events at $T_p = 600$ MeV that fall within $\pm 3\sigma$ of the neutron peak. The data are shown separately for cases where the two protons enter the same (blue) or different (red) STT. The current construction of the STT means that there can be no events where q and E_{pp} are simultaneously small.

investigation at ANKE, can not be covered by the STT detection system. The dueteron charge-exchange reaction is selected by requiring the excitation $E_{pp} < 3$ MeV, which insures that the final proton pair mainly be in $^1S_0$ state.

For the charge-exchange process $p\vec{d} \rightarrow n\{pp\}_s$ where the internal freedom of the diproton is not considered, the polarized differential cross section is the same as that of a two-body reaction induced by a polarized spin-1 particle, i.e its cross section is identical to Eq. 4.3, which is repeated here

$$\frac{d\sigma}{d\Omega}^P (\theta, \phi) = \frac{d\sigma}{d\Omega}^0 (\theta)\{1 + \frac{3}{2}Q_y A_y(\theta) \cos \phi$$
$$+ \frac{1}{4}Q_{yy}[A_{yy}(\theta)(1 + \cos 2\phi) + A_{xx}(\theta)(1 - \cos 2\phi)]\} \quad (4.32)$$

Therefore other formulae used for the proton-deuteron elastic reaction in section 4.2.1 , such as Eq. 4.13, are valid in this section.

Theoretical calculation predicted that the deuteron vector analyzing power A_y^d of $p\vec{d} \rightarrow n\{pp\}_s$ should be zero if the final diproton is at $^1S_0$ state [52]. This was confirmed experimentally in the small three-momentum-transfer region in the previous investigations[56, 58]. In present work the measurement in the region where 140 MeV$/c < q < 400$ MeV$/c$ also support this prediction. The polarization pair $(1, 2)$ was used to measure to the deuteron vector polarization A_y^d since for this pair the ideal values of the averaged vector polarization $\langle Q_y \rangle$ and the tensor polarization difference ΔQ_{yy} both vanish. In this case the formula for the ratio between the difference and sum of modes 1 and 2 ($R = \frac{N_1 - N_2}{N_1 + N_2}$) , i.e. Eq. 4.13, reduces to

$$r(\theta, \phi) = \frac{\frac{3}{2}A_y(\theta) \cos \phi \Delta Q_y}{2 + \frac{1}{2}[A_{xx}(\theta)(1 - \cos 2\phi) + A_{yy}(\theta)(1 + \cos 2\phi)] \langle Q_{yy} \rangle}, \quad (4.33)$$

However, the measured values of $\langle Q_y \rangle$ and ΔQ_{yy} actually differ from zero (see
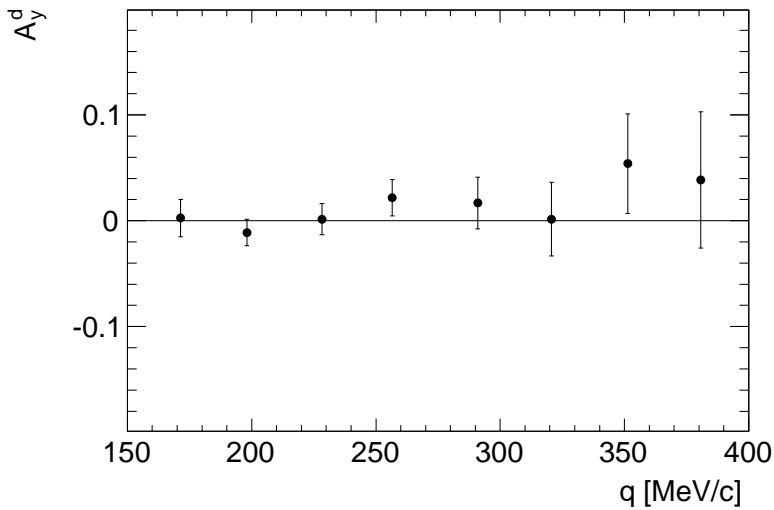
Figure 4.35: Deuteron vector analyzing power A_y^d of the $p\vec{d} \rightarrow n\{pp\}_s$ reaction with an $E_{pp} < 3$ MeV cut. Impulse approximation predictions based upon the SP07 solution for the neutron-proton elastic scattering amplitudes were used to correct for tensor analyzing power effects.

Table 4.4). In order to eliminate the contribution form $\langle Q_y \rangle$ and ΔQ_{yy} to the largest extent, the ratio difference $D = R_L - R_R$ between the data close to $\phi = 0$ and $\phi = \pi$, corresponding to the centers of left and right STTs respectively, is evaluated to measure A_y^d. By fitting the measured quantity $R_L - R_R$ with

$$d = \frac{3 A_y(\theta) \Delta Q_y}{2 + A_{yy}(\theta) \langle Q_{yy} \rangle} \tag{4.34}$$

the vector analyzing power A_y^d can be obtained. Moreover the Impulse approximation predictions based upon the SP07 solution for the neutron-proton elastic scattering amplitudes were used to correct the tensor analyzing power effects. The average of the vector polarization over all momentum transfers were found to be $A_y^d = 0.005 \pm 0.008$, agree with the theoretical prediction $A_y^d = 0$.

For the data in the centers of the STTs ($\cos 2\phi = 1$), taking into account that $A_y^d = 0$, the formula Eq. 4.13 is simplified as

$$r(\theta) = \frac{\frac{1}{2} A_{yy}(\theta) \Delta Q_{yy}}{2 + A_{yy}(\theta) \langle Q_{yy} \rangle} \tag{4.35}$$

Via fitting the ratio $R = \frac{N_a - N_b}{N_a + N_b}$ with above function, the dueteron tensor polarization A_{yy}^d can be measured. Due to the large values of $\langle Q_{yy} \rangle$ and ΔQ_{yy}, the polarization modes 3 and 4 are more suitable for determining A_{yy}^d. As in the case of A_y^d measurement, the impulse approximation was used to correct the small residual effects from the analyzing power A_{yy}^d. As shown in Fig. **??**, A_{yy}^d were measured using both the left and right STT data, results obtained from the two data sets agree with each other within the error. Fig. **??** shows the result using
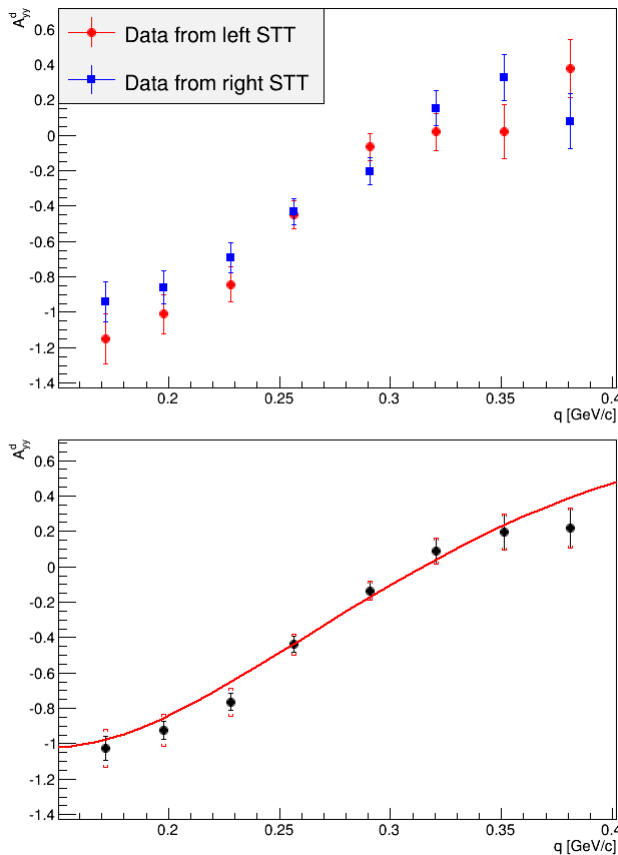
Figure 4.36: The dueteron tensor analyzing power A_{yy}^d of deuteron charge-exchange reaction $p\vec{d} \rightarrow n\{pp\}_s$ at $T_p = 600$ MeV. In the left panel values measured with left and right STTs are indicated by red dot and blue square respectively. The averaged results using the combined data are plotted in the right panel. The curve represents the calculation using the impulse approximation based on the SP07 solution for the neutron-proton elastic scattering amplitudes from the SAID database [44].

the combined data, together with the impulse approximation.

4.3.1 Discussion on the Results

The calculation based on impulse approximation [53] shows that the deuteron vector analyzing power $A_y^d = 0$ if the final proton pair is in the state $^1S_0$. The measured deuteron vector polarization presented in Fig. 4.35 agrees well with the calculation, thus confirms the reliability of the impulse approximation. In Fig. 4.37 the data below 160 MeV/c are from the measurement of the reaction $\vec{d}p \rightarrow \{pp\}_s n$ with a polarized deuteron beam of $T_d = 1200$ MeV in the first phase of the n-p scattering investigation at ANKE. The data above 160 MeV/c are measured with the inverse kinematics method in this experiment. The red curves represent the impulse approximation calculations using the SP07 solution from the SAID database as the np scattering amplitudes. The deuteron tensor analyzing power A_{yy}^d measured in this experiment connect smoothly to the previously measured data, and agree with the impulse approximation. The silicon tracking telescopes (STTs) placed on the left and right sides of the target are not able to cover the regions close to the azimuthal angles $\pm \frac{\pi}{2}$, therefore the experimental signals are
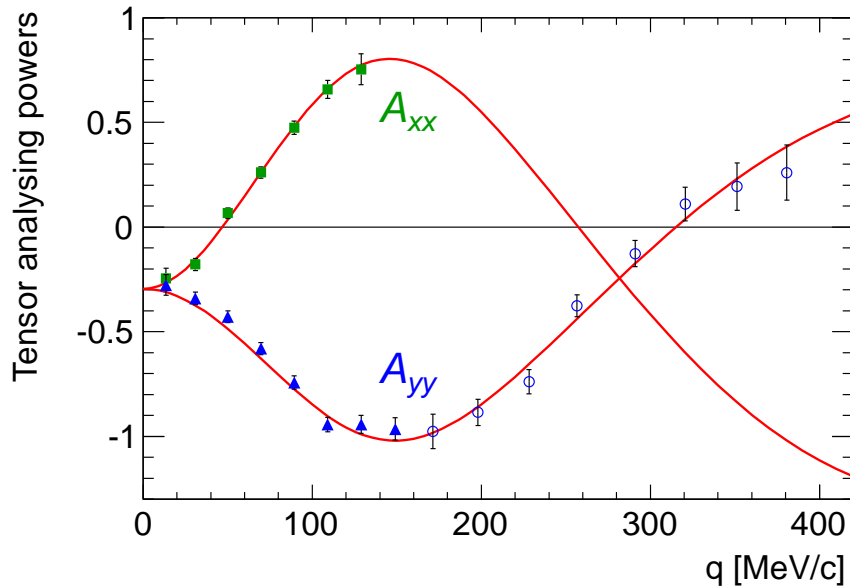
Figure 4.37: The deuteron tensor analyzing powers A_{xx} and A_{yy} of the s-ingle–polarized deuteron charge-exchange reaction $p\vec{d} \to \{pp\}_s n$. Only events with the excitation energy of the proton pair $E_{pp} < 3$ MeV were chosen in the data analyses, therefore the final proton pair are mainly at $^1S_0$ state. The impulse approximation [52] based on the np amplitudes provided by the SP07 solution of the SAID database [44] are plotted as well. Due to the one-pion exchange, the np spin–spin amplitude δ gets its minimum at the momentum transfer $q \approx 140$ MeV$/c$ (see Fig. 2.3), accordingly the tensor analyzing powers A_{xx} (A_{yy}) also reach their maximum (minimum) value (see Eq. 2.5).

not sensitive to the analyzing power A_{xx}^d, thus A_{xx}^d was not measured in this experiment. As mentioned in the second chapter, the multiple scattering and relativity effects need to be taken into account when the three-momentum transfer is high. At present only the effects of double scattering for the $^1S_0$ final state have been incorporated into the theoretical calculations[52]. Such effects are not important in the kinematic region where the three-momentum transfer $q <$140 MeV$/c$ where the A_{yy}^d is minimum. However the double scattering effects push the momentum transfer where $A_{yy}^d = 0$ down by about 20 MeV$/c$. On the other hand the double scattering is far less important in the P and higher waves of pp system, and what's more, the cut $E_{pp} < 3$ MeV ensures that final pp pairs are mainly in $^1S_0$ state, therefore the calculation is consistent with the experiment data. Nevertheless more detailed theoretical work which includes multiple scattering in higher waves and relativity effects is in progress.

Chapter 5

Conclusion and Outlook

5.1 Summary

The work presented in this thesis is the commissioning experiment for the second phase of the neutron-proton scattering programme at ANKE[23]. The charge-exchange reaction $p\vec{d} \to n\{pp\}_s$ was studied using an unpolarized proton beam of 600 MeV provided by COSY [59], impinging on the polarized deuterium atoms which are generated by the polarized atomic beam source (ABS) [85] at the ANKE spectrometer [72]. The polarized deuterium atoms were injected into a storage cell (SC) [100, 101] to enhance the effective target thickness. In order to detect the low-momentum particles around the target and to reconstruct the event vertices, two silicon tracking telescope (STT) [73] were placed on the left and right sides of the storage cell. Particles ejected in the forward direction with high momenta were detected by the forward (Fd) and positive (Pd) detection systems of the ANKE spectrometer. During the experiment two pairs of polarization modes (refer Table. 4.1) were utilized, with an alternation between the modes in each pair every 10 seconds, such a scheme allowed to minimize the systematic error which may be caused by various instabilities. Besides the polarized deuterium atoms, data were also taken with unpolarized and nitrogen gas filled in the storage cell. Unpolarized deuterium data were used to compare with the polarized data, and the nitrogen data allowed to simulate the background from the interaction between the wall of the storage cell and the beam halo. The target polarimetry were established mainly using the proton-deuteron elastic scattering $p\vec{d} \to pd$, which was validated by the quasi-free reaction $p\vec{p} \to d\pi^+$. The criteria $E_{pp} <3$ MeV serves as a filter to exclude the P and higher waves. Both vector(A_y) and tensor (A_{yy}) analyzing

powers of the charge-exchange reaction $p\vec{d} \to n\{pp\}_s$ were measured at the high-momentum transfers (160 MeV/$c \lesssim q \lesssim$ 380 MeV/c). The following conclusion can be made base on this commissioning experiment.

- This experiment is the first time that the polarized internal target installation (PIT) ever provided a polarized deuterium target at ANKE. The results manifest that the PIT is able to provide a high-quality deuterium target in the future production experiment.

- The silicon tracking telescopes (STTs) can detect both the proton–deuteron charge-exchange reaction $p\vec{d} \to n\{pp\}_s$ and the polarization reference reaction $p\vec{d} \to pd$. This investigation shows that the STT system can meets the requirements in the aspects of both hardware [73] and software [121].

- The forward (Fd) and positive side (Pd) subdetection system of ANKE can register the quasi-free reaction $p\vec{p} \to d\pi^+$, and measure the momenta with sufficient precision through the event vertex reconstruction. The polarization measured $p\vec{p} \to d\pi^+$ confirmed the results obtained from the STT data.

- The preparatory investigation found that the polarizations of the deuterium target as well as the analyzing powers of the proton–deuteron charge–exchange reaction can be measured only with the polarized data, therefore it is possible to carry out the production experiments without take the unpolarized data thus more beam time can be used to collect the polarized data, in this way results with smaller statistic errors can be expected.

- The analyzing powers A_y and A_{yy} of the proton–deuteron charge–exchange reaction were measured at the high-momentum transfer region, the results are consistent with the impulse approximation based on the np amplitudes provided by the SAID database. This proved that the np study can be performed at high energies with the inverse-kinematics method.

5.2 Outlook: Production Experiment at High Energies

Through the commissioning experiment it is demonstrated that the polarized internal target (PIT) [83, 84] is able to produce polarized deuterium target of high quality, whose polarizations can be reliably calibrated using the reference

reaction $p\vec{d} \to pd$. The background due to the wall of the storage cell can be efficiently subtracted using the nitrogen target. Both the charge-exchange reaction $p\vec{d} \to n\{pp\}_s$ and the major polarimetry reaction $p\vec{d} \to pd$ are detected by the silicon tracking telescope (STT) [73], which is proved to be satisfactory in both hardware and software aspects. The commissioning study shows that using the deuteron-proton charge-exchange reaction the neutron-proton scattering investigation at ANKE can be extended to 2.83 GeV, the highest energy available at COSY. In the future production experiments [117] the ANKE-collaboration is going to use proton beams and polarized deuterium target to measure the deuteron tensor analyzing power A_{yy}^d, the proton vector analyzing power A_y^p and the transverse spin-correlation coefficients $C_{x,x}$ and $C_{y,y}$. The target polarization will be measured at 600 MeV. In order to do so, the COSY beam will be prepared in the super cycle mode, where beams of different energy will be provided successively. To measure the proton analyzing power and the spin-correlation coefficients polarized proton beams have to be employed. The beam polarization will be measured by the EDDA detector [124, 125], which is located at another target internal station of COSY. In the production experiment measurements will be performed at
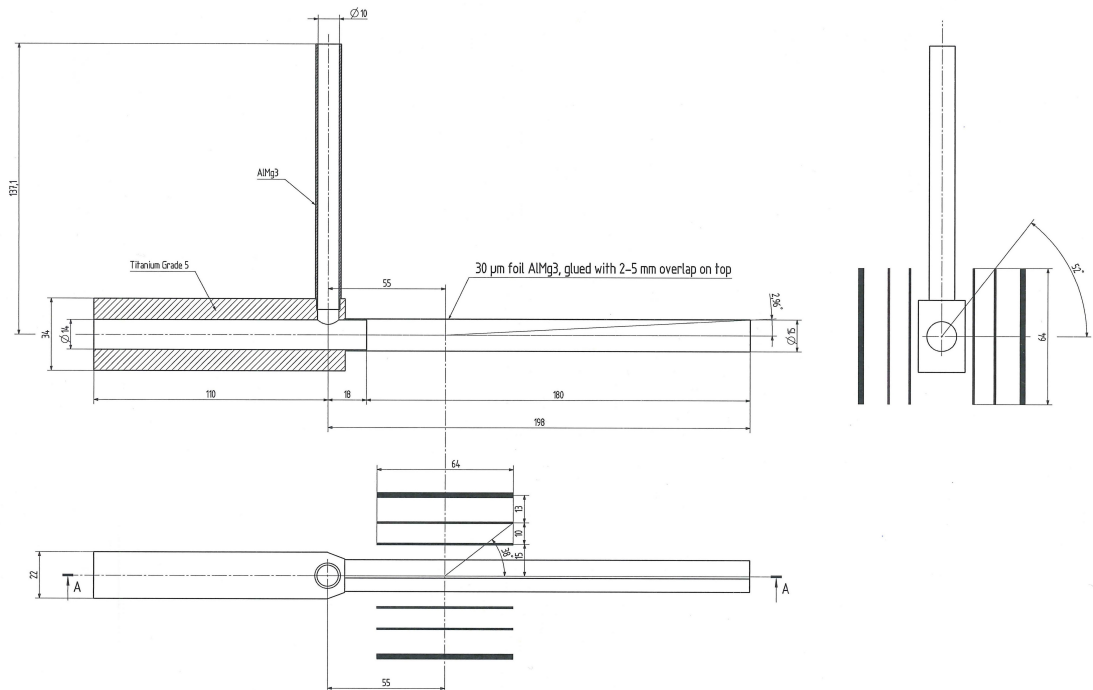
Figure 5.1: CAD drawing of the new storage cell. The thick block on the left side will exhaust the beam halo, thus in the region where the STT is placed there will be little beam-cell interaction, which was the main background source in the previous and present experiments. The STT is also drawn at its installation position.

energies from $T_p = 1.135$ GeV up to 2.83 GeV, the results are expected to provide valuable data of np scattering, which will improve human's knowledge about the nuclear force.

A new target storage cell (see Fig. 3.23), which will be open during cooling-stacking process and be closed when the beam phase space gets small, will be employed. The titanium, which cause less depolarization, will be coated on the inner wall or the storage cell. In addition, the short part of the beam tube will be very thick (10 mm), this thick block will eliminate the beam halo (see Fig. 5.1). As a result there will be little background caused by the cell wall.

List of Figures

List of Tables

Bibliography

[1] A.A. Michelson, E.W. Morley, *Amer. J. Sci.* **34** 333 (1887).

[2] J.J. Thomson et al., *Philosophical Magazine Series 5* **44** 293 (1897).

[3] E. Rutherford, F.R.S., *Philosophical Magazine Series 6* **21** 669 (1911).

[4] N. Bohr, *Philosophical Magazine Series 6* **26** 1 (1911).

[5] J. Chadwick, *Nature* **129** 312 (1932).

[6] J. Chadwick, *Proc. R. Soc. Lond. A* **136** 692 (1932).

[7] H. Yukawa, *Proc. Phys. Math. Soc. Japan* **17** 48 (1935).

[8] W. Haeberli, *Annu. Rev. Nucl. Sci.* **17** 373 (1967).

[9] S. R. Mane, et al., *Rep. Prog. Phys.* **68** 1997 (2005).

[10] G.A. Korolev, et al., *Nucl. Phys. A* **165** 262 (1985).

[11] B.H. Silverman, et al., *Nucl. Phys. A* **499** 763 (1989).

[12] J. Ball, et al., *Z. Phys. C* **40** 193 (1988).

[13] A.S. Clough , et al., *Phys. Rev. C* **21** 988 (1980).

[14] A.S. Clough , et al., *AIP Conf. Proc.* **69** 871 (1981).

[15] P.J. Riley, et al., *Phys. Lett. B* **103** 313 (1981).

[16] P.J. Riley, et al., *Phys. Lett. B* **243** 137 (1986).

[17] R. Binz, et al., *Phys. Lett. B* **231** 323 (1989).

[18] D.G. Crabb and W. Meyer, *Annu. Rev. Nucl. Part. Sci.* **47** 67 (1997).

[19] E. Steffens, W. Haeberli, *Rep. Prog. Phys.* **66** 1887 (2003).

[20] A. Abragam and M. Goldman, *Rep. Prog. Phys.* **41** 396 (1978).

[21] J. Bystricky, et al., *Phys. Lett. B* **142** 130 (1984).

[22] H. Rohdjess, *AIP Conf. Proc.* **421** 99 (1998).

[23] A. Kacharava et al., *Spin Physics from COSY to FAIR*, COSY proposal **152** (2005) arXiv:nuclex/0511028.

[24] J. Bystricky, et al., *Nucl. Phys. B* **262** 715 (1985).

[25] V.G. Vovchenko, et al., *JETP Lett.* **44** 151 (1986).

[26] N.S. Borisov, et al., *JETP Lett.* **43** 723 (1986).

[27] N.A. Bazhanov, et al., *JETP Lett.* **47** 516 (1988).

[28] J. Bystricky, et al., *Nucl. Phys. B* **321** 284 (1989).
C.D. Lac, et al., *Phys. Lett. B* **297** 653 (1988).
C.D. Lac, et al., *Phys. Lett. B* **315** 284 (1989).
C.D. Lac, et al., *Phys. Lett. B* **321** 269 (1989).
C.D. Lac, et al., *Phys. Lett. B* **321** 284 (1989).

[29] H. Shimizu, et al., *Phys. Rev. C* **42** 483 (1990).

[30] M. Garçon, et al., *Phys. Lett. B* **183** 273 (1987).

[31] D. Albers，et al., *Phys. Rev. Lett.* **78** 1652 (1997).

[32] M. Altmeier，et al., *Phys. Rev. Lett.* **85** 1819 (2000).

[33] F. Bauer，et al., *Phys. Rev. Lett.* **90** 142301 (2003).

[34] F. Bauer，et al., *Eur. Phys. J. A* **18** 555 (2003).

[35] F. Bauer, et al., *Phys. Rev. C* **71** 054002 (2005).

[36] J. Antille, et al., *Phys. Lett. B* **185** 1 (1981).

[37] G.R. Court, et al., *Phys. Rev. Lett.* **57** 507 (1986).
D.G. Crabb, et al., *Phys. Rev. Lett.* **60** 2351 (1988).
D.G. Crabb, et al., *Phys. Rev. Lett.* **65** 3241 (1990).
P.R. Cameron, et al., *Phys. Rev. C* **32** 3270 (1985).

[38] J. Ball, et al., *Nucl. Phys. A* **574** 697 (1994).

[39] J. Ball, et al., *Il Nuovo Cimento* **11** 13 (1998).

[40] J. Sowinski, et al., *Phys. Lett. B* **199** 341 (1987).

[41] R. Abegg, et al., *Phys. Rev. Lett.* **56** 2571 (1986).

[42] R. Binz et al., *Phys. Lett. B* **231** 323 (1989).
R. Binz et al., *PSI Nucl. Part. Phys. Newsletter 1990* **231** 37 (1990).
R. Binz et al., *Nucl. Phys. A* **533** 601 (1991).

[43] M.W. Rawool, *Los Alamos Report* **LA-11387-T** (1988)
R. Garnett, et al., *Phys. Rev. D* **40** 1708 (1989).
C.R. Newsom, et al., *Phys. Rev. C* **40** 2684 (1989).
C.R. Newsom, et al., *Phys. Rev. C* **41** 2732 (1990).
W.R. Ditzler, et al., *Phys. Rev. C* **44** 2267 (1991).
W.R. Ditzler, et al., *Phys. Rev. D* **46** 2792 (1992).

[44] R.A. Arndt, I.I. Strakovsky, *R.L. Workman, Phys. Rev. C* **62** 034005 (2000)
http://gwdac.phys.gwu.edu.

[45] http://nn-online.org/

[46] J. Bystricky, et al., *J. Phys. France* **51** 2747 (1990).

[47] http://pwa.hiskp.uni-bonn.de/

[48] M. H. MacGregor, M. J. Moravcsik, H. P. Stapp, *Annu. Rev. Nucl. Sci.* **10** 291 (1960).

[49] G. G. Ohlsen, *Rep. Prog. Phys.* **35** 717 (1972).

[50] J. E. Bowcock, H. Burkhardt, *Rep. Prog. Phys.* **38** 1099 (1975).

[51] G. Barton, *Introduction to dispersion techniques in field theory* W.A. Benjamin,(1965).

[52] D.V. Bugg, C. Wilkin, *Nucl. Phys. A* **467** 575 (1987).

[53] J. Carbonell, M.B. Barbaro, C. Wilkin, *Nucl. Phys. A* **529** 653 (1991).

[54] D. Chiladze et al., *Eur. Phys. J. A* **40** 23 (2009).

[55] A. Khoukaz et al., *Eur. Phys. J. D* **5**, 275 (1999).

[56] D. Chiladze et al., *Phys. Lett. B* **637** 170 (2006).

[57] D. Chiladze, et al., *Phys. Rev. Spec. Top., Accel. Beams* **9** 050101 (2006).

[58] D. Mchedlishvili et al., *Eur. Phys. J. A* **49** 49 (2013).

[59] R. Maier, *Nucl. Instr. Methods A* **390** 1 (1997).

[60] R. Weidmann, et al., *Rev. Sc. Instr.* **67** 1357 (1996).

[61] M. Eggert，et al.，*Nucl. Instr. Methods A* **453** 514 (2000).

[62] C. Weidemann, et al., *Phys. Rev. Spec. Top., Accel. Beams* **18** 020101 (2015).

[63] D. Eversmann，et al., *Phys. Rev. Lett.* **115** 094801 (2015).

[64] H.J. Stein, et al., *Atomic Energy* **94** 24 (2003).

[65] H.J. Stein, et al., *Proceedings of RuPAC 2002*, arxiv.org/abs/1101.5963/.

[66] V. Kamerdzhiev，et al.，*Nucl. Instr. Methods A* **532** 285 (2004).

[67] D. Prasuhn，et al.，*Nucl. Instr. Methods A* **441** 167 (2000).

[68] B. Höistad, J. Ritman et al., *Wide Angle Shower Apparatus (WASA) at COSY-Jülich*, COSY proposal (2004) arXiv:nucl-ex/0411038.

[69] N. Alinovskiy，et al.，*Proceedings of IPAC 2014, Dresden, Germany* **MO-PRI070** 2014), avilavle at http://jacow.org/.

[70] S. Chattopadhyay, *Nucl. Phys. A* **931** 267 (2014).

[71] R. Maier，*Proceedings of IPAC 2011, New York, USA* **THOCN2** 2014), published by the PAC'11 OC/IEEE.

[72] S. Barsov，et al.，*Nucl. Instr. Methods A* **462** 364 (2001).

[73] R. Schleichert，et al.，*IEEE Trans. Nucl. Sci.* **50** 301 (2003).

[74] H. Dombrowski，et al.，*Nucl. Instr. Methods A* **386** 228 (1997).

[75] A. Khoukaz，et al.，*Eur. Phys. J. D* **5** 275 (1999).

[76] A. Täschner，et al.，*Nucl. Instr. Methods A* **660** 22 (1997).

[77] R. Brüggemann，et al.，*AIP Conf. Proc.* **570** 830 (2000).

[78] F. Rathmann，et al.，*AIP Conf. Proc.* **675** 924 (2002).

[79] S. Dymov, et al., *Particles and Nuclei, Letters* **2**, 40 (2004).

[80] B. Chiladze, et al., *Particles and Nuclei, Letters* **4**, 113 (2002).

[81] P. A. Čerenkov, *Phys. Rev.* **52** 378 (1937).

[82] M. Büscher，et al., *Nucl. Instrum. Methods A* **481** 378 (2002).

[83] F. Rathmann，et al., *Czechoslovak Journal of Physics* **82** 681 (2002).

[84] K. Grigoryev，et al., *Int. J. Mod. Phys. E* **18** 511 (2009).

[85] M. Mikirtychyants，et al., *Nucl. Instrum. Methods A* **721** 83 (2013).

[86] K. Grigoryev，et al., *Nucl. Instr. Methods A* **599** 130 (2009).

[87] R. Engels, et al., *Rev. Sc. Instr.* **74** 4607 (2003).

[88] R. Engels, et al., *Rev. Sc. Instr.* **76** 053305 (2005).

[89] W. Gerlach, O. Stern, *Zeitschrift für Physik* **9** 353 (1922).

[90] A. Abragam, J. M. Winter, *Phys. Rev. Lett.* **1** 374 (1958).

[91] P. Zeeman, *Versl. Kon. Ak. Wet.* **5** 181 (1896),
    P. Zeeman, *Phil. Mag.* **43** 226 (1897).

[92] G. Breit, I. I. Rabi, *Phys. Rev.* **38**, 2082 (1931).

[93] S. Oh, *Nucl. Instrum. Methods* **82**, 189 (1970).

[94] J.P.M. Beijers, *Nucl. Instrum. Methods A* **536**, 282 (2005).

[95] H. Paetz gen. Schieck, *Nucl. Instrum. Methods A* **587**, 213 (2008).

[96] A. Nass, et al., *Nucl. Instrum. Methods A* **505**, 633 (2003).

[97] H. Kleines, et al., *Nucl. Instrum. Methods A* **560**, 503 (2006).

[98] A.D. Roberts, et al., *Nucl. Instrum. Methods A* **322**, 6 (1992).

[99] T. Wise, et al., *Nucl. Instrum. Methods A* **336**, 410 (1993).

[100] K. Grigoryev, et al., *AIP Conf. Proc.* **915**, 979 (2007).

[101] K. Grigoryev, et al., *Nucl. Instrum. Methods A* **599**, 130 (2009).

[102] A. Roth, *Vacuum Technology, third ed.* ElsevierScience B.V., Amsterdam (1990).

[103] R. Weidmann, et al., *Rev. Sci. Instr.* **67**, 1357 (1996).

[104] D. Prasuhn, et al., *Nucl. Instrum. Methods A* **441**, 167 (2000).

[105] H.-G. Gaul, E. Steffens, *Nucl. Instrum. Methods A* **316**, 297 (1992).

[106] W. W. Lamb, Jr., and R. C. Retherford, *Phys. Rev.* **79** 549 (1950).

[107] W. W. Lamb, Jr., and R. C. Retherford, *Phys. Rev.* **81** 222 (1951).

[108] W. W. Lamb, Jr., and R. C. Retherford, *Phys. Rev.* **85** 259 (1952).

[109] G. G. Ohlsen, J. L. McKibben, *Los Alamos Scientific Lab. Report* **LA-3725** (1967).

[110] J. L. McKibben, G. P. Lawrence, and G. G. Ohlsen, *Phys. Rev. Lett.* **20** 1180 (1968).

[111] H. Hanken, et al., **The Physics of Atoms and Quanta** *Introduction to Experiments and Theory*, Springer, (2005).

[112] http://www-hades.gsi.de/?q=pluto

[113] http://geant4.cern.ch/

[114] A. Garishvili, et al., *Measurement of the $\vec{d}\vec{p} \to \{pp\}n$, Charge-Exchange Reaction with Polarised Beam and Target*, COSY proposal **172.1** (2007).

[115] S. Barsov, et al., *Commissioning and Initial Research with the Polarised Internal Deuterium Gas Target at ANKE*, COSY proposal **201.1** (2011).

[116] V.S. Morozov, et al., *Phys. Rev. Spec. Top., Accel. Beams* **7** 024002 (2004).

[117] Z. Bagdasarian, et al., *Measurement of spin observables in $\vec{p}\vec{d}$ elastic and inelastic scattering with polarised beam and target at ANKE–COSY*, COSY proposal **218** (2013).

[118] M. Haji-Said, et al., *Phys. Rev. C* **36**, 2010 (1987).

[119] J. Arvieux, et al., *Nucl. Phys. A* **431**, 613 (1984).

[120] J. Arvieux, et al., *Nucl. Instrum. Methods A* **273**, 48 (1988).

[121] G. Macharashvili, *The Software Development For The Silicon Detector Data Analysis at ANKE-COSY*, available at http://apps.fz-juelich.de/pax/paxwiki/index.php/Main_Page.

[122] S. Dymov, D. Gusev, *IKP Annual Report* (2005), available at http://http://collaborations.fz-juelich.de/ikp/anke/annual.shtml

[123] E. Byckling, K. Kajantie, **Particle Kinematics**, John Wiley & Sons Ltd (1973).

[124] J. Bisplinghoff, et al., *Nucl. Instrum. Methods A* **329**, 151 (1993).

[125] K. Ackerstaff, et al., *Nucl. Instrum. Methods A* **335**, 113 (1993).